

Cement paste degradation under external sulfate attack
An experimental and numerical research

Ma, Xu

DOI

[10.4233/uuid:8da7150b-eec8-4148-b277-538b6bfc1384](https://doi.org/10.4233/uuid:8da7150b-eec8-4148-b277-538b6bfc1384)

Publication date

2018

Document Version

Final published version

Citation (APA)

Ma, X. (2018). *Cement paste degradation under external sulfate attack: An experimental and numerical research*. [Dissertation (TU Delft), Delft University of Technology]. <https://doi.org/10.4233/uuid:8da7150b-eec8-4148-b277-538b6bfc1384>

Important note

To cite this publication, please use the final published version (if applicable).
Please check the document version above.

Copyright

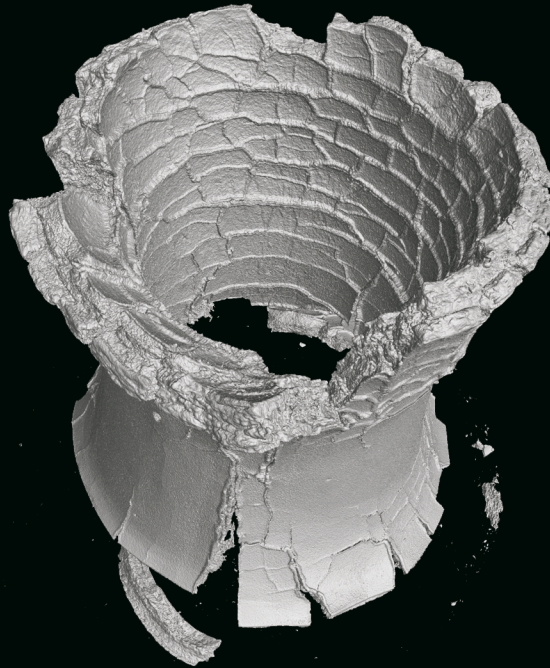
Other than for strictly personal use, it is not permitted to download, forward or distribute the text or part of it, without the consent of the author(s) and/or copyright holder(s), unless the work is under an open content license such as Creative Commons.

Takedown policy

Please contact us and provide details if you believe this document breaches copyrights.
We will remove access to the work immediately and investigate your claim.

CEMENT PASTE DEGRADATION UNDER EXTERNAL SULFATE ATTACK

AN EXPERIMENTAL AND NUMERICAL RESEARCH



Xu MA

CEMENT PASTE DEGRADATION UNDER EXTERNAL SULFATE ATTACK

AN EXPERIMENTAL AND NUMERICAL RESEARCH

CEMENT PASTE DEGRADATION UNDER EXTERNAL SULFATE ATTACK

AN EXPERIMENTAL AND NUMERICAL RESEARCH

Dissertation

for the purpose of obtaining the degree of doctor
at Delft University of Technology
by the authority of the Rector Magnificus prof. dr. ir. T.H.J.J van der Hagen
chair of the Board for Doctorates
to be defended publicly on
Monday 12 November 2018 at 10:00 o'clock

by

Xu MA

Master of Science in Geotechnical Engineering, Guangzhou University, China
born in Shaanxi, China.

This dissertation has been approved by the promotor:

promotor: Prof. dr. ir. E. Schlangen

copromotor: Dr. O. Çopuroğlu

Composition of the doctoral committee:

Rector Magnificus,	chairperson
Prof. dr. ir. E. Schlangen,	Delft University of Technology, promotor
Dr. O. Çopuroğlu,	Delft University of Technology, copromotor

Independent members:

Prof. dr. I. Carol,	Universitat Politècnica de Catalunya, Spain
Prof. dr. ir. K. van Breugel,	Delft University of Technology
Prof. dr. ir. D.A. Hordijk,	Delft University of Technology
Dr. G. Ye,	Delft University of Technology

Other member:

Prof. dr. N. Han,	Shenzhen University, China
-------------------	----------------------------

Keywords: External sulfate attack, Cement paste, Thin-wall pipe, Longitudinal restraint, Expansion, Stress, Pore size distribution, Sulfur distribution, Phase analysis, Crack initiation and propagation, Image analysis, Lattice fracture model

Printed by: Ipskamp Printing, The Netherlands.

Cover design: Xu MA and Yu CHEN

Copyright © 2018 by X. Ma

All rights reserved. This copy of the thesis has been supplied on condition that anyone who consults it is understood to recognize that its copyright rests with its author and that no quotation from the thesis and no information derived from it may be published without the author's prior consent.

ISBN 978-94-6186-982-1

An electronic version of this dissertation is available at

<http://repository.tudelft.nl/>.

To my parents

CONTENTS

List of Figures	xi
List of Tables	xvii
Part 1: Introduction and literature review	1
1 Introduction and literature review	3
1.1 Introduction	4
1.1.1 Degradation process	4
1.1.2 Exposure conditions	6
1.1.3 Sources of external sulfate	7
1.2 Review of literature on external sulfate induced expansion and degradation	8
1.2.1 Mechanism	8
1.2.2 Influencing factors	13
1.2.3 Geometry of specimens	18
1.3 Objectives of this research	21
1.4 Outline of the thesis	21
Part 2: Experimental investigations	25
2 Experimental study on cement paste pipe expansion due to external sulfate attack	27
2.1 Introduction	28
2.2 Materials and methods	28
2.2.1 Specimen preparation and test setup	28
2.2.2 Calibrations of experimental setup	31
2.2.3 Calculations of expansion and generated stress	33
2.2.4 Mercury intrusion porosimetry	34
2.3 Results and discussion	34
2.3.1 Free expansion	34
2.3.2 Restrained expansion and generated stress	36
2.3.3 Pore size distribution	37
2.4 Summary and conclusions	40
3 Microanalysis of cement paste degradation caused by external sulfate attack	43
3.1 Introduction	44
3.2 SEM-EDS microanalysis	44
3.2.1 Materials and methods	44
3.2.2 Image analysis	46

3.3	Micro-computed tomography technique	47
3.3.1	Materials and methods.	47
3.3.2	Image analysis	48
3.4	Results and discussion	51
3.4.1	Sulfur distribution	51
3.4.2	Crack pattern	59
3.5	Summary and conclusions	70
4	Microstructural evolution of cement paste exposed to strong sodium sulfate solution	73
4.1	Introduction	74
4.2	Image analysis	74
4.2.1	BSE micrograph	74
4.2.2	EDS elemental distribution map	77
4.2.3	Combined analysis.	78
4.3	Results and discussion	78
4.3.1	Precipitation of gypsum	78
4.3.2	Crack initiation and propagation.	80
4.3.3	Development of internal expansive pressure.	83
4.4	Summary and conclusions	85
4.5	Discussion of results from part 2 and conclusions	86
	Part 3: Numerical investigations compared with experimental analyses	89
5	Experimental and numerical study on mechanical properties of cement paste pipe without sulfate exposure	91
5.1	Introduction	92
5.2	Materials and methods	92
5.2.1	Materials and specimens.	92
5.2.2	Uniaxial tensile test	94
5.2.3	Lattice Fracture Model	94
5.3	Experimental results and discussion	96
5.3.1	Unnotched cement paste pipes	96
5.3.2	Single notched cement paste pipes	96
5.3.3	Discussion	98
5.4	Numerical simulation results and discussion	98
5.4.1	Unnotched cement paste pipe	98
5.4.2	Single notched cement paste pipe	99
5.4.3	Discussion	105
5.5	Summary and conclusions	106
6	Mesoscale modeling of expansion and damage of cement paste pipe in strong sodium sulfate solution	109
6.1	Introduction	110
6.2	Numerical details and methods.	110
6.2.1	Lattice Fracture Model	110
6.2.2	Modeling basics of ESA mechanism	112

6.3	Numerical simulation results and discussion	116
6.3.1	Restrained expansion and generated stress	116
6.3.2	Suggested equation to estimate expansive pressure	117
6.3.3	Largest generated stress and crack pattern.	118
6.4	Summary and conclusions	121
Part 4: Conclusions and discussion of results		123
7	Conclusions and discussion of results	125
7.1	Retrospection	126
7.2	General conclusions and discussion	127
7.3	Recommendations for future work	130
References		133
References		133
Summary		143
Samenvatting		147
Curriculum Vitae		151
List of Publications		153
Acknowledgements		155

LIST OF FIGURES

1.1	Schematic view of the formation of hydrate phases and the structure development during cement hydration according to [1].	5
1.2	Simple description of degradation process caused by external sulfate attack.	6
1.3	SEM micrographs of ettringite crystals. (a) Needle-shaped ettringite crystals with a thickness between 20 nm and 200 nm lying close to large crystals and (b) needle-shaped ettringite crystals with a hexagonal cross-section and a thickness of about 2 μm according to [2].	9
1.4	SEM micrographs of ettringite crystals. (a) Large long-needle ettringite crystals inside a pore according to [3] and (b) entrained air bubble filled with ettringite crystals according to [4].	9
1.5	The relationship between crystallization pressure (P) and supersaturation (Q/K) for ettringite according to Eq. 1.4.	11
1.6	The assumed relationship between crystallization pressure (P) and spherical crystal radius (r) according to Eq. 1.6. γ_{cl} of ettringite was used.	12
1.7	Relationship between the coefficient of permeability and W/C ratio for mature cement paste according to [5] and [6].	13
1.8	Expansion of mortars with different W/C ratio under external sulfate attack according to [7].	13
1.9	Expansion of mortars with different C ₃ A content under external sulfate attack according to [7].	15
1.10	Length change over time for different sulfate solutions for mortar bars made with CEM I cement according to [8, 9].	16
1.11	Phase assemblage of the mortar specimens immersed in (a) 4 g/L Na ₂ SO ₄ and (b) 44 g/L Na ₂ SO ₄ solutions as calculated with GEMS according to [10].	18
1.12	Expansion of mortars (CEM I, W/C ratio of 0.55) with different size in 3 g/L sodium sulfate solution according to [11].	19
1.13	Expansion of mortars (CEM I, W/C ratio of 0.5) with different sand/cement ratio in 10 % sodium sulfate solution according to [12].	20
1.14	Outline of the thesis.	23
2.1	PVC moulds and specimens.	29
2.2	Three types of restraints; (A) thick steel bar (high-restraint, diameter of 7 mm), (B) thin steel bar (low-restraint, diameter of 3 mm) and (C) spring (non-restraint).	30
2.3	Specimens immersed in sodium sulfate solutions with two different SO ₄ ²⁻ ion concentrations; (a) 1.5 g/L and (b) 30 g/L.	31
2.4	Force-strain responses of steel bars subjected to uniaxial tensile load along longitudinal direction.	32

2.5	Setup of torque test calibration.	33
2.6	Free expansions of the cement paste pipes in weak and strong sulfate solutions	35
2.7	Restrained expansions of the cement paste pipes in weak and strong sulfate solutions	35
2.8	Generated stresses of the restrained cement paste pipes in weak and strong sulfate solutions	36
2.9	Pore size distribution differential curves after being exposed to (a) weak and (b) strong sulfate solutions of unrestrained specimens	38
2.10	Pore size distribution differential curves for (a) 21-day, (b) 70-day, (c) 105-day, (d) 133-day and (e) 189-day immersion of unrestrained specimens	39
3.1	Specimen used in the experiments	45
3.2	Sample for SEM-EDS microanalysis (polished section coated with carbon)	46
3.3	Setup of CT scanning (specimens were surrounded with deionized water)	48
3.4	Segmentation procedure of cracks. (a) Original microtomography slice from the CT scanning (one image from Fig. 3.20 a). (b) Image segmentation of (a). (c) Reference image based on (b). (d) Segmented cracks based on (b) and (c).	49
3.5	3D construction of images based on (a) binary slices from Fig. 3.4 b and (b) segmented cracks from Fig. 3.4 d.	50
3.6	Combined BSE and original sulfur mapping images for (a) 21-day, (b) 70-day, (c) 105-day, (d) 133-day and (e) 189-day immersion in 1.5 g/L SO_4^{2-} of unrestrained specimens. Left edge of each image was the exposed surface. The field of view of each micrograph is $1264 \times 948 \mu\text{m}^2$	52
3.7	Combined BSE and original sulfur mapping images for (a) 21-day, (b) 70-day, (c) 105-day, (d) 133-day and (e) 189-day immersion in 30 g/L SO_4^{2-} of unrestrained specimens. Left edge of each image was the exposed surface. The field of view of each micrograph is $1264 \times 948 \mu\text{m}^2$	53
3.8	Rescaled sulfur mapping images in weight percentage (wt. %) for (a) 21-day, (b) 70-day, (c) 105-day, (d) 133-day and (e) 189-day immersion in 1.5 g/L SO_4^{2-} of unrestrained specimens. Left edge of each image was the exposed surface	54
3.9	Rescaled sulfur mapping images in weight percentage (wt. %) for (a) 21-day, (b) 70-day, (c) 105-day, (d) 133-day and (e) 189-day immersion in 30 g/L SO_4^{2-} of unrestrained specimens. Left edge of each image was the exposed surface	55
3.10	Sulfur distributions along diffusion direction after being exposed to (a) weak and (b) strong sulfate solutions of unrestrained specimens	56
3.11	Sulfur distributions along diffusion direction for (a) 21-day, (b) 70-day, (c) 105-day, (d) 133-day and (e) 189-day immersion of unrestrained specimens	57
3.12	Specimens immersed in sodium sulfate solutions. (a) 807-day immersion in 1.5 g/L SO_4^{2-} , (b) 435-day immersion in 30 g/L SO_4^{2-} , (c) 581-day immersion in 30 g/L SO_4^{2-} and (d) 735-day immersion in 30 g/L SO_4^{2-}	60

3.13	3D renderings of unrestrained specimen (specimen 1) by CT scanning after 189-day immersion in 30 g/L SO_4^{2-}	61
3.14	Reconstructed microtomography slices (3 random cross section) of unrestrained specimen (specimen 1) after 189-day immersion in 30 g/L SO_4^{2-}	61
3.15	Reconstructed microtomography slices of unrestrained specimen (specimen 1) after 189-day immersion in 30 g/L SO_4^{2-} . (a) 3 random longitudinal section and (b) the corresponding distribution of gray value along thickness direction (the area covered by the yellow frame was analyzed).	62
3.16	Unrestrained specimen (specimen 2) after (a) 294-day, (b) 343-day, (c) 420-day and (d) 469-day immersion in 30 g/L SO_4^{2-}	63
3.17	3D renderings of unrestrained specimen (specimen 2) by CT scanning after (a) 294-day, (b) 343-day, (c) 420-day and (d) 469-day immersion in 30 g/L SO_4^{2-}	64
3.18	Reconstructed microtomography slices from top to bottom of unrestrained specimen (specimen 2) after (a) 294-day, (b) 343-day and (c) 420-day immersion in 30 g/L SO_4^{2-}	65
3.19	Restrained specimens immersed in 30 g/L SO_4^{2-} . (a) 581-day immersion under high-restraint condition (7 mm) (specimen 3) and (b) 765-day immersion under low-restraint condition (3 mm) (specimen 4).	66
3.20	3D renderings of restrained specimens immersed in 30 g/L SO_4^{2-} by CT scanning after (a) 581-day immersion under high-restraint condition (7 mm) (specimen 3) and (b) 765-day immersion under low-restraint condition (3 mm) (specimen 4).	67
3.21	Reconstructed microtomography slices from top to bottom of restrained specimens immersed in 30 g/L SO_4^{2-} after (a) 581-day immersion under high-restraint condition (7 mm) (specimen 3) and (b) 765-day immersion under low-restraint condition (3 mm) (specimen 4).	68
3.22	3D crack pattern of restrained specimens immersed in 30 g/L SO_4^{2-} after (a) 581-day immersion under high-restraint condition (7 mm) (specimen 3) and (b) 765-day immersion under low-restraint condition (3 mm) (specimen 4). Based on Fig. 3.20 and Fig. 3.4.	69
4.1	BSE micrographs and rescaled EDS elemental distribution maps in atomic percentage (%) for (a) 0-day, (b) 70-day, (c) 105-day and (d) 133-day immersion in 30 g/L SO_4^{2-} . Left edge of each image was the exposed surface. From top to bottom: BSE micrograph, sulfur distribution map, aluminum distribution map and calcium distribution map	75
4.1	(continue) BSE micrographs and rescaled EDS elemental distribution maps in atomic percentage (%) for (a) 0-day, (b) 70-day, (c) 105-day and (d) 133-day immersion in 30 g/L SO_4^{2-} . Left edge of each image was the exposed surface. From top to bottom: BSE micrograph, sulfur distribution map, aluminum distribution map and calcium distribution map	76
4.2	Segmented microstructure for (a) 0-day, (b) 70-day, (c) 105-day and (d) 133-day immersion in 30 g/L SO_4^{2-} (black - pore or crack, gray - cement hydration product, white - anhydrous cement particle).	77

4.3	Sulfur profiles of hydration product pixels along the diffusion direction	79
4.4	EDS plots of S/Ca versus Al/Ca atomic ratios on hydration product pixels at penetration depth between 0.25 mm and 0.5 mm (zone 2) for (a) 0-day, (b) 70-day, (c) 105-day and (d) 133-day immersion in 30 g/L SO_4^{2-}	79
4.5	Images of pixels with (a) $S/Al > 1.5$, (b) $S/Al > 2$, (c) $S/Al > 2.5$, (d) $S/Al > 4$ in atomic ratio. Display as white. Left edge of each image was the exposed surface. From top to bottom: 0-day, 70-day, 105-day and 133-day immersion in 30 g/L SO_4^{2-}	81
4.5	Images of pixels with (a) $S/Al > 1.5$, (b) $S/Al > 2$, (c) $S/Al > 2.5$, (d) $S/Al > 4$ in atomic ratio. Display as white. Left edge of each image was the exposed surface. From top to bottom: 0-day, 70-day, 105-day and 133-day immersion in 30 g/L SO_4^{2-}	82
4.6	Sulfur profiles of hydration product pixels along the diffusion direction excluding the pixels with $S/Al > 2.5$ in atomic ratio.	84
5.1	Setup of uniaxial tensile tests. (a) An unnotched cement paste pipe and (b) a single notched cement paste pipe.	93
5.2	Uniaxial tensile test of single notched cement paste pipes (Fig. 5.1b). (a) Geometric size of the notch and (b) cracked specimen.	93
5.3	Cell-based images of the structure of cement paste pipes for uniaxial tensile simulations. (a) Unnotched pipe and (b) single notched pipe (NOL represents numerical output location, considering LVDT used in Fig. 5.1b).	95
5.4	Experimental stress-strain responses of single notched cement paste pipes (Fig. 5.1b) subjected to uniaxial tensile loading along vertical direction. (a) Specimen 4, (b) specimen 5 and (c) comparison between specimen 4 and specimen 5 (strain is the average value of the four LVDTs).	97
5.5	Influence of increased height (Δh), which is corresponding to Fig. 5.3b. Simulated stress-strain responses of the single notched cement paste pipe (Fig. 5.3b) subjected to uniaxial tensile loading along vertical direction. Lattice elements behave as linear elastic (Fig. 5.6a). (a) $\Delta h = 0$, (b) $\Delta h = 2.5$, (c) $\Delta h = 7.5$ and (d) $\Delta h = 15$	100
5.6	Assumed local mechanical properties of lattice elements. (a) Simulation linear 1 (linear elastic behavior), (b) simulation multi-linear 2, 3, 4 (multi-linear behavior) and (c) simulation multi-linear 5 (multi-linear behavior).	101
5.7	Simulated stress-strain responses of the single notched cement paste pipe (Fig. 5.3b, $\Delta h = 15$ mm) subjected to uniaxial tensile loading along vertical direction. The local mechanical properties of lattice elements are referred to Fig. 5.6. (a) Simulation linear 1, (b) simulation multi-linear 2, (c) simulation multi-linear 3, (d) simulation multi-linear 4 and (e) simulation multi-linear 5.	102

5.8	Results of the single notched cement paste pipe (experiment: Fig. 5.1b, simulation: Fig. 5.3b, $\Delta h=15$ mm) subjected to uniaxial tensile loading along vertical direction. Strain is the average value of the four LVDTs or NOLs. Comparisons between experimental and simulated stress-strain responses (a) simulation linear 1, (b) simulation multi-linear 2, (c) simulation multi-linear 3, (d) simulation multi-linear 4, (e) simulation multi-linear 5 and (f) comparisons among simulated stress-strain responses.	103
5.9	Simulated crack patterns of the single notched cement paste pipe subjected to uniaxial tensile loading along vertical direction at (a) step 700, (b) step 6 000, (c) step 12 000 and (d) step 15 000 (black-damaged element), corresponding to Fig. 5.7e. Fig. 5.6c was used as the local mechanical properties of lattice elements.	104
6.1	The structure of cement paste pipes for simulations. (a) Cell-based image of 1/8 pipe and (b) lattice mesh used in the simulations.	111
6.2	Sulfur profiles along diffusion direction after being exposed to 30 g/L SO_4^{2-} (half of wall thickness).	113
6.3	Initial estimation of the expansive pressure in lattice node along diffusion direction after being exposed to 30 g/L SO_4^{2-} (half of wall thickness), based on Fig. 6.2 and Eq. 6.4 ($m=1$ in Eq. 6.6).	114
6.4	Initial estimation of the expansive pressure of lattice elements (based on Fig. 6.3), which was used as the input for the simulations at (a) 21-day, (b)70-day, (c) 105-day, (d) 133-day and (e) 189-day exposure to 30 g/L SO_4^{2-} (whole of wall thickness).	114
6.5	(a) Numerical results of generated stress of specimen immersed in 30 g/L SO_4^{2-} under high-restraint condition (7 mm) with the increase of analysis step and (b) the scaling factor (m) applied at the corresponding analysis step.	119
6.6	Numerical results of cracking process of specimen immersed in 30 g/L SO_4^{2-} under high-restraint condition (7 mm) with the increase of analysis step. (a) Crack pattern (black-damaged element) and (b) deformed lattice of undamaged elements.	120

LIST OF TABLES

1.1	Limiting values for exposure classes for chemical attack from natural soil and ground water according to EN 206 [13].	7
1.2	Requirements to protect against damage to concrete by sulfate attack from external sources of sulfate according to ACI 201 [14].	14
1.3	Mineral composition of Portland cement (CEM I 42,5N) calculated by Bogue equation according to [15].	15
2.1	The obtained values after two types of calibrations	32
3.1	The specimen information of the performed scans, all specimens were immersed in 30 g/L SO_4^{2-}	47
5.1	Experimental results of global mechanical properties of unnotched cement paste pipes (Fig. 5.1a)	96
5.2	Simulated results of global tensile strength of the unnotched cement paste pipe (Fig. 5.3a)	99
5.3	Calculations of fracture energy	105
5.4	Simulated results of mechanical properties of the unnotched cement paste pipe (Fig. 5.3a)	106
5.5	Suggested local mechanical properties of the lattice elements, corresponding to Fig. 5.6c	106
6.1	Local mechanical properties applied on lattice elements	112
6.2	The measured restrained expansion and generated stress of specimen immersed in 30 g/L SO_4^{2-} under high-restraint condition (7 mm)	116
6.3	The simulated expansion and scaling factor when the simulated generated stress reached the measured generated stress in experiments	117
6.4	The differences between simulated and experimental generated stress when the final scaling factor (f) is taken as 1.86	118

PART 1: INTRODUCTION AND LITERATURE REVIEW

1

INTRODUCTION AND LITERATURE REVIEW

In this chapter, a summary of the past research and the motivation of this research are presented. Main terms related to the degradation of cementitious materials caused by the ingress of external sulfate ions are described. Sources of external sulfate and mechanisms which lead to the degradation are reviewed. Different influence factors are discussed. Finally, the aims of this research are formulated.

1.1. INTRODUCTION

THE development of concrete as a construction material dates back several thousand years to the days of the ancient Egyptians, the Greeks and the Romans. And it is still the most widely used construction material in the world by far. Cement industry is facing challenges regarding economy, environment and technical development. One third to one half of the annual investments of construction are devoted to maintenance [16]. Over the last few decades, concrete durability has become a key aspect in the design of new structures and the repair of existing ones. A large number of studies can be found in the literature dealing with different kinds of degradation processes, such as corrosion of rebar, alkali-aggregate reaction, freezing and thawing of concrete and sulfate attack.

External sulfate attack (ESA) is a progressive degradation of cementitious materials upon being exposed to external sulfate ions. It is a complex issue in which ionic transport, expansive reactions and mechanical damage are responsible in varying degrees for gradually increasing macroscopic expansion and severe mechanical damage [17–19]. External sulfate ions can penetrate into the hardened concrete, and react with cement hydration products to form ettringite as well as gypsum crystals, if higher sulfate concentrations are available [20–23]. Such formations result in a solid volume increase and cause local expansive pressure within the pore network. Although the solid volume increase may initially reduce the porosity of cement paste, it may cause cracking at a later stage as the generated expansive pressure exceeds the tensile strength of the material. This, in turn, leads eventually to a total strength loss and an increased permeability of concrete. In addition, the ESA-induced degradation can also lead to the acceleration of other durability problems, such as reinforcement corrosion because of easier penetration of chloride.

1.1.1. DEGRADATION PROCESS

Portland cements used in the manufacture of concrete consist of clinker, a setting regulator and fillers, such as gypsum, blast-furnace slag, silica fume and fly ash. European standard EN 197-1 [24] classifies common cements into 5 types and 27 products according to the relative amounts of these compounds. CEM I is the type with 95–100 % of clinker. In the raw material from which clinker is made, four major oxides are found, which include calcium oxide (CaO), silicon oxide (SiO₂), aluminium oxide (Al₂O₃) and ferrite oxide (Fe₂O₃). Burning, partial melting and sintering of the raw material can produce the clinker containing four major phases, which are tricalcium silicate (C₃S), dicalcium silicate (C₂S), tricalcium aluminate (C₃A) and tetracalcium aluminate ferrite (C₄AF) [25]. C₃S is responsible for the early strength gain in cement paste and C₂S contributes to the late strength beyond 28 days. C₃A is very reactive, which would hydrate fast with water and cause the phenomenon called flash set. The drawbacks of flash set are that the hydrated C₃A not only contributes barely to the binding or strength of the material, but also spatially prevents the development of other necessary hydrates such as calcium silicate hydrate (C-S-H) and calcium hydroxide (CH) [16]. In order to regulate the rate of early hydration, a small amount of calcium sulfates is added to the cement, which works as C₃A set retarder. The most commonly-used calcium sulfates is gypsum (CaSO₄·2H₂O, simply expressed as $C\bar{S}H_2$), which reacts with C₃A according to Eq. 1.1 and forms an ettringite (3CaO·Al₂O₃·3CaSO₄·32H₂O, simply expressed as $C_6\bar{A}\bar{S}_3H_{32}$)

layer acting as a coating around C_3A grains [26]. In most commercial cements, gypsum is exhausted within the first few hours of hydration. However, ongoing hydration process continues to liberate aluminium from clinker solids [27]. Under this condition, when gypsum is exhausted, previously formed ettringite reacts with the remaining anhydrous C_3A and is converted to calcium aluminate monosulfate ($3CaO \cdot Al_2O_3 \cdot CaSO_4 \cdot 12H_2O$, simply expressed as $C_4\bar{A}\bar{S}H_{12}$), as shown in Eq. 1.2. Therefore, in a hydrated matrix of cement paste, more monosulfate ($C_4\bar{A}\bar{S}H_{12}$) existed than ettringite ($C_6\bar{A}\bar{S}_3H_{32}$) (Fig. 1.1), which is finely intermixed in the C-S-H.

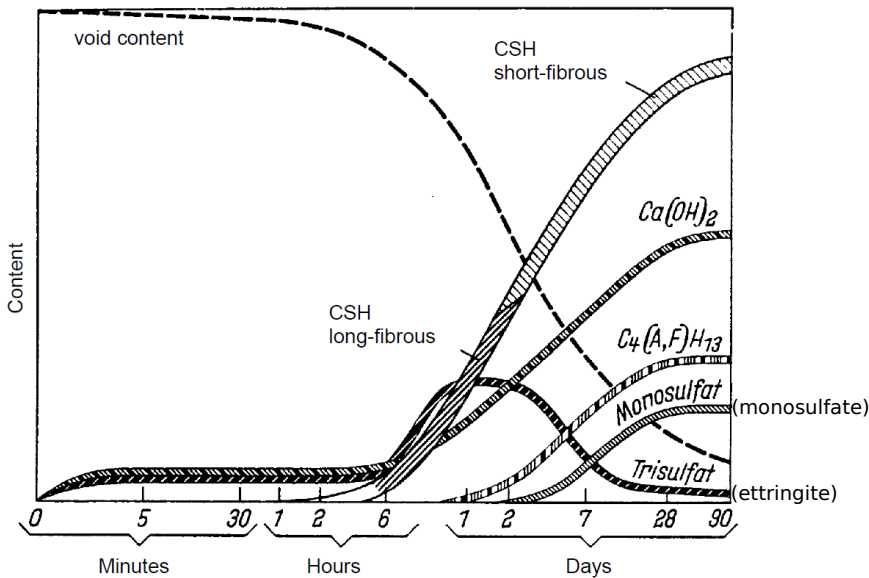
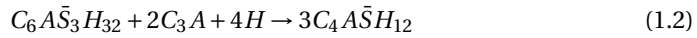
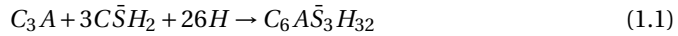


Figure 1.1: Schematic view of the formation of hydrate phases and the structure development during cement hydration according to [1].

Ettringite formed during early hydration is called "primary" ettringite. Since it forms in the plastic stage of the cement matrix, the resulting volume increase does not produce any significant harmful stress. However, the ettringite which forms after the hardening of cement matrix can lead to concrete expansion and degradation, which is called "secondary" ettringite or "delayed" ettringite in some special cases.

Depending on the sulfate source, there are two types of "secondary" ettringite related damage, which are internal and external sulfate attack [28]. Internal sulfate attack (ISA) is caused by excess of internal sulfate (cement with high sulfate content, supplementary materials such as fly ash or slag, gypsum-contaminated aggregate and chemical admixtures [6]) or by thermal decomposition and re-formation of ettringite [28, 29].

It can happen in high-temperature steam cured concrete, large section and mass concrete, railroad concrete ties exposed to the rain and sun alternate actions, etc. External sulfate attack (ESA) occurs when environmental sulfate penetrates into concrete structures in service. Such sources include sulfates from seawater, rivers, groundwater, soil, industrial wastes, atmospheric SO_3 , fertilizers, etc [6].

When hardened concrete is exposed to sulfate environment, external sulfate ions can penetrate from the outside of concrete into the inside through the pore system and react with monosulfate ($C_4A\bar{S}H_{12}$, AFm) to form ettringite ($C_6A\bar{S}_3H_{32}$, Aft), as shown in Eq. 1.3. Thaumasite and gypsum are also possible reaction products. Thaumasite forms normally in presence of an adequate supply of sulfate and carbonate ions at low temperature [30, 31], which is out of the scope of this thesis. Gypsum appears usually when higher sulfate concentrations are present [20–23]. The transformation of monosulfate into ettringite can cause a 2.3-times increase in volume [2]. Unreacted C_3A and C_4AF are also potential sources of aluminium to form ettringite, which can react with the external sulfates. As the pores within cement matrix are filled with expansive chemical reaction solid phases (ettringite), strain develops which leads to stress and cracking. This in turn accelerates further diffusion of external sulfate ions. Therefore, the essential degradation process are diffusion of ions (external sulfate ions), expansive reactions (Eq. 1.3), expansion, cracking and change of strength and permeability, which can be simply illustrated as in Fig. 1.2.

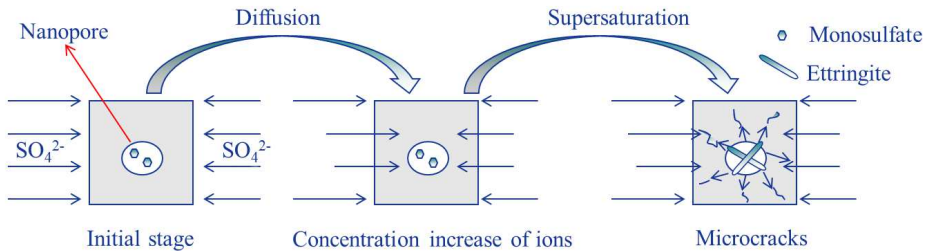
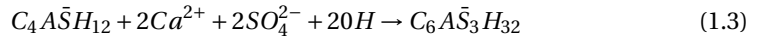


Figure 1.2: Simple description of degradation process caused by external sulfate attack.

1.1.2. EXPOSURE CONDITIONS

ESA-induced degradation is influenced by several factors including the exposure conditions, which can range from continuous immersion to cycles of wetting and drying. Continuous immersion means the concrete is continuously and completely immersed in a sulfate-containing water. This research focuses on the continuous immersion condition.

Wetting and drying cycles with sulfate solutions is another form of exposure which can occur when the level of sulfate-containing water rises and drops, such as ocean tides and changing of underground water level. Cyclic migration of water into concrete can be induced by capillary suction. When soluble sulfate salts, as well as other soluble salts, are concentrated in sufficient amounts, damage of the concrete surface layers can happen.

In a restricted sense, degradation caused by wetting and drying cycles of sulfate solutions is a physical process and other soluble salts may also lead to the same type of damage. However, it is likely that both physical and chemical attack can occur if the wetting and drying processes are slow [32]. It was found that the cyclic exposure to sulfates increased the rate of degradation compared with continuous immersion [33].

Partial immersion in sulfate environment is another severe exposure condition, which can also lead to a more rapid damage compared with continuous immersion [34]. It can happen when the lower portion of a concrete structure is in contact with seawater or moist soil containing sulfates while the upper portion is exposed to a drying environment. An evaporation front is created in this condition. Concrete spalling and scaling can happen in the areas exposed to the drying environment. Both physical and chemical processes are involved in this degradation process.

1.1.3. SOURCES OF EXTERNAL SULFATE

The field conditions of concrete exposed to sulfate are numerous and variable. The aggressive level depends on many factors, such as concentration of sulfate in water, presence of water in the soil and its mobility, concrete quality and service environment.

The primary sources of external sulfate are natural sulfate salts which exist in soils or dissolve in groundwater. The concentration of sulfate in soils or groundwater is normally low. As defined by EN 206 [13], the highest sulfate concentration in groundwater for highly aggressive environment is 6 g/L SO_4^{2-} (Table 1.1). In ACI 201 [14], the severe sulfate concentration in water is defined as 10 g/L (10 000 ppm) (Table 1.2) SO_4^{2-} .

Table 1.1: Limiting values for exposure classes for chemical attack from natural soil and ground water according to EN 206 [13].

Exposure classes	Description of the environment	Sulfate in ground water (SO_4^{2-} mg/L)	Sulfate in soil (SO_4^{2-} mg/Kg)
XA1	Slightly aggressive environment	≥ 200 and ≤ 600	$\geq 2\ 000$ and $\leq 3\ 000$
XA2	Moderately aggressive environment	> 600 and $\leq 3\ 000$	$> 3\ 000$ and $\leq 12\ 000$
XA3	Highly aggressive environment	$> 3\ 000$ and $\leq 6\ 000$	$> 12\ 000$ and $\leq 24\ 000$

Seawater and coastal soil soaked with seawater are another main source of external sulfate. Several ions present in seawater with different concentrations and the main ions are Na^+ , Mg^{2+} , Cl^- and SO_4^{2-} . The typical concentration of SO_4^{2-} in seawater is 2.7 g/L [6].

Agricultural or industrial waste waters may also contain sulfates, such as fertilizer and water from cooling tower. Industrial solid wastes exposed to groundwater or precipitation can be another sulfate source, such as wastes from mining industry, combustion of coal and metallurgical industry. In addition, atmospheric pollution (acid rain) may also contribute to increase sulfate concentration of soil and groundwater. [6, 14]

Domestic sewage typically contains sulfate between 20 and 500 mg/L [35]. Several industrial wastewaters contain much higher concentrations of sulfate, such as the chemical industry producing organic peroxides can generate wastewater with sulfate concentrations ranging from 12 g/L to 35 g/L SO_4^{2-} [36].

One of the methods to accelerate the tests in laboratory is to increase the concentration of sulfate solutions, which can lead to the acceleration of sulfate diffusion and then degradation process. The sulfate concentration of 50 g/L Na_2SO_4 are proposed in ASTM C1012 [37] as the exposure condition, which is equal to 34 g/L SO_4^{2-} . Schmidt et al. [20] used 4 g/L and 44 g/L Na_2SO_4 in their study. Yu et al. [11] chose three concentrations of sulfate solutions containing 3 g/L, 10 g/L and 30 g/L Na_2SO_4 . Müllauer et al. [38] used sodium sulfate solutions with a concentration of 1.5 and 30 g/L SO_4^{2-} at 20 °C, attempting to account for natural and accelerating conditions, respectively. On the other hand, 30 g/L SO_4^{2-} can also occur in severe environment for the natural condition, such as industrial wastewaters mentioned above.

1.2. REVIEW OF LITERATURE ON EXTERNAL SULFATE INDUCED EXPANSION AND DEGRADATION

1.2.1. MECHANISM

EXTERNAL sulfate attack is a complex issue as chemical, physical, and mechanical processes contribute to the degradation. The complexity of the degradation process has produced large amount of studies, however, the controversy about this topic still remains. Three types of macroscopic damage features have been reported: expansion (cracking, spalling), softening and decohesion [16].

Softening is caused by the formation of ettringite and gypsum. Since calcium is needed during the formation processes, softening can lead to a partial decalcification of C-S-H.

Decohesion mainly occurs when thaumasite is formed and replaces the C-S-H. Thaumasite which looks like an incohesive mush forms normally in presence of an adequate supply of sulfate and carbonate ions at low temperature [30, 31]. The formation of thaumasite is favored at low temperatures (0-5 °C) and humid atmospheres [39, 40]. A formation at temperatures up to 25 °C is also possible. However, the formation rate will decrease markedly between 15 °C and 20 °C [6]. The formation also consumes silicon from the C-S-H which can cause a loss of the binding properties of C-S-H.

Regarding the mechanisms of expansion caused by external sulfate attack, several theories exist in the literature, such as swelling, topochemical reaction and crystallization pressure theory. Most of the theories concern the formation of ettringite as the main cause, even though the formation of gypsum may also possibly play a role in the expansion [39, 41].

Scanning electron microscopy (SEM) micrographs indicate that ettringite exists in concrete in various forms, such as spherical clusters of ettringite crystals, crossed or parallel needles with different sizes. Stark and Bollmann [2] found that the large needle-shaped ettringite crystals with a thickness of several microns often consisted of many slender crystals with a thickness between 20 nm and 200 nm lying close to each another, as shown in Fig. 1.3. More examples of ettringite crystals in hydrated cement matrix

are presented in Fig. 1.4. Mehta [42] proposed two types of ettringite crystals. Type one is large lath-like crystals, which could be 10 to 100 μm long and several microns thick. This type of ettringite crystals are formed at low hydroxyl ions concentration. Type two is small rod-like crystals, which are 1 to 2 μm long and 0.1 to 0.2 μm thick or even smaller. This type of ettringite crystals are formed at high hydroxyl ions concentration.

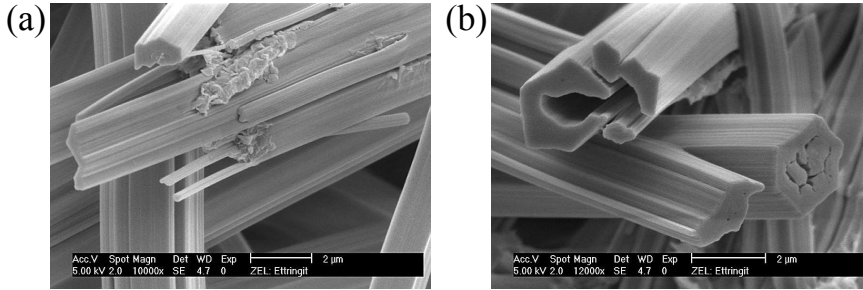


Figure 1.3: SEM micrographs of ettringite crystals. (a) Needle-shaped ettringite crystals with a thickness between 20 nm and 200 nm lying close to large crystals and (b) needle-shaped ettringite crystals with a hexagonal cross-section and a thickness of about 2 μm according to [2].

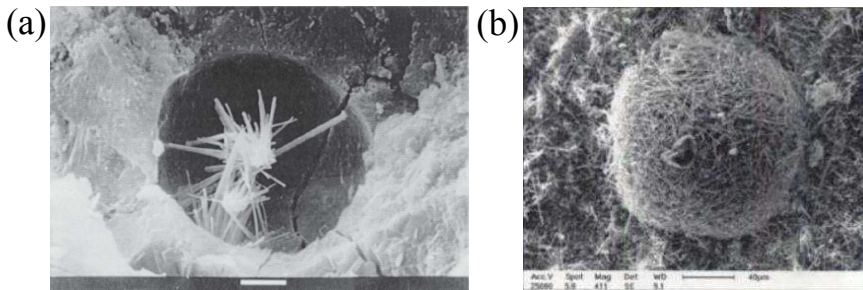


Figure 1.4: SEM micrographs of ettringite crystals. (a) Large long-needle ettringite crystals inside a pore according to [3] and (b) entrained air bubble filled with ettringite crystals according to [4].

SWELLING

Swelling considers ettringite as crystals of colloidal dimensions. Mehta [43] proposed that in the presence of calcium hydroxide, the formed ettringite is colloidal in size. It has a high specific surface and exhibits a net negative charge. When exposed to an outside source of water, the colloidal ettringite can attract a large amount of water molecules, which could cause swelling pressure. But if calcium hydroxide is absent, then ettringite crystals will be larger in size, which can not attract enough water molecules and do not contribute to expansion.

Brown and Taylor [44] stated that swelling is a typical property of gel-like materials, which could take up water and expand without breaking. However, ettringite is not usually observed to be formed as a gel-like material and its internal structure cannot take more than 36 moles of water [45]. In addition, in some situations such as calcium

sulphoaluminate cement, there is no free calcium hydroxide but expansion from ettringite formation still happens [11].

TOPOCHEMICAL REACTION

Topochemical reaction, or solid-solid reaction, is defined as a reaction between a solid particle and a surrounding solution in which the hydration product is formed on the surface of the solid particle [46]. Some authors [47, 48] proposed that the expansive ettringite is formed on the surface of unhydrated tricalcium aluminate grains with external sulfate ions, as a topochemical reaction. Schwiete et al. [49] have reported that ettringite crystals are formed on the surfaces of the C_3A particles without the C_3A being dissolved beforehand.

However, a large difference exists in the crystal structures of ettringite and anhydrous tricalcium aluminate [50]. Mehta [51] believed that the formation of ettringite and its random deposition in other locations is caused by through-solution reaction rather than the topochemical reaction. Monteiro [52] defined the through-solution reaction as the cement compounds dissolve to produce ions in solution that will recombine to form hydration products which directly precipitate from supersaturated solution.

CRYSTALLIZATION PRESSURE THEORY

Even though the theories concerning the exact origin of the expansive pressure are under debate, ettringite formation from monosulfate is generally considered as the major cause [10, 11, 16, 38]. Lothenbach et al. [10] showed that the increase in solid volume caused by external sulfate attack did not exceed the total capillary porosity and concluded formation of ettringite within the hydrated cement matrix led to the observed expansion. Yu et al. [11] provided evidence that sulfate related expansion is linked to the formation of ettringite from fine monosulfate crystals embedded within the C-S-H. Müllauer et al. [38] concluded that the damage is due to the formation of ettringite in small pores (10 to 50 nm) which generates stresses up to 8 MPa exceeding the tensile strength of the binder matrix. Ettringite formation also takes place in larger pores, but the generated stress is negligible. In this case, the most likely expansion mechanism can be the crystallization pressure developing inside the nanopores within the cement paste.

According to the crystallization pressure theory [53–58], the driving force for crystallization pressure is the supersaturation of the pore solution. Then, the crystal growth in the confined space leads to the expansive pressure on the pore walls.

Driving force for crystallization from solution Various estimations of crystallization pressure can be found in the literature, the first of which dates back to Correns [58]. If the solution is supersaturated ($Q/K > 1$), then the growth of the crystal can be prevented by applying a pressure directly on the crystal according to Eq. 1.4 [53–55, 58].

$$P = \frac{R_g T}{V_c} \ln \left(\frac{Q}{K} \right) \quad (1.4)$$

where P represents the pressure that is needed to suppress the growth of the crystal, R_g is the gas constant, T is the absolute temperature, V_c is the crystal molar volume, Q is the ion activity product and K is the equilibrium constant.

Eq. 1.4 reveals that a mechanical pressure applied directly to a crystal increases its solubility. For a crystal which grows in a pore, it is the pore wall that applies stress to suppress the growth. For ettringite, $R_g=8.314 \text{ J/mol} \cdot \text{K}$, $V_c=708.5 \text{ cm}^3/\text{mol}$. $T=293.15 \text{ K}$ [11]. According to Eq. 1.4, the relationship between crystallization pressure (P) and supersaturation ($\frac{Q}{K}$) is shown in Fig 1.5.

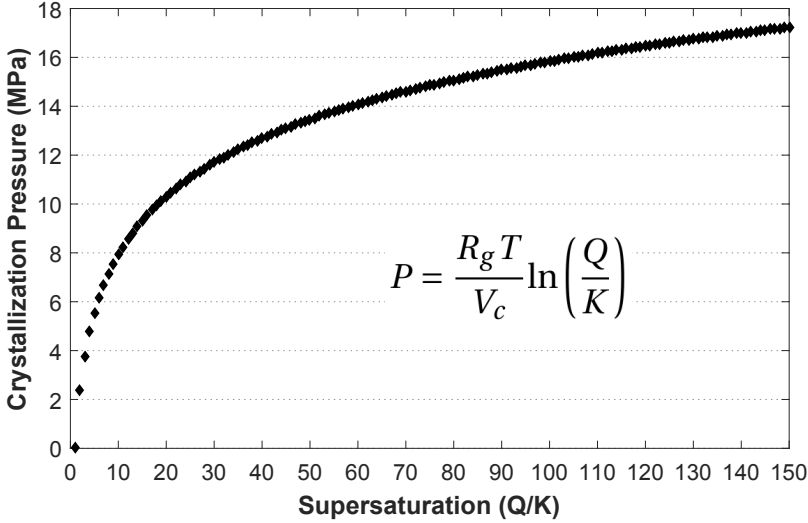


Figure 1.5: The relationship between crystallization pressure (P) and supersaturation (Q/K) for ettringite according to Eq. 1.4.

Surface energy Suppose that a crystal is growing in a supersaturated solution, then, the increase in surface energy resulting from growth is $\gamma_{cl}dA$, where γ_{cl} is the crystal/liquid interfacial free energy, A is the surface area. This increase in energy inhibits the crystal growth. It is equivalent to applying a mechanical pressure (P) on the crystal, so that the crystal needs to do the work (PdV) when it increases in volume (V) [54]. Therefore, the two energies should be equal, as described in Eq. 1.5.

$$\gamma_{cl}dA = PdV \tag{1.5}$$

Another form of Eq. 1.5:

$$P = \gamma_{cl} \frac{dA}{dV} = \gamma_{cl} \kappa_{cl} \tag{1.6}$$

where κ_{cl} represents the curvature of the crystal, which is equal to dA/dV .

For a spherical crystal with a radius r , $A = 4\pi r^2$, $V = 4\pi r^3/3$. Therefore, $\kappa_{cl} = \frac{dA}{dV} = \frac{2}{r}$. Based on Eq. 1.6, the pressure to suppress the growth of a spherical crystal is:

$$P = \gamma_{cl} \frac{2}{r} \tag{1.7}$$

Eq. 1.6 reveals the amount of pressure which should have to be imposed on the crystal to suppress the growth as much as the surface energy does. It can be found that the pressure (P) is related with the curvature of the crystal (κ_{cl}). Therefore, the crystal which grows in a smaller pore needs a higher pressure to suppress the growth. Assuming spherical crystals with a radius r and a crystal/liquid interfacial free energy (γ_{cl}) for ettringite of 0.1 J/m^2 [38], the relationship between crystallization pressure (P) and crystal radius (r) can be drawn, as shown in Fig 1.6.

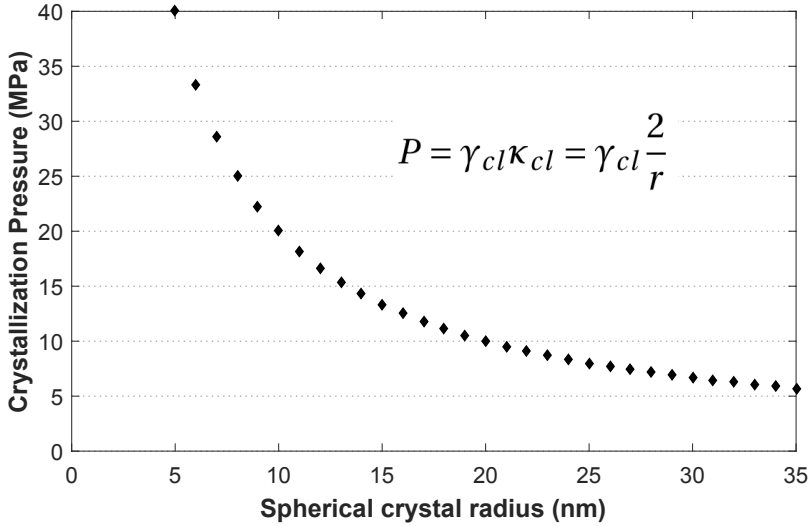


Figure 1.6: The assumed relationship between crystallization pressure (P) and spherical crystal radius (r) according to Eq. 1.6. γ_{cl} of ettringite was used.

Equilibrium requirements The surface energy increases the solubility of the crystal, therefore, a smaller crystal is in equilibrium with a higher concentration [54]. As a result, a crystal having the curvature κ_{cl} is in equilibrium with a certain supersaturation ($\frac{Q}{K}$), as described in Eq. 1.8 [59, 60].

$$\gamma_{cl}\kappa_{cl} = \frac{R_g T}{V_c} \ln\left(\frac{Q}{K}\right) \quad (1.8)$$

The physical understanding of Eq. 1.8 is that an atom on the surface of a small crystal is in a highly energetic condition. Therefore, it has a stronger tendency to hop into the liquid compared with an atom on the surface of a large crystal. As a result, a higher concentration of ions in the adjacent solution is required to maintain the equilibrium, so that a correspondingly high frequency of atoms hopping from the liquid onto the solid can happen [54].

1.2.2. INFLUENCING FACTORS

WATER/CEMENT RATIO

Water/cement (W/C) ratio has always been an important parameter in any durability related experiment. Specimens made with higher W/C ratio result in an increased porosity and permeability [5, 61, 62], as can be found in Fig. 1.7. Therefore, the ingress and movement of external sulfate ions can be reduced by lowering W/C ratio.

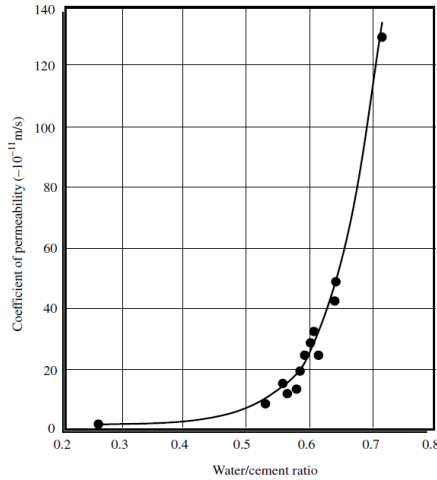


Figure 1.7: Relationship between the coefficient of permeability and W/C ratio for mature cement paste according to [5] and [6].

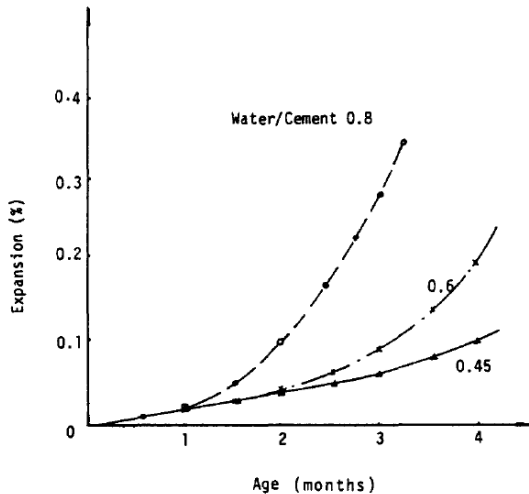


Figure 1.8: Expansion of mortars with different W/C ratio under external sulfate attack according to [7].

Ouyang et al. [7] studied the influence of W/C ratio on the expansion behavior of

cement mortars immersed in a sulfate solution containing 4.3 wt.% magnesium sulfate and 2.5 wt.% sodium sulfate. They concluded that the increase of W/C ratio can lead to a faster rate of expansion, as illustrated in Fig. 1.8. The higher W/C ratio can result in a faster ingress of external sulfate ions and a weaker cement matrix.

Monteiro and Kurtis [63] studied the failure time for concrete with various mixtures and exposed to severe sulfate conditions. They found that the failure time, as measured by expansion, decreases with increasing W/C ratio and C_3A content. The mixtures with W/C ratio below 0.45 and C_3A content below 8 % are in a "safe region".

ACI 201 [14] suggested the maximum W/C ratio and the type of cementitious material for concrete that will be exposed to sulfates, which are listed in Table 1.2.

Table 1.2: Requirements to protect against damage to concrete by sulfate attack from external sources of sulfate according to ACI 201 [14].

Severity of potential exposure	Sulfate (SO_4^{2-}) in water, ppm	Water/cement ratio by mass, max.	Cementitious material requirements
Class 0 exposure	0 to 150	No special requirements	No special requirements
Class 1 exposure	> 150 and < 1 500	0.50	ASTM C150 Type II or equivalent
Class 2 exposure	> 1 500 and < 10 000	0.45	ASTM C150 Type V or equivalent
Class 3 exposure	10 000 or greater	0.40	ASTM C150 Type V plus pozzolan or slag

INITIAL C_3A CONTENT

The chemical composition of cement is another major factor influencing external sulfate attack. Among the cement hydration products, the alumina-bearing phases is more susceptible to sulfate attack, which are mainly originally from C_3A [64]. The sulfate resistance of cement generally decreases with an increase in its initial C_3A content [65–67], due to the proportional correlation between the amount of C_3A in cements and the potential for ettringite formation. Therefore, the maximum C_3A content are normally limited in standards for sulfate resistance of cements.

Ouyang et al. [7] studied the influence of C_3A content for the cement mortars immersed in a sulfate solution containing 4.3 wt.% magnesium sulfate and 2.5 wt.% sodium sulfate. The expansion of specimens with different C_3A content by mass (4.3 %, 7 %, 8.8 % and 12 %) can be found in Fig. 1.9. Specimens containing more C_3A appeared to have larger expansion.

Hossack and Thomas [68] investigated the effect of C_3A content on the severity of sulfate attack. Clinkers with two different C_3A content were used, which are 8–9 % C_3A and 11–12 % C_3A . Mortar bars with a water/cementitious materials ratio of 0.485 were exposed to a 5% sodium sulfate solution. They found that the mortar bars with high C_3A content failed much sooner than that with low C_3A content in 5 °C sulfate solution. On average, the C_3A -rich mortar bars failed in half the time of the low C_3A mortar bars.

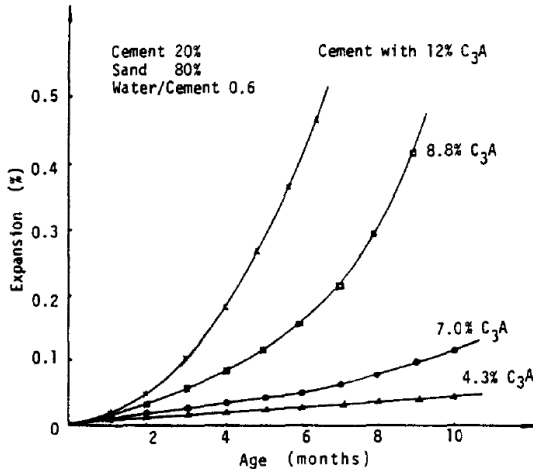


Figure 1.9: Expansion of mortars with different C₃A content under external sulfate attack according to [7].

In ASTM C150 [69] test method, Type II portland cement is for the use when moderate sulfate resistance is desired and Type V portland cement is for the high sulfate resistance. Type II and Type V portland cements are specified to have a maximum C₃A content of 8 % by mass and 5 % by mass, respectively. ACI 201 [14] test method also has the similar requirements, as shown in Table 1.2.

The chemical composition of the Portland cement can be determined by X-ray fluorescence (XRF) spectrometry method. Then the corresponding mineral composition can be calculated with the Bogue equation [70]. One experimental result from our laboratory about the mineral composition of Portland cement (CEM I 42,5N) is listed in Table 1.3 [15]. The Portland cement is produced by ENCI, the Netherlands. Therefore, the initial C₃A content of the cement used in this research should be around 7.9 wt.%.

Table 1.3: Mineral composition of Portland cement (CEM I 42,5N) calculated by Bogue equation according to [15].

Compound	C ₃ S	C ₂ S	C ₃ A	C ₄ AF	Total
Weight (%)	64.1	13.0	7.9	8.1	93.1

TYPE OF SULFATE SOLUTION

Practically, different types of sulfates can be involved in the external sulfate attack on concrete structures, since SO₄²⁻ anions are always bound to a counter cation, such as Na⁺, Ca²⁺, Mg²⁺ and K⁺ in the field. Various types of sulfates have a direct influence on the formed products and the attack process, which is addressed by numerous researchers.

Santhanam et al. [71] studied the expansion of mortar bars (CEM I, water to cement ratio of 0.485, 6 mm × 15 mm × 80 mm) exposed to sodium sulfate and magnesium sul-

fate solutions. They concluded that sodium sulfate solution led to a faster expansion compared to magnesium sulfate solution. ACI 201 [14] mentions that solutions containing calcium sulfate are generally less aggressive than solutions containing sodium sulfate.

Kunther et al. [8, 9] investigated the length change of mortar bars (CEM I, water to cement ratio of 0.55, 25 mm × 25 mm × 150 mm) exposed to four types of sulfate solutions, which are sodium sulfate (50 g/L), potassium sulfate (61 g/L), magnesium sulfate (44.8 g/L) and a mixture solution containing sodium sulfate, potassium sulfate, magnesium sulfate and calcium sulfate. The experimental results are shown in Fig. 1.10. It can be found that the specimens in potassium sulfate solution expanded fastest followed by the specimens in sodium sulfate solution. The specimens in magnesium sulfate solution and the mixture solution presented smaller expansions.

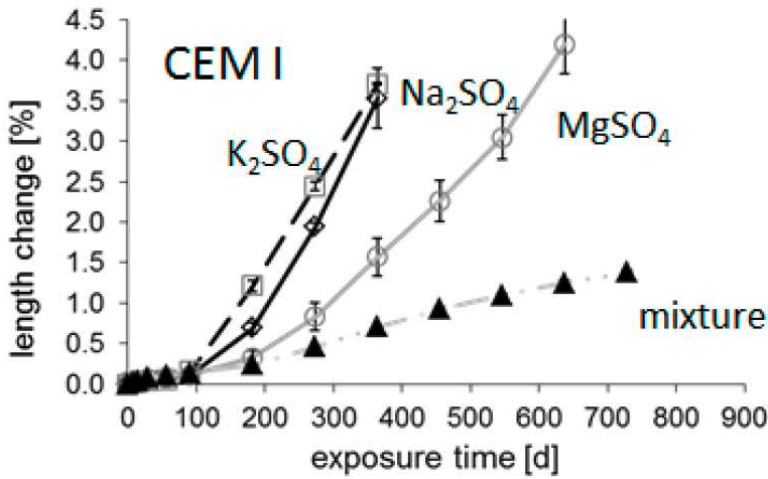


Figure 1.10: Length change over time for different sulfate solutions for mortar bars made with CEM I cement according to [8, 9].

Sodium sulfate (Na_2SO_4) Sodium sulfate solution is the most commonly used sulfate solution in experiments. Sulfate ions in a solution can penetrate into the cementitious materials and react with monosulfate to form ettringite, as shown in Eq. 1.3. Ca^{2+} is needed in this process, however, Na_2SO_4 can only offer Na^+ instead of Ca^{2+} . Therefore, firstly, source of Ca^{2+} in this process is portlandite (calcium hydroxide), which is mainly produced when C_2S and C_3S react with water during cement hydration. The expansion caused by ettringite formation is the main problem in this type of degradation [72].

Furthermore, when portlandite is consumed, it is possible that the existing C-S-H phase begins to decompose to supply Ca^{2+} for further reactions [17]. In this condition, besides expansion, cement paste also starts gradually to lose its strength and binding property.

On the other hand, if the alumina-bearing compounds (such as monosulfate or C_3A) are not available, gypsum begins to form instead of ettringite formation [17].

Potassium sulfate (K_2SO_4) Generally, potassium sulfate and sodium sulfate are assumed to interact similarly with cement hydrates and therefore have a similar degradation type. They are often discussed together using the term alkali sulfates [9, 17].

Calcium sulfate ($CaSO_4$) Compared to sodium sulfate and magnesium sulfate, calcium sulfate is typically considered to be the least aggressive sulfate salt [17]. For the calcium sulfate in the field, the amount of sulfate ions which are able to penetrate into the concrete is limited due to its low solubility in water (around $1.46 \text{ g/L } SO_4^{2-}$ at 20°C) [27].

Calcium sulfate also reacts with monosulfate to form ettringite, which results in expansion. However, unlike in other sulfate solutions, Ca^{2+} is available in the calcium sulfate solution. Therefore, there is no need for the decomposition of portlandite or C-S-H to supply Ca^{2+} for the reactions. In addition, it is expected that the presence of calcium in the solution reduces calcium leaching [17, 73], since calcium ions in the solution decrease the diffusion gradient of calcium concentration. Calcium leaching can accelerate sulfate attack since it leads to a more porous microstructure and therefore external sulfate ions can penetrate more easily [16].

Magnesium sulfate ($MgSO_4$) Magnesium sulfate solution is the second most commonly used sulfate solution in experiments. Magnesium sulfate can initially react with calcium hydroxide in the hydrated matrix, which leads to the formation of brucite ($Mg(OH)_2$) and gypsum [72, 74]. Brucite precipitates as a layer on the surface of the specimen, which is often accompanied by a layer of gypsum that forms in the same reaction on the inside of the brucite layer [74]. The dense brucite layer on the specimen surface can act as a protective layer to reduce the permeability, which is considered to be responsible for the reduced sulfate penetration and expansion [9, 75].

On the other hand, brucite has a very low solubility and its saturated solution has a pH of about 10.5 [22]. C-S-H is unstable in low pH conditions, therefore formation of brucite causes the decomposition of C-S-H to calcium hydroxide in order to maintain the pH balance in the system [72]. As long as magnesium sulfate is available, calcium hydroxide will be consumed to form brucite, which causes a further decomposition of C-S-H. Brucite also reacts with silicate hydrate arising from the decomposition of C-S-H, and this leads to the formation of magnesium silicate hydrate (M-S-H), which is lack of cohesive properties [76]. Therefore, the main problem for this type of degradation is loss of strength and disintegration of concrete due to decomposition of C-S-H, other than expansions due to ettringite formation [17].

SULFATE CONCENTRATION

Increase of sulfate concentration in solutions can accelerate the ingress of external sulfate ions and then the expansion and degradation processes. Ferraris et al. [77] found that the concentration of sulfate solutions played an important role in the rate of specimen expansions. A higher concentration of sodium sulfate solutions resulted in a faster expansion of specimens. The same conclusion was also drawn by many other researchers [11, 71, 78].

On the other hand, high sulfate concentrations can lead to the precipitation of gypsum, while no or limited gypsum can be found in low sulfate concentrations [21, 39, 79]. Schmidt et al. [20] studied the physical and microstructural changes caused by external sulfate attack. The mortar bars (10 mm × 40 mm × 160 mm) were immersed in solutions of 4 g/L and 44 g/L Na₂SO₄. They concluded that the higher concentration led to the formation of gypsum, which did not happen in the low concentration. Schmidt et al. [20] and Lothenbach et al. [10] investigated the phase changes in two types of sulfate concentrations through thermodynamic models and compared the numerical results with their experimental observations. The simulations also showed the presence of gypsum in 44 g/L Na₂SO₄ solution and the absence of gypsum in 4 g/L Na₂SO₄ solution, as presented in Fig. 1.11. However, in some other studies, gypsum was also found in cement pastes when exposed to a low sulfate concentration, such as 2.1 g/L sodium sulfate solution [79] and 3 g/L sodium sulfate solution [80].

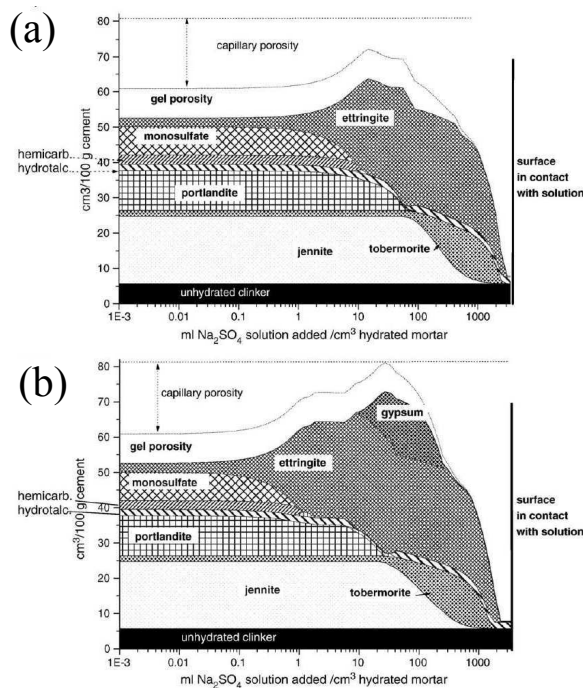


Figure 1.11: Phase assemblage of the mortar specimens immersed in (a) 4 g/L Na₂SO₄ and (b) 44 g/L Na₂SO₄ solutions as calculated with GEMS according to [10].

1.2.3. GEOMETRY OF SPECIMENS

External sulfate attack under continuous immersion condition is governed by a slow diffusion process. Even though high W/C ratios and high sulfate ion concentrations have been adopted as acceleration methods, research shows that the attack depth remains shallow even after several months. Yu et al. [11] acquired sulfur profiles through EDS

elemental mapping methods for mortars (CEM I, W/C ratio 0.55) submerged in sodium sulfate solutions with three types of concentrations. It seems that the external sulfate can reach the depth of around 4 mm after 120-day exposure and around 5 mm after 240-day exposure to 30 g/L sulfate solution. Samson et al. [81, 82] found the external sulfate ions can reach the depth of around 4 mm after 90 days, around 5mm after 180 days and around 8 mm after 360 days for cement paste (Canadian CSA Type 10, W/C ratio 0.60) exposed to 50 mmol/L sodium sulfate solution. Kunther [9] concluded the external sulfate ions can reach the depth of around 3.5 mm after 91 days and around 9 mm after 273 days for mortars (CEM I, W/C ratio 0.55) immersed in 0.35 mol/l sodium sulfate solution. Therefore, specimens with a small thickness along the diffusion direction could be preferred for experimental research in order to ensure a faster exposure of the entire cross-section.

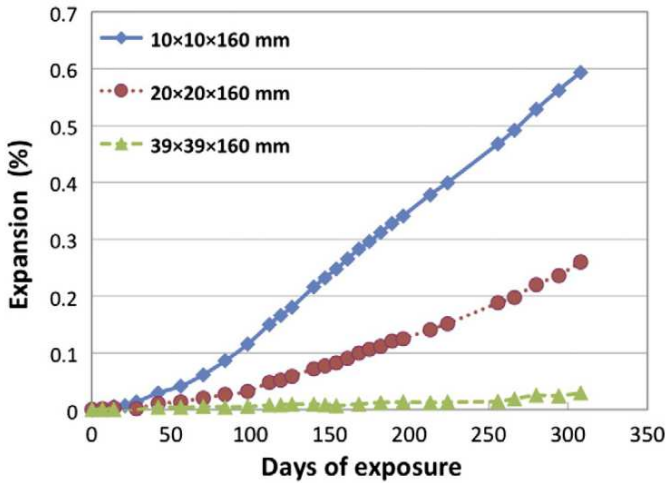


Figure 1.12: Expansion of mortars (CEM I, W/C ratio of 0.55) with different size in 3 g/L sodium sulfate solution according to [11].

ASTM C452 [83] and ASTM C1012 [37] test methods provide a procedure of measuring length change of mortar specimens immersed in sulfate solutions. The dimensions of test specimens is 25 mm × 25 mm × 285 mm [83]. Several other dimensions can also be found in the literature, such as 25 mm × 25 mm × 150 mm (mortar) [9], 40 mm × 40 mm × 160 mm (mortar) [84], 10 mm × 10 mm × 160 mm (mortar) [11] and 6 mm × 15 mm × 80 mm (mortar) [71]. The measurement of expansion according to ASTM C1012 is based on the assumption that the whole specimen is expanding at the same time, however, it was observed that only a small fraction of the entire cross section is responsible for the measured expansion [85]. In this case, the expansive part is restrained by the original part which is not reached by external sulfates yet. As the expansion is expressed as a percentage of the total length of the whole specimen, the real expansion of the area affected by sulfates should be much larger than the measured expansion. As presented in Fig. 1.12, Yu et al. [11] studied the expansion behavior of mortars bars with different sizes immersed in 3 g/L sodium sulfate solution and found that the specimens with

smaller size expanded faster. On the other hand, besides the expansion measurement as the most common method to evaluate the sulfate resistance, several other parameters are also used as the indications of degradation, such as loss or increase of mass, strength and elastic modulus decrease [78, 86]. Considering the small area fraction affected by sulfates, the specimens with relative large size seem almost impossible to reflect the real changes of the whole specimens for the indications mentioned above. Therefore, reducing the cross section of specimen is proposed in this research.

The thin-walled hollow mortar cylinders (diameter 30.0 mm, wall thickness 2.5 mm) assembled with different diameters of central steel bars were used in Müllauer et al [38], which was originally developed to study the hygral stress produced in dry hardened cement paste after saturation with water [87]. Inspired by their research, the same dimensions of specimens were used in this research. More information on this can be found in section 2.2.1. Cement paste was chosen over mortar and concrete, with the purpose of eliminating the influence of aggregates and reaching a relatively uniform distribution of local expansive pressure at each attack depth. Bonakdar et al. [12] found that an increase of sand fraction can lead to the increase of specimen expansions when they have the same exposure to 10 % sodium sulfate solution (Fig. 1.13). Therefore, considering the heterogeneities of material and internal expansive pressure distribution, more severe damage is likely to occur in concrete compared to cement paste.

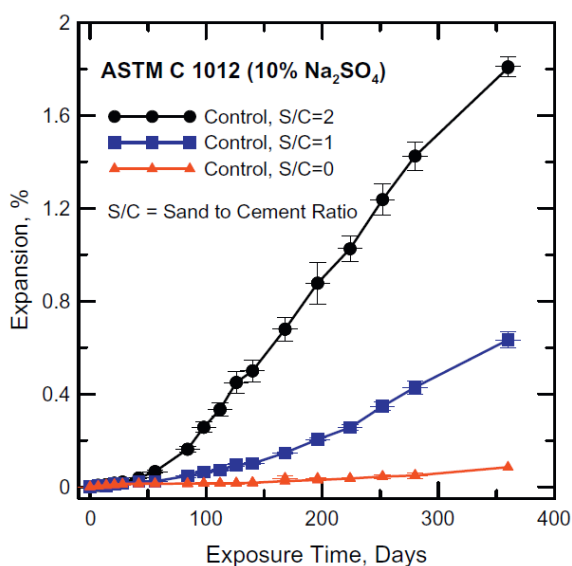


Figure 1.13: Expansion of mortars (CEM I, W/C ratio of 0.5) with different sand/cement ratio in 10 % sodium sulfate solution according to [12].

The ESA-induced expansions are rather small, especially for the restrained pipes in this research, which are in a range of several microns. In order to obtain accurate expansion data, a new technique is developed in this research for measuring the expansions.

1.3. OBJECTIVES OF THIS RESEARCH

THE main goal of this research is to obtain a complete experimental dataset regarding the process of specimen expansion and degradation when exposed to sulfate solutions, and simulate the process based on the experimental observations. The study contains the following objectives:

- External sulfate attack is a complex issue which can lead to internal expansive pressure inside the pore network of cement paste. However, the theories concerning the exact origin of the pressure are still under debate. Even though the crystallization pressure theory has become the most widely cited hypothesis, more evidences for this mechanism are still needed. Therefore, the first objective in this study is to offer experimental evidences for supporting crystallization pressure theory.
- The magnitude of the internal expansive pressure caused by external sulfate attack is still missing in the literature. Therefore, the second objective is to measure or estimate the expansive pressure at different scales.
- For the engineering practice, the concrete structures are exposed to different sulfate concentrations and subjected to different restrained levels. The third objective is, therefore, to study the influences of sulfate concentrations and external restraining levels.
- The development of pressure gradient has been largely neglected in the current literature. The specimen with a large dimension is normally used in the current researches, however, the measured results are in fact an overall consequence which is caused by the gradient of internal expansive pressure. Therefore, the fourth objective is to study the influence of the pressure gradient. In addition, the process of crack initiation and propagation is also investigated.
- Based on the experimental observations, the expansion and degradation processes of the specimens exposed to sulfate solutions can be simulated. In addition, the simulated results can be compared with the experimental results. Therefore, the fifth objective in this study is to validate the numerical simulations by experiments.

1.4. OUTLINE OF THE THESIS

THE thesis discusses the durability problem caused by external sulfate attack. Laboratory experiments and numerical simulations are both used to investigate the degradation mechanism, expansive pressure and cracking process. It is divided into seven chapters, including an introduction and literature review (chapter 1) and conclusions and discussion (chapter 7). The outline of this thesis is given in Figure 1.14.

In chapter 1, an introduction of the PhD work is given. The degradation process caused by the ingress of external sulfate ions are described. Sources of external sulfate and exposure conditions are summarized. The mechanisms which lead to the expansion and degradation are reviewed. The factors affecting sulfate-induced degradation

are discussed. Dimension and shape of specimens in the literature are also reviewed. In the end, the reasons for the experimental setup used in this research are explained. Finally, the aims of this research are formulated.

Chapter 2 - 4 deal with the experimental part of the research. Cement paste pipes with a wall thickness of 2.5 mm are chosen. Three types of longitudinal restraints and two types of sulfate concentrations are considered. Chapter 2 presents an experimental study on the expansion behavior of cement paste pipes. In order to investigate the reason to cause the expansion, the change of pore size distributions is studied. In addition, the expansions and generated stresses of the specimens are quantified during sulfate immersion tests. However, the measured generated stress is caused by a gradient of internal expansive pressure, which is related with the sulfur gradient. Therefore, the sulfur gradient is periodically analyzed in chapter 3. Moreover, the 3D crack patterns of the specimens under three types of restraints are also studied in chapter 3. The different crack patterns due to restrained level are discussed. Chapter 4 studies the complex process of crack initiation and propagation during material degradation at microscopic scale.

Chapter 5 and 6 deal with the modeling part of the study. Delft lattice model is used. The fracture of materials under external loading is simulated in chapter 5. The damage of materials due to internal loading is modeled in chapter 6. Chapter 5 focuses on the uniaxial tensile simulations. The mechanical properties of cement paste pipes after 90-day curing are studied experimentally and numerically. The local mechanical properties of cement paste lattice elements obtained in chapter 5 are used in chapter 6. Chapter 6 presents a numerical study on expansion and degradation processes of the specimen immersed in strong sulfate solution (30 g/L) under high-restraint condition (7 mm), which are investigated experimentally in chapter 2 and 3.

In chapter 7, the work in this thesis are briefly summarized. Moreover, general conclusions and findings of this research are presented and discussed. Finally, recommendations for further research are given.

Cement paste degradation under external sulfate attack *An experimental and numerical research*

Part 1: Introduction and literature review (Chapter 1)

Part 2: Experimental investigations (Chapters 2-4)

Experimental study on cement paste pipe expansion due to external sulfate attack (Chapter 2)

Microanalysis of cement paste degradation caused by external sulfate attack (Chapter 3)

Microstructural evolution of cement paste exposed to strong sodium sulfate solution (Chapter 4)

Part 3: Numerical investigations compared with experimental analyses (Chapters 5-6)

Experimental and numerical study on mechanical properties of cement paste pipe without sulfate exposure (Chapter 5)

Mesoscale modeling of expansion and damage of cement paste pipe in strong sodium sulfate solution (Chapter 6)

Part 4: Conclusions and discussion of results (Chapter 7)

Figure 1.14: Outline of the thesis.

PART 2: EXPERIMENTAL INVESTIGATIONS

2

EXPERIMENTAL STUDY ON CEMENT PASTE PIPE EXPANSION DUE TO EXTERNAL SULFATE ATTACK

This chapter presents an experimental study on the expansion behavior of specimens immersed in sodium sulfate solutions with SO_4^{2-} ion concentrations of 1.5 g/L and 30 g/L. The procedure of preparing the cement paste pipes with a wall thickness of 2.5 mm was described. The test setup of longitudinal restraints and the strain gauge measurement system were introduced. The free expansion, restrained expansion and generated stress were quantified. The pore size distribution was periodically analyzed.

2.1. INTRODUCTION

EXTERNAL sulfate attack is a progressive degradation process that may cause expansion, cracking, loss of binder cohesion and increased permeability in cementitious materials. Crystallization pressure theory has often been referred to as the most likely mechanism. However, thus far the stress causing the expansion has not been quantified.

According to the crystallization pressure theory [53–56], the driving force for crystallization pressure is the supersaturation of the pore solution. Then, the crystal growth in the confined space leads to the expansive pressure on the pore walls. An inverse relationship between the expansive pressure and the pore size is critical. Müllauer et al. [38] calculated a spherical crystal with a radius of around 25 nm and found that this is in equilibrium at a maximum pressure of around 8 MPa. Yu et al. [11] also calculated the crystallization pressure as high as 21 MPa from a supersaturated solution to form ettringite. The magnitude of the expansive pressure on the walls of nanopores can be predicted based on the crystallization pressure theory. However, an experimental verification is still missing since direct measurement of the expansive pressure on nanopore walls is highly challenging. Therefore, in this chapter, the expansion behavior of larger scale specimens under various degrees of restraint was studied experimentally, which was proposed to be used for the investigation on the magnitude of expansive pressure on nanopore walls indirectly.

External sulfate attack under continuous immersion condition is a slow diffusion process. Even though high water/cement ratios and high sulfate ion concentrations have been adopted as acceleration methods, research shows that the attack depth remains shallow even after several months [11, 82]. Therefore, specimens with a small thickness along the diffusion direction could be preferred for experimental research in order to ensure a faster exposure of the entire cross-section. In this research, the specimen with a pipe shape was chosen and the wall thickness was only 2.5 mm. In order to eliminate the influence of aggregates and reach a relatively uniform distribution of local expansive pressure at each attack depth, cement paste specimens were chosen over mortar and concrete. Three types of longitudinal restraints were applied on the specimens before exposure, which were created by a spring, a thin or a thicker stainless steel bar that was centered in the hollow specimens. Strain gauges were glued on the steel bars and used for the measurements under restrained conditions, with the purposes of increasing the measurement accuracy and obtaining continuous experimental results. In this chapter, the free expansion, restrained expansion and generated stress were quantified during exposure to two concentrations of sodium sulfate solutions. The pore size distributions were also periodically analyzed.

2.2. MATERIALS AND METHODS

2.2.1. SPECIMEN PREPARATION AND TEST SETUP

IN this study, cement paste specimens with a water/cement ratio of 0.40 were prepared by using ordinary Portland cement, CEM I 42,5 N, produced by ENCI, in the Netherlands. PVC moulds with stainless steel rods in the center (Fig. 2.1) were fabricated in order to produce the cement paste pipes with a wall thickness of 2.5 mm (outer diameter 30 mm, inner diameter 25 mm) and a length of around 95 mm [38, 88, 89]. During

casting of the cement paste pipes, the moulds were put on a vibration table to make the casting easier and also remove the air from the fresh paste. Then the moulded specimens were wrapped with plastic foil and kept in curing room (20 ± 1 °C, 96 ± 2 % RH) for 24 hours. After that, the specimens were demoulded and cured in saturated limewater at 20 ± 1 °C for another 90 days. Upon completion of the curing period, the cement paste pipes were cut and polished at both ends to ensure that they were parallel and that the length was 70 mm.

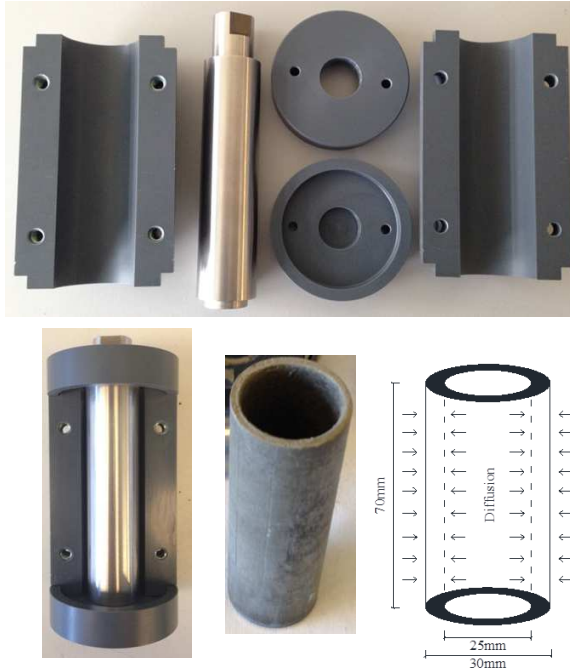


Figure 2.1: PVC moulds and specimens.

Three types of longitudinal restraints were applied on the cement paste pipes in this study [38, 88, 89]. The restraints were created by a spring, a thin stainless steel bar or a thicker stainless steel bar that were centered in the pipes in order to facilitate the non-, low- or high-restraint condition (Fig. 2.2). The middle part diameters of thin steel bars and thick steel bars are 3 mm and 7 mm, respectively. Strain gauges were used for the thin and thick steel bars to measure the deformation of the bars and determine the restraint and resulting stresses. In order to reduce the influence of bending during tests, two strain gauges were glued on the opposite side of the middle part of each steel bar, and the average reading of the two strain gauges was used as the final strain. Then a special coating was applied on the surfaces of strain gauges to protect the strain gauges when exposed to sulfate solutions. The strain values of the strain gauges were measured continuously with a CompactDAQ system connected to a computer.

After 90 days of curing in saturated limewater, the cement paste pipes were assembled with the three types of longitudinal restraints. In order to ensure a firm contact be-

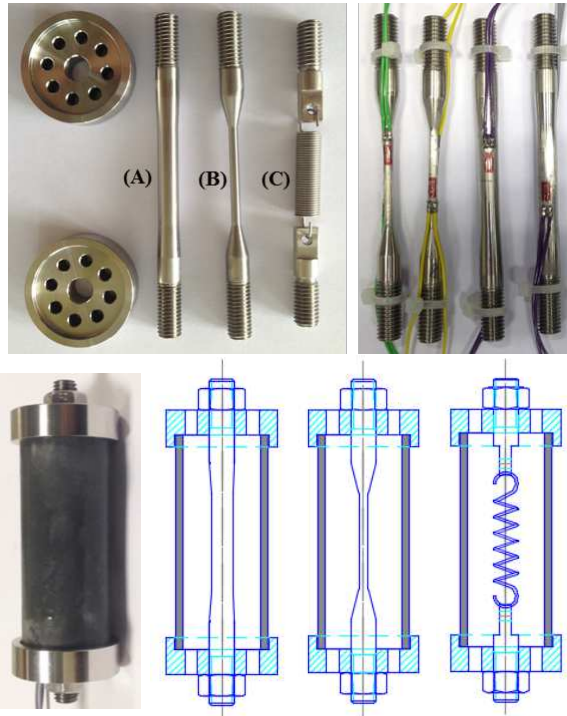


Figure 2.2: Three types of restraints; (A) thick steel bar (high-restraint, diameter of 7 mm), (B) thin steel bar (low-restraint, diameter of 3 mm) and (C) spring (non-restraint).

tween the steel disks and specimens under low- and high-restraint conditions, 0.7 N-m was imposed on the nuts with a precision torque wrench. Then the whole system was immersed in sodium sulfate solutions with the SO_4^{2-} ion concentrations of 1.5 g/L and 30 g/L (Fig. 2.3), attempting to account for natural and accelerating conditions, respectively. For each exposure condition, several additional specimens were also immersed in sulfate solutions, however these additional specimens did not have any restraint thus were able to expand freely. These unrestrained specimens were used for MIP (mercury intrusion porosimetry), SEM (scanning electron microscope) - EDS (energy dispersive X-ray spectrometry) microanalysis and CT (X-ray computed tomography) scanning. The immersion tests were carried out in a room with a constant temperature at 20 ± 1 °C. The temperature of each sulfate solution was monitored by temperature sensors during the tests, considering the sensitivity to temperature change of steel bars and strain gauges. The sulfate solutions were renewed every two weeks until 238-day immersion and from there on every four weeks to keep the strength of the solution stable.

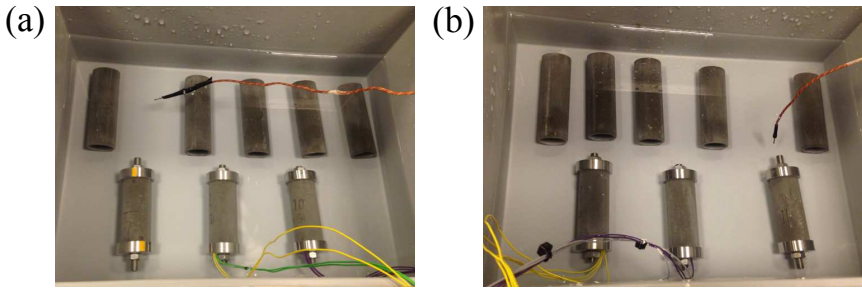


Figure 2.3: Specimens immersed in sodium sulfate solutions with two different SO_4^{2-} ion concentrations; (a) 1.5 g/L and (b) 30 g/L.

2.2.2. CALIBRATIONS OF EXPERIMENTAL SETUP

Two types of calibrations of the strain gauge measurement system were needed for the calculations of restrained expansion and generated stress, which were done before the immersion tests. The two types of calibrations were the tensile test calibration and the torque test calibration, with the purposes of obtaining the force-strain curves and the relationship between local strain and total strain of the steel bars, respectively.

A uniaxial tensile test was performed on each steel bar. The obtained force-strain responses were presented in Fig. 2.4, where the strain is acquired from the strain gauges ($\epsilon_{\text{strain gauge}}$ in Eq. 2.1). The four steel bars were used for the specimen immersed in 1.5 g/L (steel bar 1 and 3) and 30 g/L (steel bar 2 and 4) sodium sulfate solutions, respectively. The middle part diameters of thin steel bars (steel bar 1 and 2) and thick steel bars (steel bar 3 and 4) are 3 mm and 7 mm. Based on the obtained force-strain curves (Fig. 2.4), K_{tensile} in Eq. 2.1 was calculated for each steel bar, which is shown in Table 2.1.

$$\frac{F}{A} = K_{\text{tensile}} \cdot E \cdot \epsilon_{\text{strain gauge}} \quad (2.1)$$

where $\epsilon_{\text{strain gauge}}$ represents the strain of the strain gauge, F is the applied tensile force,

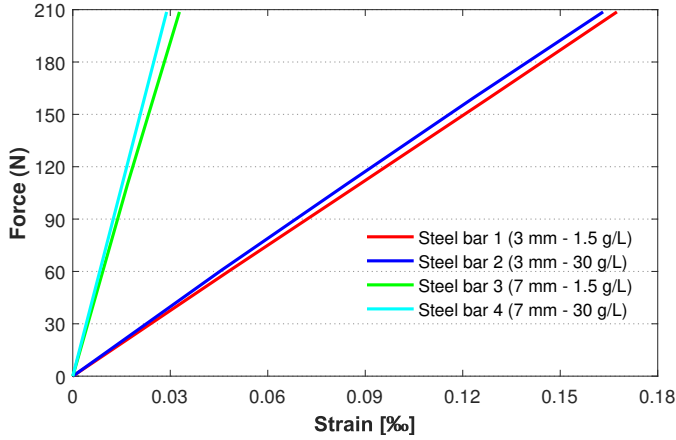


Figure 2.4: Force-strain responses of steel bars subjected to uniaxial tensile load along longitudinal direction.

A is the cross-sectional area of the steel bar where strain gauges are located, E is the Young’s modulus of the steel bar which is 193 GPa, $K_{tensile}$ is the value that needs to be obtained through tensile test calibration.

Table 2.1: The obtained values after two types of calibrations

	Steel bar 1	Steel bar 2	Steel bar 3	Steel bar 4
$K_{tensile}$	0.9151	0.9572	0.8684	0.9734
K_{torque}	0.4092	0.4290	0.6210	0.6989

The cross-sectional areas were different along the longitudinal direction of each steel bar, so the strain varied for different parts of a given steel bar when the longitudinal load was applied at the ends. Strain gauges were glued in the middle part of the steel bars, where the diameter was minimum. The local strain ($\epsilon_{strain\ gauge}$ in Eq. 2.2) can be recorded continuously during the immersion tests, however, the total strain ($\epsilon_{steel\ bar}$ in Eq. 2.2) is needed for the calculation of specimen expansion. Therefore, the torque test calibration was carried out. The steel bars were assembled with an aluminum pipe whose length was 70 mm. Thereafter, a defined increment of certain torque value was applied at each step by means of a precision torque wrench. During this process, the local strain was recorded by computer. At the same time, the corresponding total strain was calculated based on the measurement of entire steel bar length change using a digital indicator. The setup of torque test calibration is shown in Fig. 2.5. The linear relationship between local strain and total strain can be expressed in Eq. 2.2. K_{torque} of each steel bar was calculated after the torque test calibration, which is presented in Table 2.1.

$$\epsilon_{steel\ bar} = K_{torque} \cdot \epsilon_{strain\ gauge} \tag{2.2}$$

where $\epsilon_{steel\ bar}$ represents the strain of the entire steel bar, $\epsilon_{strain\ gauge}$ stands for the

strain of the strain gauge, K_{torque} is the value that needs to be obtained through torque test calibration.

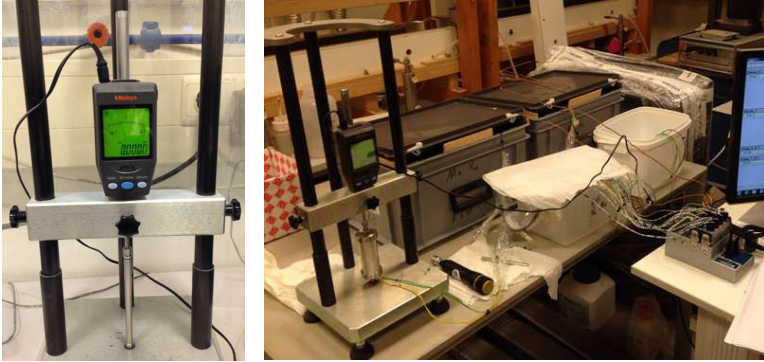


Figure 2.5: Setup of torque test calibration.

2.2.3. CALCULATIONS OF EXPANSION AND GENERATED STRESS

In this study, expansion is expressed as the strain of the cement paste pipe along the longitudinal direction, which is equal to the increased length divided by the original length of the specimen (70 mm). The free expansion stands for the expansion under non-restraint condition with a spring being assembled, which was measured at every 14 days up to a total of 98-day immersion. After that, the measurements were carried out at every 7 days. For every measurement, the specimens were taken out from the solutions and the length changes were recorded by comparing with a reference steel rod using a digital indicator. The measurement process was finished very fast to prevent the specimens from drying. The reference steel rod was kept in a constant temperature room to avoid temperature influences.

The restrained expansion represents the expansion under low- or high-restraint condition created by a thin steel bar (3 mm) or a thicker steel bar (7 mm). During immersion tests, the local strain ($\epsilon_{strain\ gauge}$ in Eq. 2.2) was recorded by computer. Then the total strain ($\epsilon_{steel\ bar}$ in Eq. 2.2) was calculated based on Eq. 2.2. Therefore, the increased length of the entire steel bar was acquired, which is equal to the increased length of the specimen. After that, the restrained expansion of specimen was calculated.

The generated stress means the compressive stress acting on the cement paste pipe at the restrained boundaries due to the restraint by the steel bars, which was originally caused by the interaction between the external sulfate ions and the hydration products. The specimens were expected to expand because of external sulfate attack. Therefore, the steel bars were under tensile force, which led to the same compressive force on the specimens. During the immersion tests, the readings of the strain gauges ($\epsilon_{strain\ gauge}$ in Eq. 2.1) were recorded continuously by computer. Then, based on Eq. 2.1, the tensile forces (F) in the steel bars were calculated, which are equal to the compressive forces exerted on the cement paste pipes. The generated stresses were obtained through dividing the compressive forces by the cross-sectional area of the specimens.

2.2.4. MERCURY INTRUSION POROSIMETRY

Mercury intrusion porosimetry (MIP) is a widely used technique to measure both porosity and pore size distribution of cementitious materials [90–92]. It provides a fast method to characterize the pore structure. Porous material is put into a low-pressure chamber firstly and then a high-pressure chamber. The chamber is evacuated and the samples are surrounded by mercury. The external pressure on the mercury is gradually increased, which leads to the intrusion of mercury into the pores. Assuming the pores are cylindrical, the relationship between the pore diameter (d) and the applied pressure (p) can be expressed by the Washburn equation [93].

$$p = -\frac{4\gamma \times \cos\theta}{d} \quad (2.3)$$

where γ is the surface tension of the mercury (mN/m) and θ is the contact angle between the mercury and the pore surface of the material. By applying the Washburn equation, mercury intrusion data can be converted into a pore size distribution curve.

In this study, MIP measurements were performed with a Micrometrics PoroSizer® 9320 with a maximum intrusion pressure of 207 MPa. The specimens without any restraint were taken out from the sulfate solutions at certain time and were prepared for MIP. Freeze-drying method was adopted for conditioning the specimens before the MIP test. The contact angle (θ) and the surface tension (γ) used for calculations were 139° and 480 mN/m, respectively [92, 94]. For these pressures, the measured pore size was in the range from 0.007 μm to 400 μm .

2.3. RESULTS AND DISCUSSION

2.3.1. FREE EXPANSION

IT was observed that the free expansions in both weak and strong sulfate exposure conditions increased continuously during the immersion tests, as shown in Fig. 2.6. Free expansions were expectedly found to be much larger than the restrained expansions (Fig. 2.7). Free expansion in strong sulfate solution (30 g/L SO_4^{2-}) was remarkably larger than free expansion in weak sulfate solution (1.5 g/L SO_4^{2-}).

Based on the speed change of the increase in expansion (Fig. 2.6), it seems that the attack process for the freely expanding specimen immersed in strong sulfate solution (spring - 30 g/L) can be divided into three stages. During the first stage (from 0-day to 98-day immersion), the free expansion increased steadily. In the second stage (from 98-day to 350-day immersion), the free expansion tended to accelerate. In the third stage (from 350-day immersion), the fastest increase of the free expansion happened. The acceleration of free expansion in stage 2 may be caused by the distributed micro-cracks and then the localized cracks. After that, it was possible that more and more localized cracks began to coalesce in stage 3, which can lead to a rapid deterioration of the specimen. More discussion regarding the attack process is given in section 4.5, which considered all the experimental observations from chapter 2, 3 and 4. For the freely expanding specimen immersed in weak sulfate solution (spring - 1.5 g/L), it seems that the specimen still stayed in the first stage until 420-day immersion.

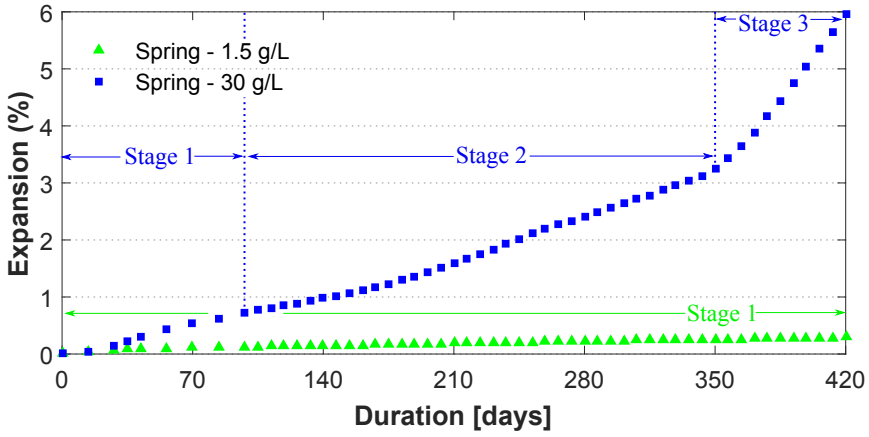


Figure 2.6: Free expansions of the cement paste pipes in weak and strong sulfate solutions

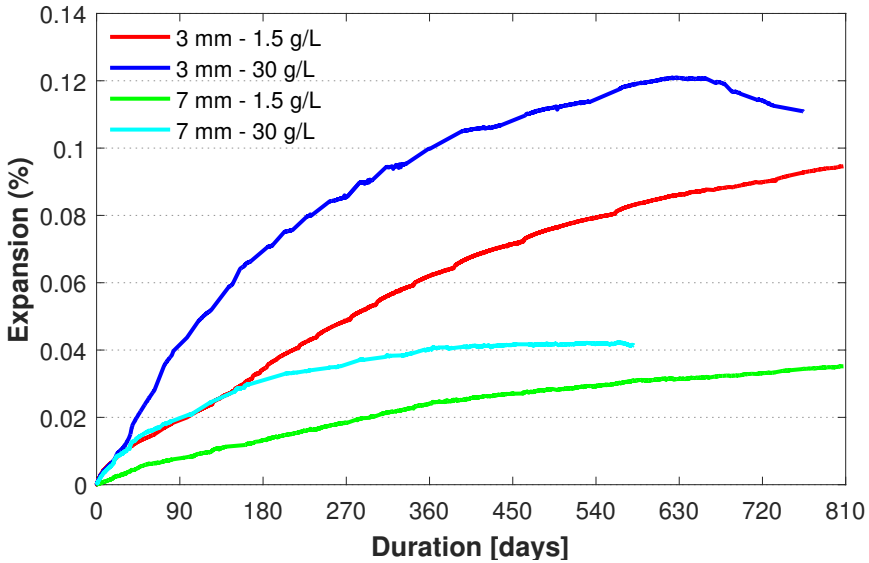


Figure 2.7: Restrained expansions of the cement paste pipes in weak and strong sulfate solutions

2.3.2. RESTRAINED EXPANSION AND GENERATED STRESS

For the restrained condition, it was also observed that the restrained expansions and the generated stresses in both weak and strong sulfate exposure conditions increased continuously during the initial immersion tests. In general, a stronger sulfate solution or a lower restraint condition resulted in a faster expansion. A stronger sulfate solution or a higher restraint condition led to a larger generated stress. Fig. 2.7 and Fig. 2.8 show the results of restrained expansions and generated stresses up to 807-day immersion in the two different sulfate solutions under low- and high-restraint conditions.

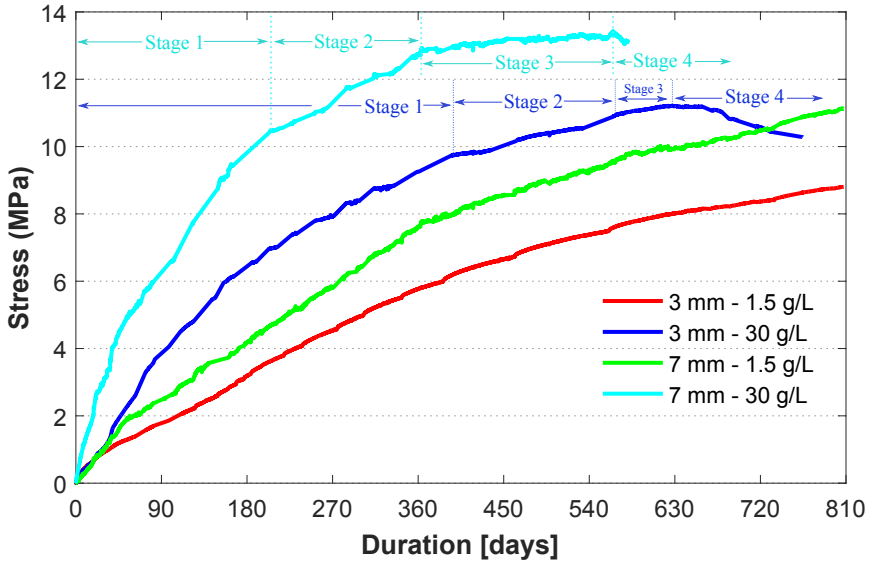


Figure 2.8: Generated stresses of the restrained cement paste pipes in weak and strong sulfate solutions

For the specimen immersed in strong sulfate solution under high-restraint condition (7 mm - 30 g/L), it was found that the generated stress increased fast until 205-day immersion. Then the increase of generated stress slowed down until 365-day immersion. From 365-day immersion to 565-day immersion, the increase of generated stress almost stopped with a rather small rise from 12.9 MPa to 13.4 MPa. The largest generated stress occurred at 565-day immersion and the generated stress started to decrease from there on. The largest generated stress was 13.4 MPa with the expansion of 0.042 %.

Based on the experimental observation above, for the specimen immersed in strong sulfate solution under high-restraint condition (7 mm - 30 g/L), four stages regarding the damage process are proposed as a hypothesis (Fig. 2.8). In the first stage (from 0-day to 205-day immersion), due to the continued penetration of external sulfate ions, the generated stress of the specimen increased steadily. In this stage, maybe only limited distributed micro-cracks were formed. In the second stage (from 205-day to 365-day immersion), the slowdown of generated stress increase may be caused by the formation of few localized cracks. In the third stage (from 365-day to 565-day immersion), the almost stop of generated stress increase may be due to the process of crack localization and for-

mation of large cracks. In the final stage, the specimen cannot carry more compressive stress at the restrained boundaries and can be damaged with large cracks connecting. The crack pattern of the specimen at the beginning of fourth stage is presented in Fig. 3.22a.

For the specimen immersed in strong sulfate solution under low-restraint condition (3 mm - 30 g/L), the four stages can also be found (Fig. 2.8), which is not as obvious as the specimen under high-restraint condition (7 mm - 30 g/L). The crack pattern of the specimen at the beginning of fourth stage is presented in Fig. 3.22b. The largest generated stress occurred at 628-day immersion and the generated stress started to decrease from there on. The largest generated stress was 11.2 MPa with the expansion of 0.121 %.

For the specimens immersed in weak sulfate solution (1.5 g/L), the generated stresses kept increasing up to 807-day exposure and tended to increase with the tests continuing. At 807-day immersion, the generated stress of specimen under low-restraint condition (3 mm - 1.5 g/L) was 8.8 MPa with the expansion of 0.095 %. The generated stress of specimen under high-restraint condition (7 mm - 1.5 g/L) was 11.1 MPa with the expansion of 0.035 %.

For the specimens under restrained conditions, the specimens tended to expand, however, they were restrained by the steel bars. Therefore, the steel bars were under tensile stress, while the specimens were under compressive stress. The value of the tensile stress is equal to the value of the compressive stress, which is defined as the generated stress in this study. Therefore, the internal expansive pressure caused by the external sulfate attack led to the restrained expansion and the generated stress. After 189-day immersion, the generated stresses of 10.1 MPa in strong sulfate solution and 4.4 MPa in weak sulfate solution under high-restraint condition were measured, which means the internal local expansive pressure in the cement paste was rather high. However, no visually noticeable cracks were observed for all the restrained specimens. This phenomenon is due to that the restrained specimens were in fact under compression. The whole specimen may be damaged due to tensile splitting in the final stage.

2.3.3. PORE SIZE DISTRIBUTION

The pore size distribution differential curve was derived from the pore size distribution cumulative intrusion curve and is essentially a plot of $dV/d\log D$ (V: Pore volume) against D (D: Pore diameter). The peaks in the curves represent the pore diameters corresponding to the higher rate of mercury intrusion per change in pressure, which are also known as the "critical pore diameters" [91]. The area under the curve represents the total volume within the specific range of pores. Fig. 2.9 shows the pore size distribution of the specimens before the exposure to sulfate solutions and after 21 days, 70 days, 105 days, 133 days and 189 days immersion. The samples used for MIP tests were the complete cross section of the specimens. Even though the wall thickness (2.5 mm) of the specimen is small, a gradient along the diffusion direction can still exist regarding the amount of pore filling, which means more pores can be filled for the surface part compared with the inner part at the initial exposure period. Therefore, the experimental results in this study can only reflect the tendency of pore filling. The amount of pore filling is an overall result of the complete cross section.

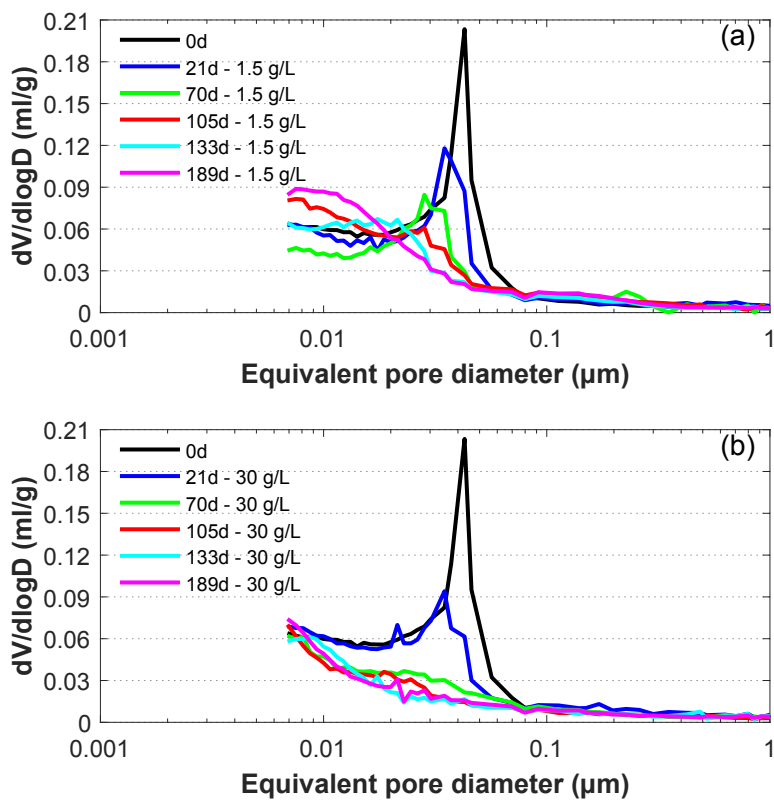


Figure 2.9: Pore size distribution differential curves after being exposed to (a) weak and (b) strong sulfate solutions of unrestrained specimens

In the weak sulfate solution, it was found that the peak kept moving to a smaller pore diameter as the duration of exposure increased. It is plausible to suggest that as the larger pores were continuously filled by the sulfate-bearing reaction products and meanwhile some smaller new pores or cracks were produced because of the expansive pressures on the walls of larger pores in the range of 10 nm to 70 nm, as shown in Fig. 2.9a.

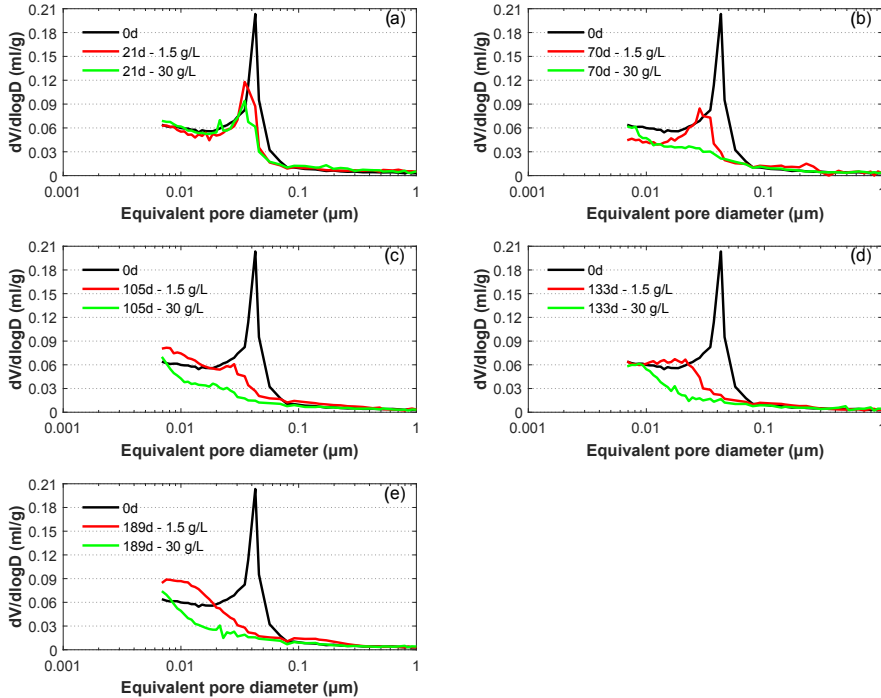


Figure 2.10: Pore size distribution differential curves for (a) 21-day, (b) 70-day, (c) 105-day, (d) 133-day and (e) 189-day immersion of unrestrained specimens

In the strong sulfate solution, it was also found that the pores with diameters between 10 nm and 70 nm were gradually filled during the immersion tests (Fig. 2.9b). The difference was that the filling of the nanopores (10 nm - 70 nm) in the strong sulfate solution was much faster than that in the weak sulfate solution, which can be seen through Fig. 2.10. The filling of the nanopores can produce significant local expansive pressure. High sulfate solution resulted in more filling of the nanopores compared with the weak sulfate solution when the immersion time was equal. This explained the observation of a faster expansion in strong sulfate solution. The observation of the nanopores filling also supported the crystallization pressure theory to explain the origin of the expansive pressure.

2.4. SUMMARY AND CONCLUSIONS

IN this chapter, an experimental study on the expansion behavior of cement paste pipes immersed in sodium sulfate solutions is presented. The wall thickness of the specimens was only 2.5 mm. The study considered two types of sulfate concentrations and three types of longitudinal restraints. Based on the experimental results and discussions, the following conclusions can be drawn:

- The free expansions in both weak (1.5 g/L SO_4^{2-}) and strong (30 g/L SO_4^{2-}) sulfate solutions increased continuously during the immersion tests. For the same exposure time, free expansion in strong sulfate solution was remarkably larger than that in weak sulfate solution. In addition, the free expansions were obviously much larger than the restrained expansions.
- The restrained expansions and the corresponding generated stresses in all the conditions kept on increasing during the sulfate exposure until the occurrence of specimen damage. In general, a stronger sulfate solution or a lower restraint condition resulted in an accelerated expansion. A stronger sulfate solution or a higher restraint condition led to a larger generated stress.
- For the specimen immersed in strong sulfate solution under high-restraint condition (7 mm - 30 g/L), the generated stress began to decrease from 565-day immersion. For the specimen immersed in strong sulfate solution under low-restraint condition (3 mm - 30 g/L), the generated stress started to decrease from 628-day immersion. The decrease of generated stress is due to that the specimen cannot carry more compressive stress at the two ends and tends to the damage process. Therefore, a higher restraint can result in an earlier damage.
- For the specimens immersed in strong sulfate solution (30 g/L), the largest generated stresses for high-restraint condition (7 mm - 30 g/L) and low-restraint condition (3 mm - 30 g/L) were 13.4 MPa and 11.2 MPa, respectively. For the specimens immersed in weak sulfate solution (1.5 g/L), the generated stresses kept on increasing up to 807-day exposure and tended to increase with the tests continuing. At 807-day immersion, the generated stresses of specimens under low-restraint condition (3 mm - 1.5 g/L) and high-restraint condition (7 mm - 1.5 g/L) were 8.8 MPa and 11.1 MPa, respectively. The measured generated stresses were caused by the internal expansive pressure. Therefore, both of strong and weak sulfate solutions can lead to a rather high expansive pressure in cement paste.
- According to the MIP measurements, the pores with diameters between 10 nm and 70 nm were continuously filled during the exposure to both of the sulfate concentrations, which supports the crystallization pressure theory to explain the origin of the expansive pressure when exposed to external sulfate ions. On the other hand, it should be noted that the samples used for MIP tests were the complete cross-section of the specimens. Even though the wall thickness (2.5 mm) of the specimen is small, a gradient along the diffusion direction can still exist regarding the amount of pore filling. Therefore, the experimental results from MIP measure-

ments can only reflect the tendency of pore filling. The amount of pore filling is an overall result of the complete cross-section.

- It was found that the filling of the nanopores (10 nm - 70 nm) in strong sulfate solution was much faster than that in weak sulfate solution, which explained the observation of a faster expansion in strong sulfate solution.

3

MICROANALYSIS OF CEMENT PASTE DEGRADATION CAUSED BY EXTERNAL SULFATE ATTACK

This chapter presents an experimental study on the degradation of cement paste exposed to sodium sulfate solutions. The sulfur ingress profiles of samples immersed in two types of sulfate concentrations were periodically analyzed. SEM - EDS microanalysis and image analysis were applied. In order to obtain non-destructive experimental results, X-ray computed tomography (CT) was used to acquire the three-dimensional crack patterns of the specimens immersed in strong sulfate solution under three types of restraints. The procedure of crack segmentation based on original microtomography slices was introduced.

Parts of this chapter have been published in Construction and Building Materials 410-422, (2018) [88].

3.1. INTRODUCTION

EXTERNAL sulfate ions can penetrate into the hardened concrete, and react with cement hydration products to form crystals [11, 38]. The crystal growth in the confined space leads to the local expansive pressure on the wall of the pore system. The ingress of external sulfate ions is a process, which occurs from the surface inwards. As a result, a dynamic gradient of local expansive pressure along the diffusion direction exists during the penetration process. The expansions and generated stresses of cement paste pipes immersed in sodium sulfate solutions were measured continuously and discussed in chapter 2, however, the gradient of expansive pressure was missing, which was responsible for the overall expansion. Theoretically, the dynamic expansive pressure gradient is related with the dynamic sulfur gradient. Therefore, in this chapter, the sulfur ingress profiles were periodically analyzed during the immersion tests exposed to two sulfate concentration levels.

In most cases, sample preparations for SEM may possibly lead to drying cracks in sample, which include drying in a vacuum environment, impregnation with epoxy resin, grinding and polishing. In addition, once the sample is prepared and tested, it cannot be put back to sulfate solutions for further investigations. As an alternative, X-ray computed tomography (CT) is an excellent technique since it can provide a non-destructive method to obtain three-dimensional microstructure information of cementitious materials. Therefore, the crack pattern and crack development of the specimens exposed to strong sulfate solution (30 g/L) up to 765-day immersion were studied by CT scanning as described in this chapter.

3.2. SEM-EDS MICROANALYSIS

3.2.1. MATERIALS AND METHODS

THE tested material was a standard grade OPC CEM I 42,5 N paste with a water/cement ratio of 0.40. Special moulds were fabricated to produce the cement paste pipes with a wall thickness of 2.5 mm (outer diameter 30 mm, inner diameter 25 mm), as described in section 2.2.1. Upon completion of the curing period, the cement paste pipes were polished at both ends before being immersed in sodium sulfate solutions with the SO_4^{2-} ion concentrations of 1.5 g/L and 30 g/L, respectively. The size of the specimens is shown in Fig. 3.1. The immersion tests were carried out in a room with a constant temperature at 20 ± 1 °C. The sulfate solutions were renewed every two weeks until 238-day immersion and from there on every four weeks to keep the strength of the solution stable.

The specimens were taken out of sulfate solutions after a predefined exposure period and cut at a length of 25 mm, as shown in Fig. 3.1. Then the cut surface was prepared for SEM-EDS microanalysis, which included drying, impregnation with low-viscosity epoxy resin, grinding, polishing and coating with carbon.

Oven drying at 36 °C was used for the samples at 21-day, 70-day, 105-day and 133-day immersion. Solvent exchange with isopropanol and then drying under vacuum were used for samples at 189-day immersion and the reference sample just after 90-day curing. It was found that the second drying method performed better for avoiding drying cracks than the first drying method. Therefore, the second drying method is suggested for future researches. In this study, the crack pattern was discussed based on the anal-

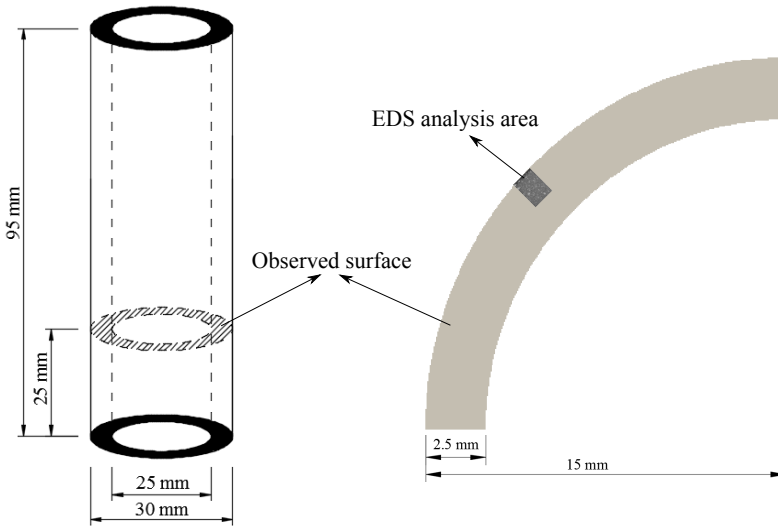


Figure 3.1: Specimen used in the experiments

yses of elemental mappings. Therefore, the drying cracks have no effect on the analysis result.

After drying, the samples were put in a plastic mould and then placed in a vacuum chamber at 30 mbar for half an hour. Afterwards, the resin was supplied from a cup outside the vacuum chamber into the plastic mould through a plastic tube. Then the upper face of the samples was covered with resin. After about 10 minutes, air was introduced into the vacuum chamber gradually to push the resin further into the pore system of the samples. The impregnated samples were cured at atmospheric pressure at room temperature for 24 hours [92, 95].

After impregnation with epoxy resin, the samples were carefully polished by hand, which included grinding with grade # 320, # 500, # 800, # 1200, and # 4000 grinding sandpaper (Silicon Carbide) and following by $6\ \mu\text{m}$, $3\ \mu\text{m}$, $1\ \mu\text{m}$, and $0.25\ \mu\text{m}$ diamond paste polishing with a lapping table. After each grinding and polishing step, the sample surfaces were cleaned by immersing them in an ultrasonic bath with ethanol for 10s. Finally, the polished surfaces were coated with carbon in a Leica EM CED030 carbon evaporator at a thickness of about 10 nm, in order to provide a conductive surface and to prevent charging [96, 97]. Fig. 3.2 shows an example of the sample ready for the SEM-EDS microanalysis.

The prepared samples were examined by scanning electron microscopy (SEM) using backscattered electron detector (BSE) for imaging and energy dispersive X-ray spectroscopy (EDS) for elemental distribution maps. A Philips XL30 ESEM equipped with an EDAX energy-dispersive spectrometer was used for the microanalysis. All SEM-EDS microanalyses were performed at an accelerating voltage of 15 kV and in the hi-vac chamber condition. The BSE micrographs and EDS elemental distribution maps were obtained at low magnification level ($\times 100$) which covers an area of $1264 \times 948\ \mu\text{m}^2$ with



Figure 3.2: Sample for SEM-EDS microanalysis (polished section coated with carbon)

a resolution of 256×192 pixels. As a result, the length of region-of-interest (ROI) of all the obtained images was $1264 \mu\text{m}$, which was along the diffusion direction. The size of one pixel was about $5 \times 5 \mu\text{m}^2$ representing an area approximately equivalent to a single analysis spot at 15 kV. The EDS elemental distribution maps were acquired by Thermo Scientific Noran 7 solid state EDS system in standardless analysis mode, which relies on the internal standards of the microanalysis software. The obtained results were normalized to 100 % without taking chemically bound water into account. The wall thickness of the specimens was 2.5 mm and both sides of the wall surface were exposed to sulfate solutions. Therefore, the length of ROI was considered to be sufficient for the analysis, which is larger than the half wall thickness of specimens.

3.2.2. IMAGE ANALYSIS

The acquired EDS elemental distribution map is a scaled image in which the characteristic X-rays for each element of interest at each analysis point (pixel in elemental distribution map) are counted and uniformly scaled to be the gray level from 0 to 255 [98–101]. The intensity of the elemental map is proportional to the element concentration, which can reflect the relative relation of element concentration at each pixel. However, the real element concentration at each pixel cannot be obtained directly because of the scaled intensity value. Meanwhile, the highest normalized concentration of each element was recorded in the EDS software, which is related to the gray value of 255 in the scaled elemental map and can be used for the image rescaling. Therefore, in this chapter, a MATLAB code for image analysis was developed to get the normalized weight percentage of sulfur at each pixel and the sulfur distribution along the diffusion direction, which consists of two steps, rescaling and calculation.

In rescaling step, based on the recorded highest normalized sulfur weight percentage of each mapping from the software which is related to the gray value of 255 in the scaled output mapping, the gray value in each pixel was rescaled linearly to a number which stands for the normalized weight percentage of sulfur. After this step, the normalized

sulfur weight percentage at each pixel was obtained, as shown in Fig. 3.8 and Fig. 3.9. In calculation step, in order to get rid of the influence from the empty pores, only the pixels with sulfur weight percentage above 0 % were counted. Then the average of the counted pixels along each column (parallel to the exposed surface) was calculated, which means one number was obtained for each column. The obtained number represents the average sulfur weight percentage at the corresponding penetration depth. After this step, the sulfur distribution along the penetration depth was obtained based on the sulfur mapping image. For each sulfur distribution curve in this chapter, the result is an average value obtained from two different areas of the same sample. The sulfur distributions at the two different areas were similar for each case.

3.3. MICRO-COMPUTED TOMOGRAPHY TECHNIQUE

3.3.1. MATERIALS AND METHODS

THE internal structure of the cement paste pipes immersed in 30 g/L SO_4^{2-} after different exposure period was monitored by using three-dimensional (3D) X-ray computed tomography (CT), as listed in Table 3.1. While mostly applied in healthcare industry, CT scanning is also increasingly used in the measurements of cementitious materials, because of its high resolution, non-destructive characteristic and clear 3D visualization. Various researches with the application of CT scanning in cementitious materials can be found in the literature, such as pore structure and tortuosity analysis [102, 103], cement microstructure investigation [104, 105] and corrosion induced damage [106, 107]. In this chapter, the crack pattern and crack development of specimens exposed to sodium sulfate solutions were studied.

Table 3.1: The specimen information of the performed scans, all specimens were immersed in 30 g/L SO_4^{2-} .

Scan number	Specimen number	Type of restraint	Immersion duration (days)	Spatial resolution (μm)
1	Specimen 1	non-restraint	189	16.7
2	Specimen 2	non-restraint	294	20
3	Specimen 2	non-restraint	343	20
4	Specimen 2	non-restraint	420	23.6
5	Specimen 2	non-restraint	469	23.6
6	Specimen 3	high-restraint	581	30
7	Specimen 4	low-restraint	765	32.2

The X-ray CT technique is based on the mapping of the linear attenuation coefficient of X-rays passing through the investigated specimen. The attenuation depends on the composition and density of the specimen [108]. Multiple X-ray images of a specimen are taken at different angles. Using a reconstruction algorithm, these X-ray images are reconstructed to produce a three-dimensional digital image where each voxel stands for the X-ray absorption at that point [109]. Because of the relationship between X-ray absorption and material density, the 3D internal structure can be inferred. The resulting

3D images are typically displayed as a series of 2D slices [110].

In this chapter, four specimens immersed in 30 g/L SO_4^{2-} were scanned and discussed. Specimen 1 and specimen 2 were under same situation, which were unrestrained specimens. Specimen 1 was used for other purposes after checking by CT scanning, therefore specimen 2 was employed for the following scanning. After 294-day immersion, one whole cement paste pipe immersed in strong sulfate solution was taken out and cut. The part with the height of around 39 mm was chosen as specimen 2. Specimen 2 was examined by CT scanning in total four times at different exposure time and was put back to strong sulfate solution immediately after each scan. After 581-day immersion, the specimen (specimen 3) immersed in strong sulfate solution under high-restraint condition (7 mm - 30 g/L) was disassembled from the setup and scanned. After 765-day immersion, the specimen (specimen 4) immersed in strong sulfate solution under low-restraint condition (3 mm - 30 g/L) was also disassembled from the setup and scanned.

For each scan, the specimen was immersed in a plastic bottle filled with deionized water, in order to make sure no drying damage happened to the specimen during the CT scanning. Then the specimen surrounding with deionized water was scanned, as shown in Fig. 3.3. Phoenix Nanotom X-ray system was used for data acquisition. During each scan, 1 440 tomographic images with an exposure time of 4 s were taken over a complete 360° rotation. Achieved voxel size is listed in Table 3.1. The 3D tomographic reconstruction which can be represented as a series of 2D slices (Fig. 3.4a) was carried out with Phoenix Datas|x software.

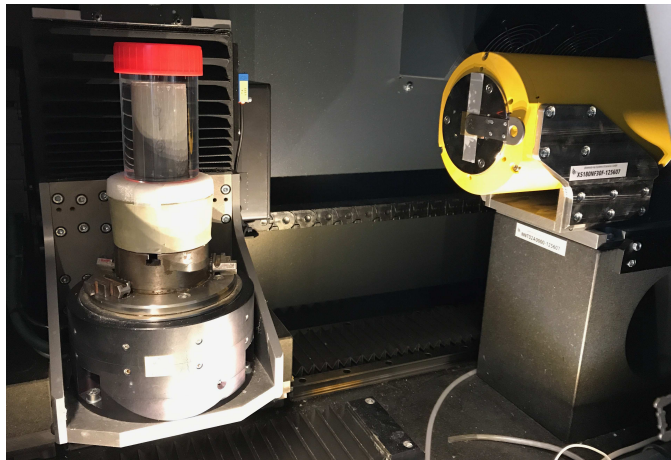


Figure 3.3: Setup of CT scanning (specimens were surrounded with deionized water)

3.3.2. IMAGE ANALYSIS

As presented in Fig. 3.4a, the original microtomography slice can show the crack clearly in a 2D view, which is a gray-scale digital image. Based on the analysis of histogram, one threshold value was determined for phase segmentation to separate crack from cement

paste. The resulting binary image is shown in Fig. 3.4b. This research focused on the crack pattern, therefore the cement paste which includes outer hydration products, inner hydration products and anhydrous cement is segmented as one phase. This phase displays as white in Fig. 3.4b. As shown in Fig. 3.4b, the crack pattern can be presented slice by slice in a 2D view, however, a whole 3D view of crack pattern is impossible since both of the crack part and background display as black. In this case, for a 3D construction of binary images presented in Fig. 3.4b, the internal cracks of the specimen cannot be seen and only the cracks on the surface are visible, as shown in Fig. 3.5a. Therefore, with the purpose of only showing the cracks, the crack part needs to be separated from the background, which can be realized by creating a reference image.

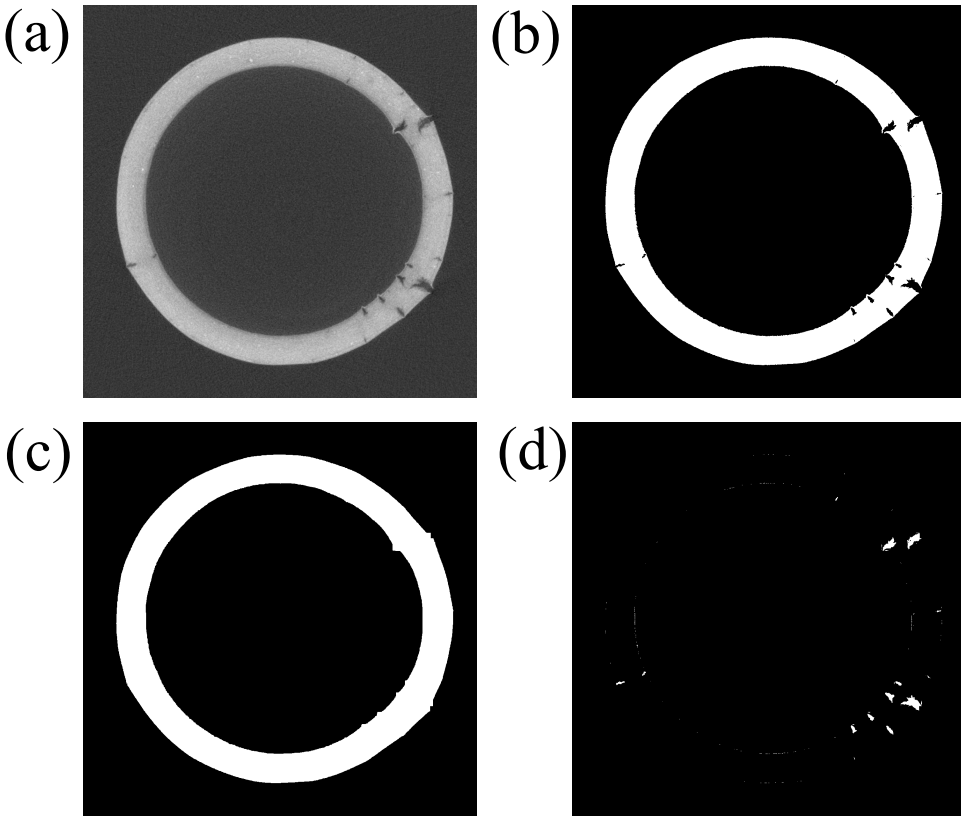


Figure 3.4: Segmentation procedure of cracks. (a) Original microtomography slice from the CT scanning (one image from Fig. 3.20 a). (b) Image segmentation of (a). (c) Reference image based on (b). (d) Segmented cracks based on (b) and (c).

The purpose of creating a reference image is to create one image which can fill the cracks in Fig. 3.4b. With the aid of ImageJ software, Fig. 3.4b was firstly dilated 15 times, which filled the cracks and resulting in a larger circle than the origin. After that, the same times (15 times) of erosion was applied on the dilated image to make the size of the circle back to the origin, which resulted in the needed reference image as shown in Fig. 3.4c.

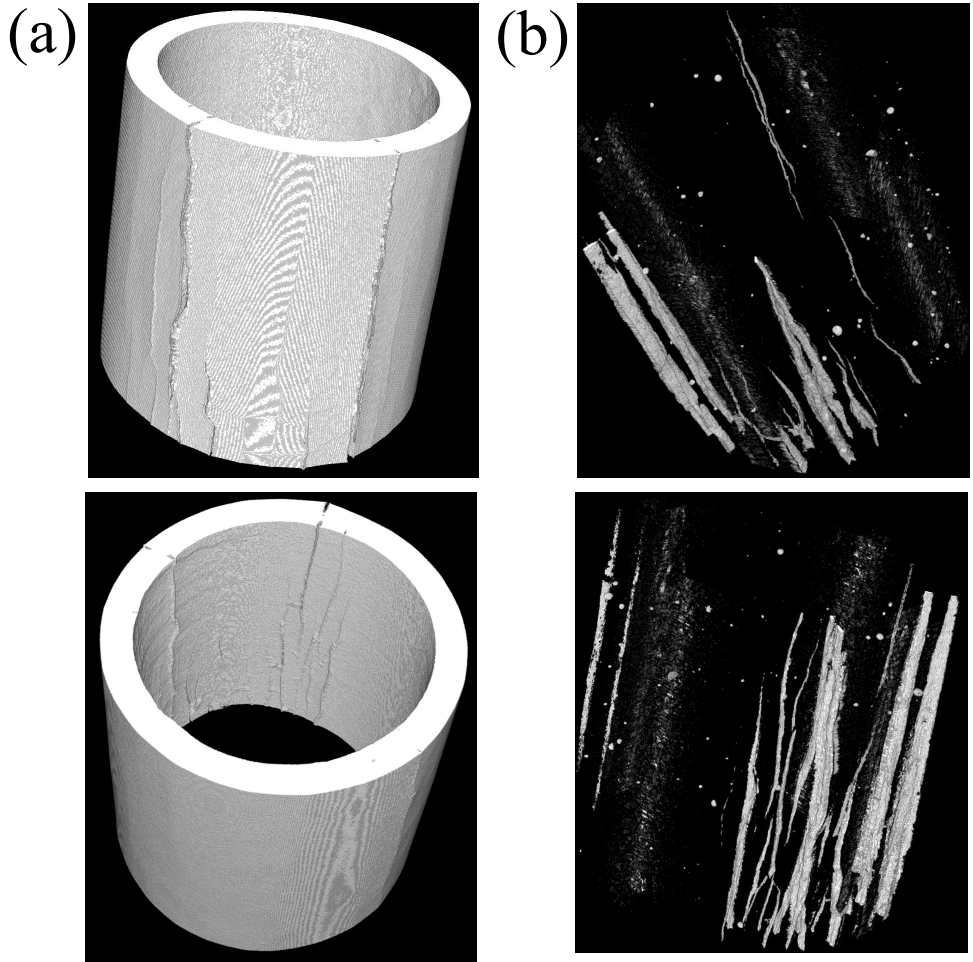


Figure 3.5: 3D construction of images based on (a) binary slices from Fig. 3.4 b and (b) segmented cracks from Fig. 3.4 d.

Finally, the segmented cracks (Fig. 3.4d) were obtained by subtracting Fig. 3.4b from Fig. 3.4c. Based on Fig. 3.4d, a 3D view of crack pattern was constructed, as presented in Fig. 3.5b. The whole procedure was accomplished by a MATLAB code combined with ImageJ software.

3.4. RESULTS AND DISCUSSION

3.4.1. SULFUR DISTRIBUTION

THE combined images of BSE micrographs and original sulfur mappings in weight percentage for the samples tested up to 189-day immersion are shown in Fig. 3.6 and Fig. 3.7, where the red color represents sulfur (one example is illustrated for each immersion time). The left edge of the images represents the surface of the sample exposed to the sulfate solutions. Therefore the external sulfate ions diffused from left to right. The width of each image is a bit larger than the half wall thickness of specimens. The rescaled sulfur mappings in weight percentages are shown in Fig. 3.8 and Fig. 3.9, which were used for the calculations of sulfur distribution curves in Fig. 3.10 and Fig. 3.11.

It was observed from Fig. 3.6 and Fig. 3.7 that sulfur accumulated in the hydrated matrix, which indicated the location of the newly formed sulfur-containing phases. It can be understood as that the external sulfate ions diffused into the pore network of the hydration products which is a mixture of several phases (eg: C-S-H, calcium hydroxide and monosulfate). When the supersaturation occurs, ettringite or gypsum forms inside the pores or cracks. When the crystal formation is suppressed by the confined pore wall, the expansive pressure on the pore wall is generated while the crystal is under compressive stress. The smaller the pore is, the higher the degree of supersaturation that is required for crystal formation. That means the larger the expansive pressure is produced to maintain the equilibrium. Especially in nanopores, significantly large expansive pressure may develop to damage the specimens.

Fig. 3.10a and Fig. 3.10b show the sulfur distribution inside the unrestrained specimens after 0-day, 21-day, 70-day, 105-day, 133-day and 189-day immersion in weak and strong sulfate solution, respectively. The differences caused by different sulfate solutions at the same immersion days are shown in Fig. 3.11. The depth presented in the curve stands for the distance from the exposed surface. The sulfur in the curve stands for the average normalized weight percentage of sulfur at a certain depth. The result of 0-day represents the specimen just after 90 days of curing in saturated limewater.

As shown in Fig. 3.10a, in the weak sulfate solution, the sulfur ingress profile had a noticeable gradient along the penetration depth at 21-day immersion. Three zones can be seen from the surface to the inside of the samples, which were a leaching zone, an attack zone and a pristine zone. The pristine zone stands for the area that is practically free of external sulfate ions. The pristine zone cannot be found at 70-day immersion, which can be understood as the external sulfate ions reached the half wall thickness of the sample within 70 days, considering that both sides of the wall surface were exposed to sulfate solutions. After 21-day immersion, the sulfur content of the area near the surface was increased slower compared with the area in the bulk. With the increased immersion time, the sulfur gradient along the penetration depth became smaller. The almost uni-

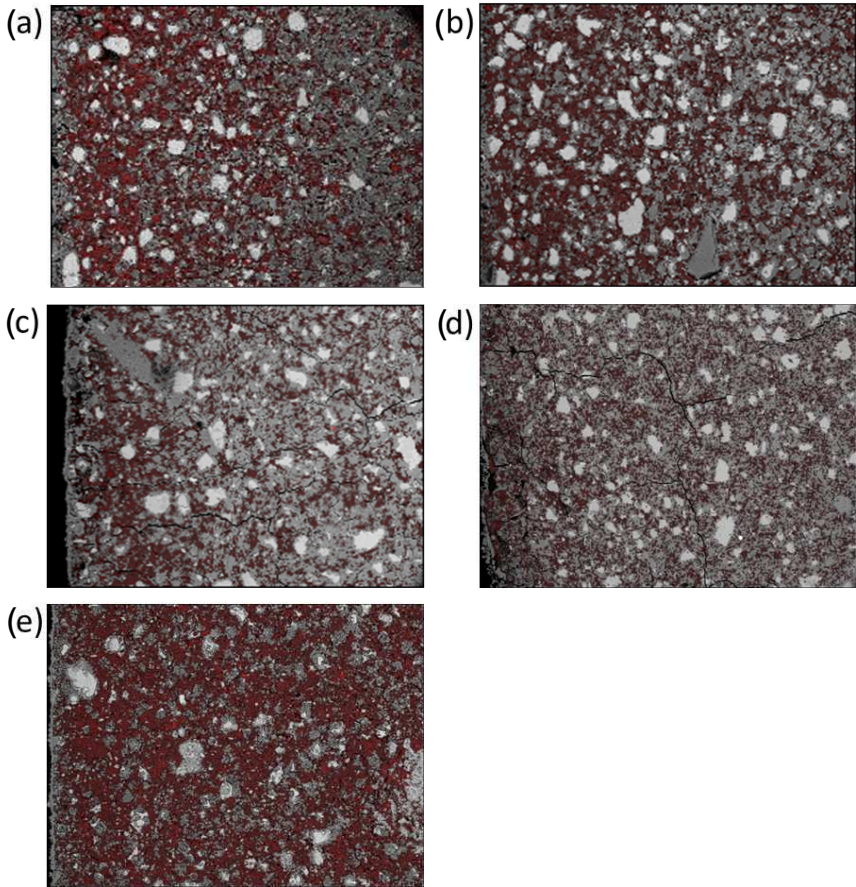


Figure 3.6: Combined BSE and original sulfur mapping images for (a) 21-day, (b) 70-day, (c) 105-day, (d) 133-day and (e) 189-day immersion in 1.5 g/L SO_4^{2-} of unrestrained specimens. Left edge of each image was the exposed surface. The field of view of each micrograph is $1264 \times 948 \mu\text{m}^2$

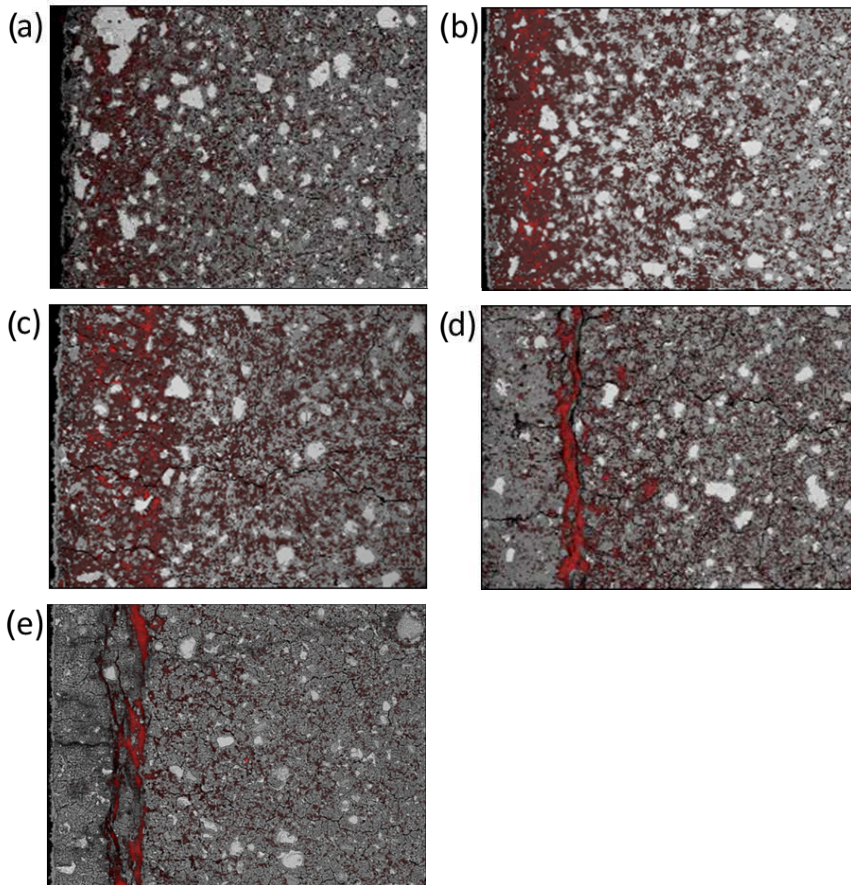


Figure 3.7: Combined BSE and original sulfur mapping images for (a) 21-day, (b) 70-day, (c) 105-day, (d) 133-day and (e) 189-day immersion in 30 g/L SO_4^{2-} of unrestrained specimens. Left edge of each image was the exposed surface. The field of view of each micrograph is $1264 \times 948 \mu\text{m}^2$

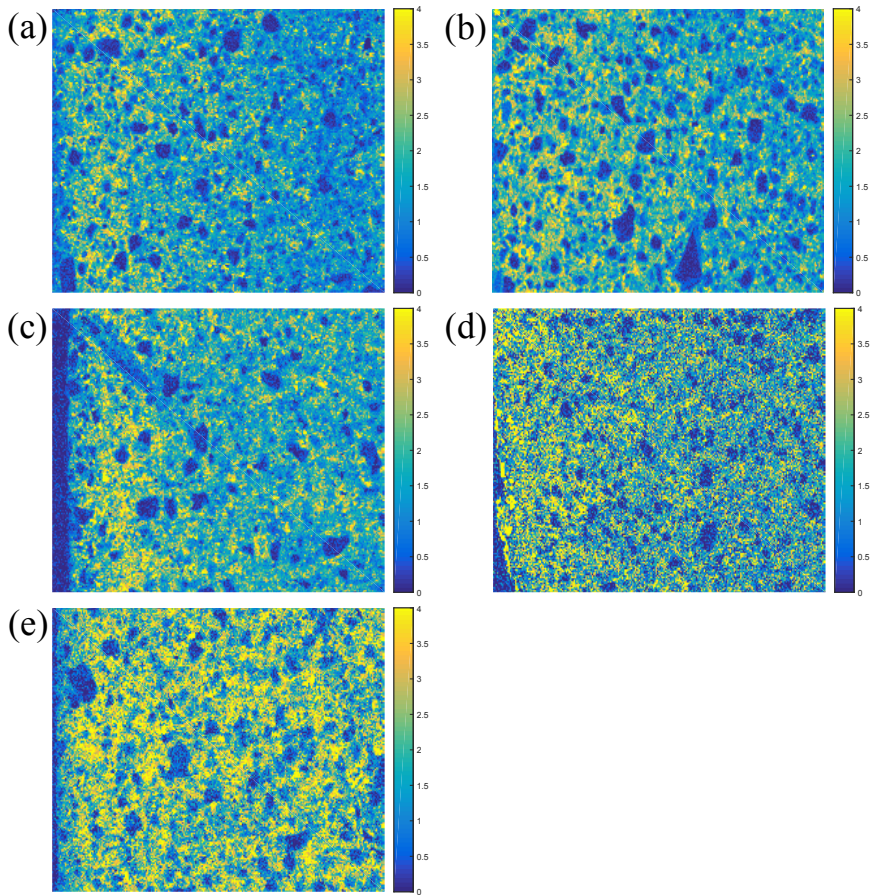


Figure 3.8: Rescaled sulfur mapping images in weight percentage (wt. %) for (a) 21-day, (b) 70-day, (c) 105-day, (d) 133-day and (e) 189-day immersion in 1.5 g/L SO_4^{2-} of unrestrained specimens. Left edge of each image was the exposed surface

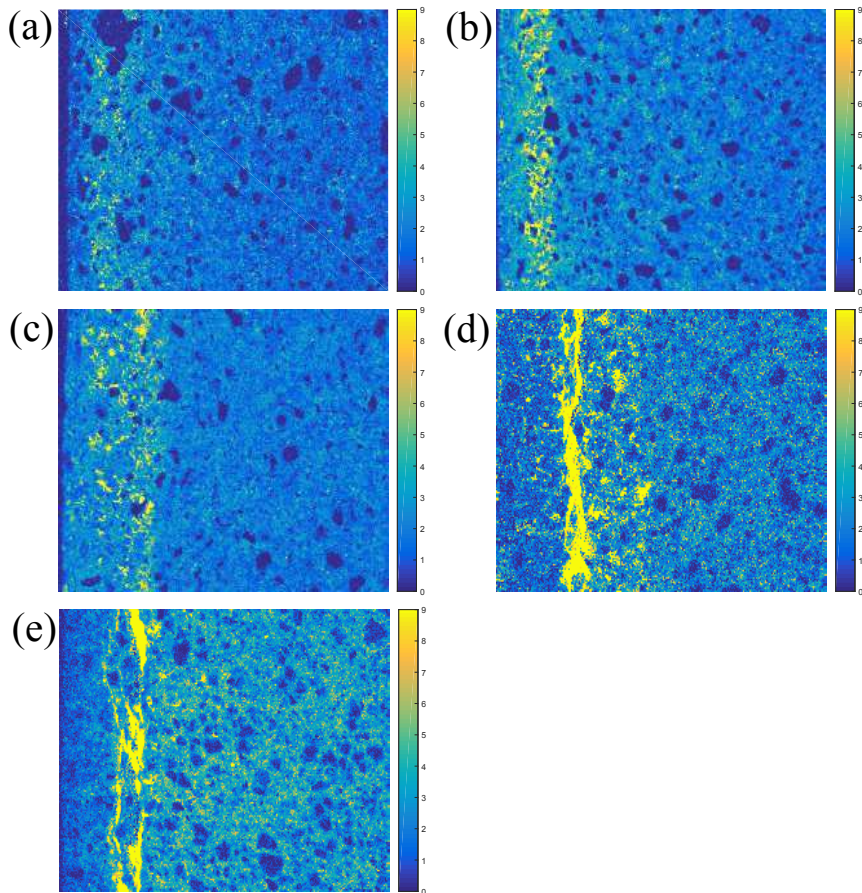


Figure 3.9: Rescaled sulfur mapping images in weight percentage (wt. %) for (a) 21-day, (b) 70-day, (c) 105-day, (d) 133-day and (e) 189-day immersion in 30 g/L SO_4^{2-} of unrestrained specimens. Left edge of each image was the exposed surface

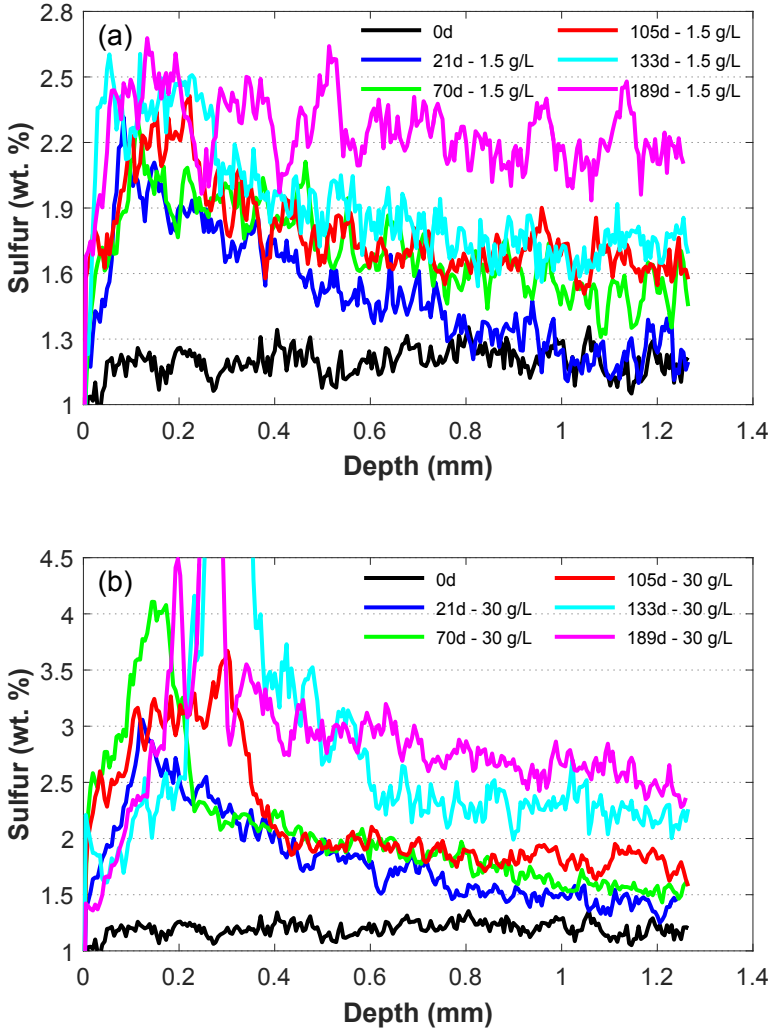


Figure 3.10: Sulfur distributions along diffusion direction after being exposed to (a) weak and (b) strong sulfate solutions of unrestrained specimens

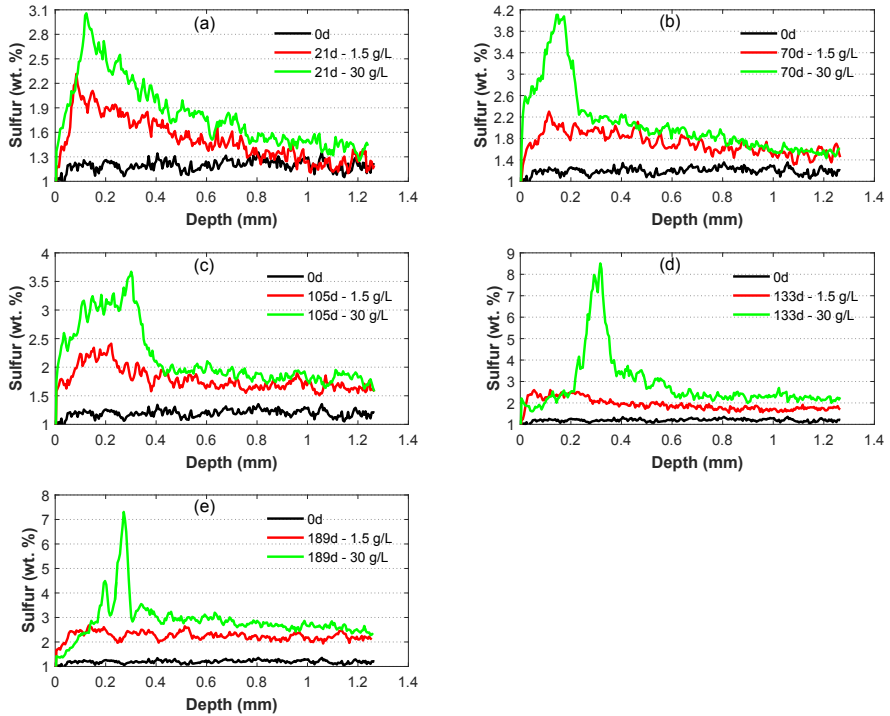


Figure 3.11: Sulfur distributions along diffusion direction for (a) 21-day, (b) 70-day, (c) 105-day, (d) 133-day and (e) 189-day immersion of unrestrained specimens

form sulfur distribution was found at 189-day immersion. A more uniform sulfur distribution with a higher average sulfur content was expected with extended immersion time. The sulfur content represents the amount of original and newly formed sulfur-containing phases at each location. In weak sulfate solution, the main product was suggested to be ettringite, which was limited by the abundance of aluminum-containing phases as well as available sulfate ion through external sulfate penetration. The amount of aluminum-containing phases was constant at each depth. Therefore, the sulfur content at each depth of the sample tended to increase to a limit value, considering the limit of aluminum-containing phases. Furthermore, the aluminum-containing phases were uniformly distributed inside the existing cementitious materials, which can finally lead to a uniform sulfur distribution if no cracks happened.

During the immersion tests, there was always a dynamic sulfur gradient along the diffusion direction because of the penetration of external sulfate ions, which caused an internal expansive pressure gradient along the wall thickness of the specimens. Before the cracks occurred and gypsum precipitated inside the generated cracks, it can be simply assumed that additional sulfur relates to higher local expansive pressure. In the initial stage, the attacked area tended to expand while the non-attacked area wanted to keep the original shape. Thus, the attacked area was restrained by the non-attacked area. In this situation, the attacked area was under compressive stress, and the non-attacked area was under tensile stress. The situation was similar for the sulfur-rich area and the area lower in sulfur. The sulfur-rich area expanded more than the area lower in sulfur and therefore was restrained by it. Therefore, for the zone at the boundary between sulfur-rich area and the area lower in sulfur, the tensile stress was probably very high, as a result of the gradient of the sulfur distribution. Note that the stresses acted in all directions. Also ring-compressive stresses developed at the outer and inner ring of the specimen. Between the layers, a radial tensile stress would occur. The micro-cracks started growing in the area where tensile stress exceeded tensile strength of the material, and in a later stage microcracks localized in main cracks.

For the specimens immersed in strong sulfate solution, a layer of sulfur-rich phases was found at 133-day immersion, as shown in Fig. 3.7d. The layer was subparallel to the exposed surface with the distance from the exposed surface of around 250 μm . Calcium was also rich in the layer while the content of other elements were low, which suggested mainly gypsum precipitation. As shown in Fig. 3.10b, it was found that the sulfur content at a depth of between 30 μm and 250 μm kept on being increased until 70-day immersion. The sulfur gradient was rather large at 70-day immersion, and a clear boundary was found at the depth of around 250 μm . The area with the higher sulfur content tended to expand more than the area with lower sulfur content, which caused tensile stress in the lower sulfur content area. The highest tensile stress may happen at the boundary between area under compressive stress and area under tensile stress. The large sulfur gradient at 70-day immersion may result in a very high pressure gradient, which can probably lead to micro-crack formation at the depth of around 250 μm . These micro-cracks were much larger compared with the pore network of the surrounding undamaged cement paste, therefore the crystal precipitation was promoted. After that, the distributed micro-cracks kept on being developed to form continuous micro-cracks because of the pressure gradient. Finally, a localized crack occurred, as shown in Fig. 3.7d and Fig. 3.7e.

It can be found through Fig. 3.10b that the sulfur content at the depth of around 250 μm increased dramatically at 105-day immersion and kept on being increased, which can be understood from the fact that many distributed micro-cracks were formed at the depth of around 250 μm after 70-day immersion and gypsum kept on being precipitated in the formed micro-cracks. With the development of the cracks, more and more ions diffused into the cracks, which resulted in more and more gypsum precipitation. Finally, due to the produced crack pattern, a layer or several layers of gypsum can be found along the cracks. Moreover, the smaller sulfate-bearing crystals tended to dissolve and transfer their ions to a larger crystal in an adjacent pore [54, 55, 111], which explained the decrease of sulfur content at depth between 30 μm and 250 μm after 70-day immersion.

It can be concluded through Fig. 3.11 that strong sulfate solution resulted in high sulfur content along the diffusion direction, when the immersion time was same as in the weak sulfate solution. In the initial stage, the difference of sulfur distribution caused by the solution concentration is dominant by diffusion process and formation rates of sulfur-containing phases. It can be simply assumed that more sulfur relates to higher local expansive pressure. Then the micro-cracks happened in the strong sulfate solution, which was caused by the high local expansive pressure and great pressure gradient along the depth. After that, the gypsum began to precipitate in the localized micro-crack zone which led to a rather high sulfur content appearing at certain depth in the strong sulfate solution. This process indicates that the specimens under external sulfate attack is damaged layer by layer. The sulfur distribution curves in this chapter are important for the simulation work in the following chapters. A gradient of local expansive pressure along the depth has to be assumed based on the sulfur distribution at different immersion periods, which is an important simulation input. The measured sulfur distributions were from the unrestrained specimens. For the specimens under restrained conditions, considering the compressive stress acted at the two ends, the diffusion speed of external sulfate ions may probably be slower than that under free condition before connected micro-cracks occur.

3.4.2. CRACK PATTERN

As discussed in section 2.3, the specimens immersed in strong sulfate solution under three types of restraint were damaged at different exposure time. The noticeable damage occurred before 735-day immersion (Fig. 3.12b, c, d). On the other hand, even though the generated stresses of the specimens had reached 8.8 MPa for low-restraint condition and 11.1 MPa for high-restraint condition, no visually noticeable cracks were observed on the specimens immersed in weak sulfate solution up to 807-day immersion (Fig. 3.12a). This phenomenon can be understood as the pressure gradient along the wall thickness for the specimens immersed in weak sulfate solution was not large enough to cause the obvious cracks up to 807-day immersion. In this chapter, the crack pattern and crack development of the specimens immersed in strong sulfate solution were discussed.

For the unrestrained specimen immersed in strong sulfate solution, two layers of sulfur-rich phases were observed under SEM at 189-day immersion (Fig. 3.7e). In order to get a non-destructive view of the crack pattern at the same exposure time, one unrestrained specimen (specimen 1) was checked by CT scanning after 189-day immer-

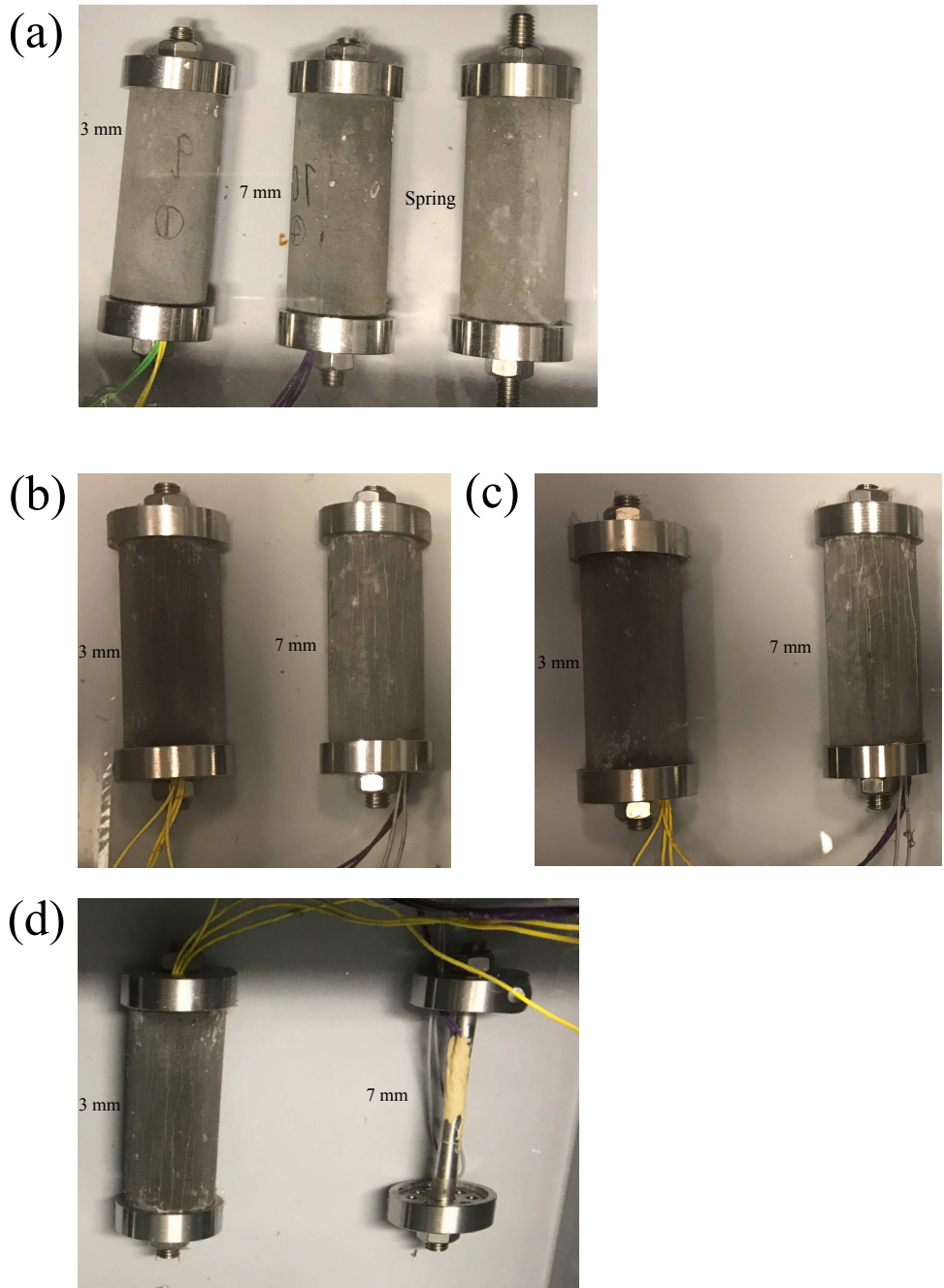


Figure 3.12: Specimens immersed in sodium sulfate solutions. (a) 807-day immersion in 1.5 g/L SO_4^{2-} , (b) 435-day immersion in 30 g/L SO_4^{2-} , (c) 581-day immersion in 30 g/L SO_4^{2-} and (d) 735-day immersion in 30 g/L SO_4^{2-} .

sion in strong sulfate solution. However, cracks were not detected, as shown in Fig. 3.13 and Fig. 3.14. Only gray value differences across the wall of the specimen were found, as presented in Fig. 3.15. The lower gray value on the surface part suggested more porosity or cracks on the surface part. Therefore, it was most likely due to the limited resolution achieved by the CT scanning ($16.7 \mu\text{m} / \text{voxel}$) compared to SEM ($5 \mu\text{m} / \text{pixel}$), which led to that the observed cracks under SEM were not detected under CT scanning.

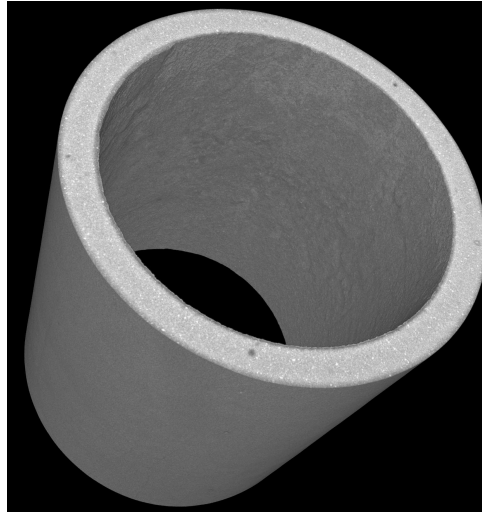


Figure 3.13: 3D renderings of unrestrained specimen (specimen 1) by CT scanning after 189-day immersion in 30 g/L SO_4^{2-} .

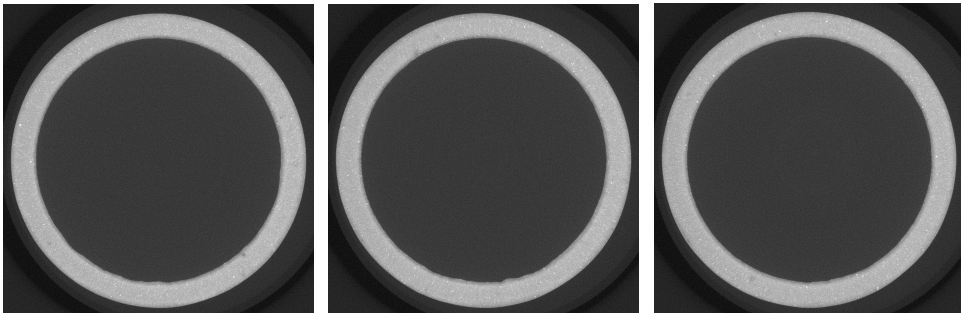


Figure 3.14: Reconstructed microtomography slices (3 random cross section) of unrestrained specimen (specimen 1) after 189-day immersion in 30 g/L SO_4^{2-} .

After 294-day immersion, visually noticeable cracks were observed for the unrestrained specimens immersed in strong sulfate solution, as shown in Fig. 3.16a. Then the crack pattern of the specimen (specimen 2) was studied by CT scanning. After that, the specimen (specimen 2) was also checked after 343-day (Fig. 3.16b), 420-day (Fig. 3.16c) and 469-day (Fig. 3.16d) immersion. The three dimensional renderings with two views in

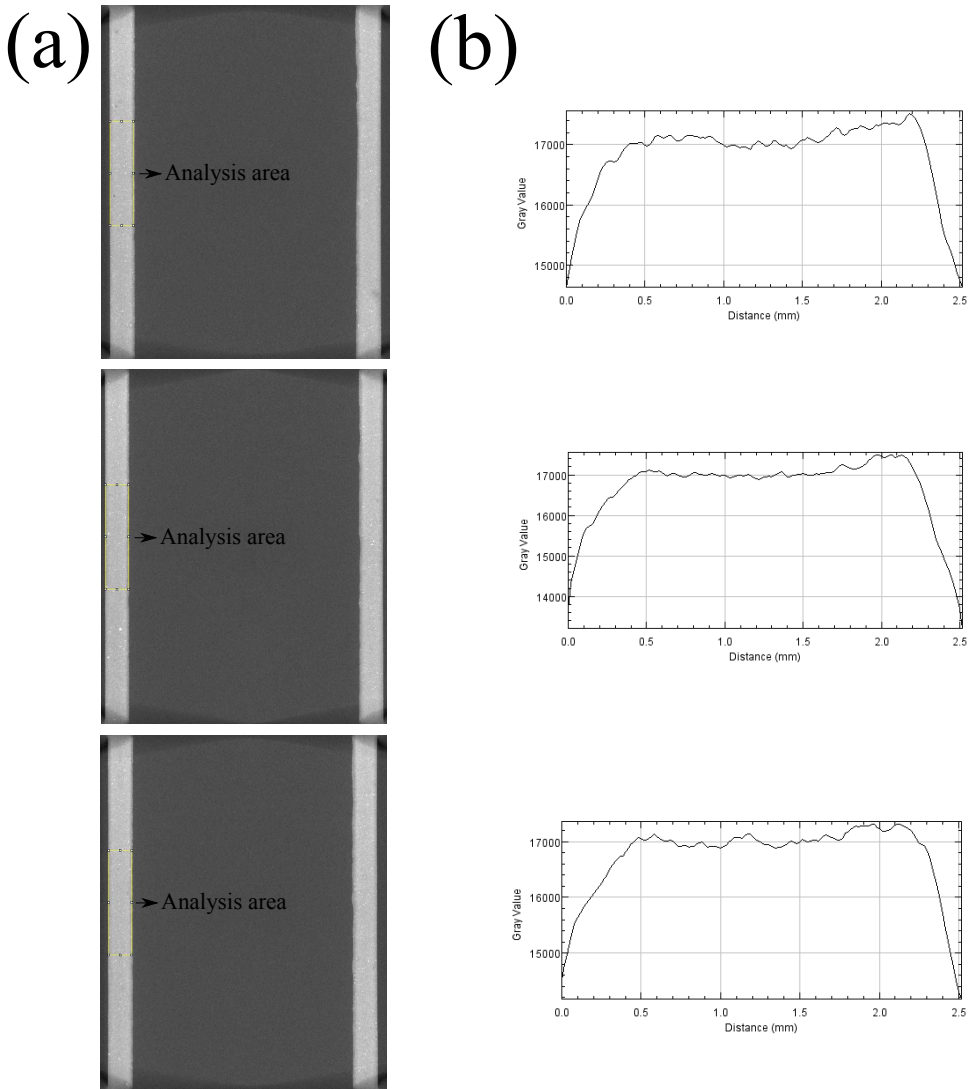


Figure 3.15: Reconstructed microtomography slices of unrestrained specimen (specimen 1) after 189-day immersion in 30 g/L SO_4^{2-} . (a) 3 random longitudinal section and (b) the corresponding distribution of gray value along thickness direction (the area covered by the yellow frame was analyzed).

each situation are shown in Fig. 3.17.

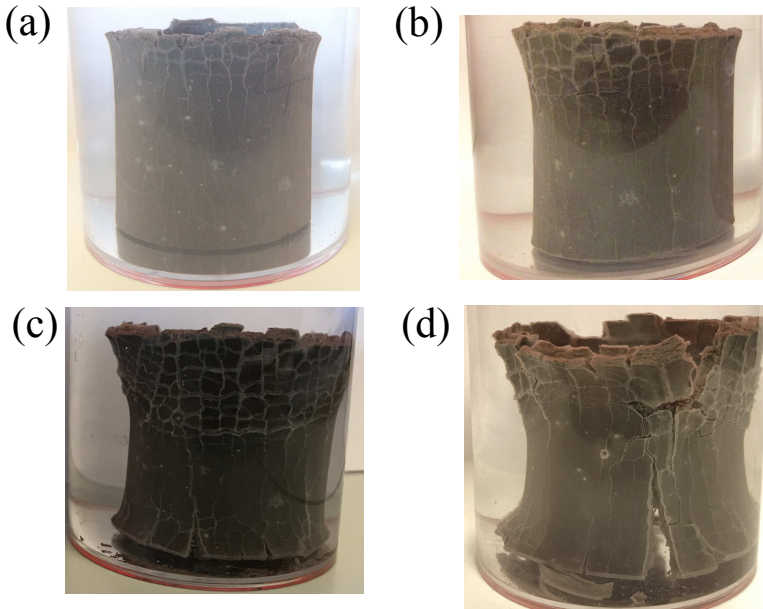


Figure 3.16: Unrestrained specimen (specimen 2) after (a) 294-day, (b) 343-day, (c) 420-day and (d) 469-day immersion in 30 g/L SO_4^{2-} .

For the unrestrained specimen (specimen 2) after 294-day immersion in strong sulfate solution, five reconstructed microtomography slices were chosen randomly from top to bottom of the specimen along the longitudinal direction, which were illustrated in Fig. 3.18a also from top to bottom. After that, for the 343-day immersion and 420-day immersion, the microtomography slices with similar location as 294-day immersion were also chosen and shown in Fig. 3.18b and Fig. 3.18c, respectively. The crack propagation can be seen in Fig. 3.18 along the horizontal direction, which represents the crack development at different exposure time.

As discussed in section 2.3.1, the attack process can be divided into three stages for the freely expanding specimen immersed in strong sulfate solution. The free expansion increased steadily in the first stage (from 0-day to 98-day immersion) and tended to increase faster in the second stage (from 98-day to 350-day immersion). After 350-day immersion, the speed of the expansion increased again, which suggested a rapid damage of the specimen, as shown in Fig. 2.6. The cracking process of the unrestrained specimens immersed in strong sulfate solution can be seen in Fig. 3.7, Fig. 3.17 and Fig. 3.18. As shown in Fig. 3.7, a layer of mainly gypsum was formed from 133-day immersion, which indicated that the localized cracks were subparallel to the exposed surface with the distance from the exposed surface of around $250 \mu\text{m}$. It showed a similar tendency from Fig. 3.18 compared with Fig. 3.7. Several localized cracks which were subparallel to the exposed surface were found. The vertical cracks starting from the exposed surface were also found. Therefore, the crack pattern should be a combination of the horizon-

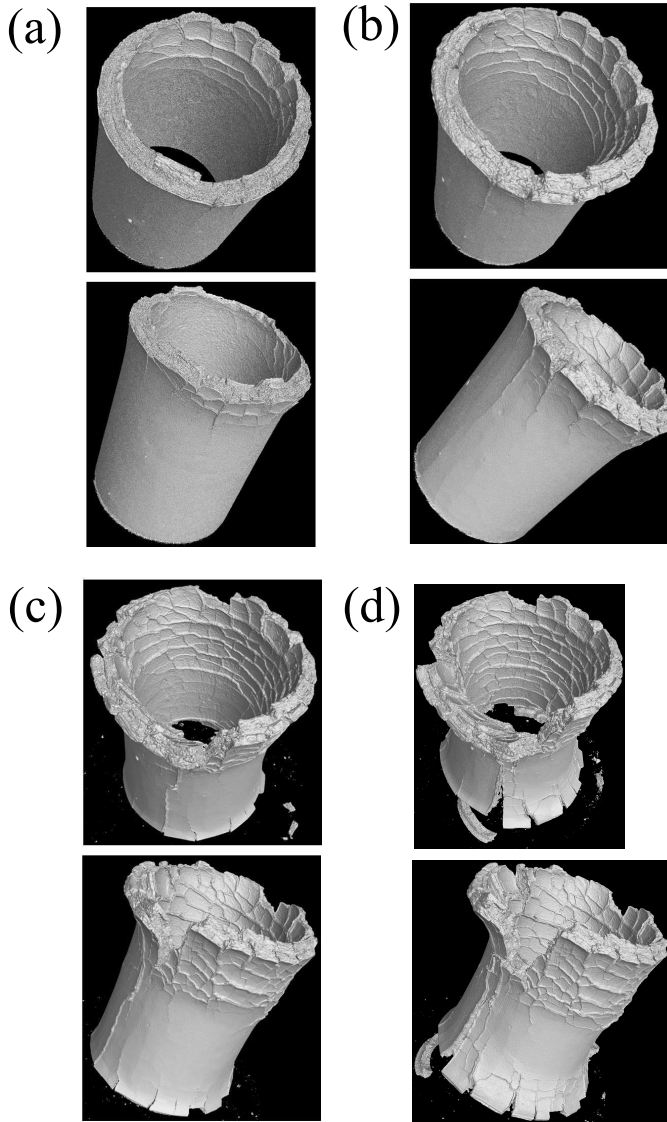


Figure 3.17: 3D renderings of unrestrained specimen (specimen 2) by CT scanning after (a) 294-day, (b) 343-day, (c) 420-day and (d) 469-day immersion in 30 g/L SO_4^{2-} .

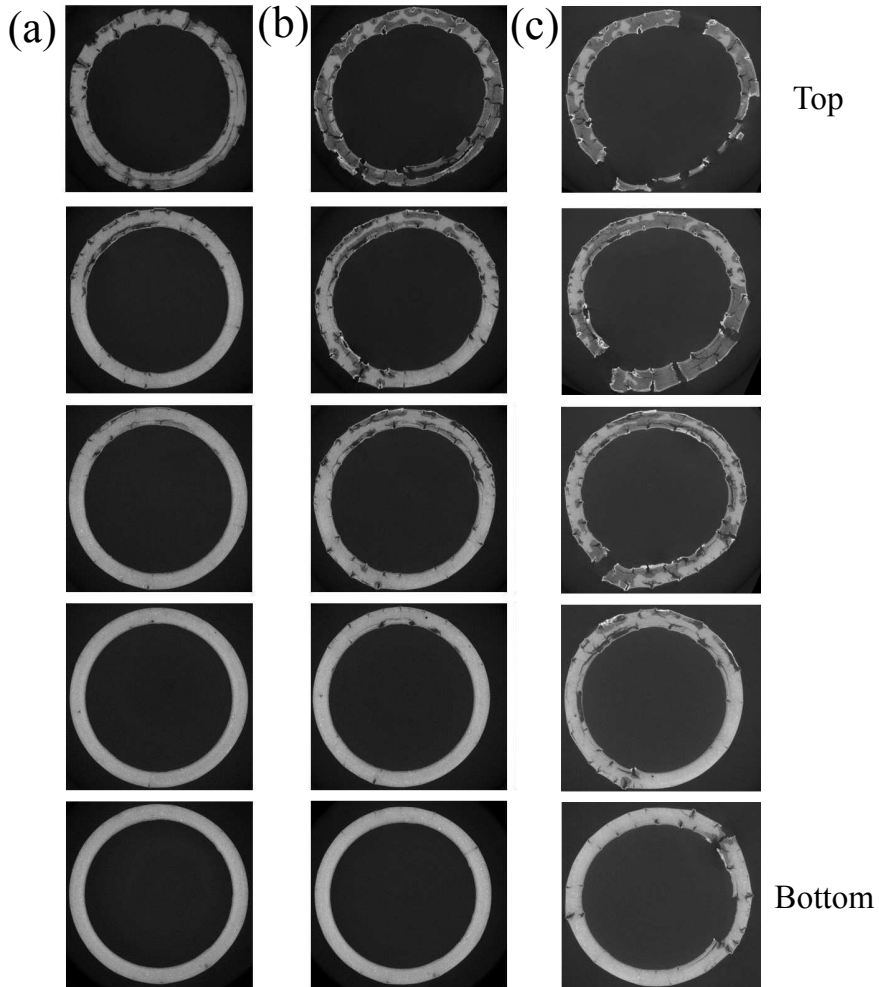


Figure 3.18: Reconstructed microtomography slices from top to bottom of unrestrained specimen (specimen 2) after (a) 294-day, (b) 343-day and (c) 420-day immersion in 30 g/L SO_4^{2-} .

tal cracks which started some distance away from the exposed surface and the vertical cracks which started from the exposed surface. The vertical crack means that the crack is along the longitudinal direction of the specimen. The horizontal crack represents that the crack is in the plane of the cross-section and along the tangential direction of the circle.

For the specimen immersed in strong sulfate solution under high-restraint condition (7 mm - 30 g/L) (specimen 3), the generated stress reached the highest value and began to decrease from 565-day immersion (Fig. 2.8), which means the specimen cannot carry more compressive stress at the two ends and turned to the process of being damaged. The highest generated stress was obtained as 13.4 MPa, however, the type of damage was still unknown. Therefore, the internal structure of the almost damaged specimen was studied at 581-day immersion by CT scanning, as shown in Fig. 3.19a. The 3D renderings after tomographic reconstruction is shown in Fig. 3.20a. The reconstructed microtomography slices were presented in Fig. 3.21a, which were chosen randomly from top to bottom of the specimen along the longitudinal direction. Several vertical cracks can be found on the surface of specimen in both of inner and outer circles of the pipe. In order to obtain a 3D view of the crack pattern which can show the internal cracks of specimen, image analysis was carried out based on the horizontal slices from Fig. 3.20a as described in section 3.3.2. The achieved 3D crack pattern is shown in Fig. 3.22a. It can be found that only several vertical cracks existed without any horizontal crack showing. If one vertical crack started from the surface of outer circle, another vertical crack also existed in the inner circle. These two vertical cracks were approximately along the same diameter direction and tended to connect to be a single crack, as shown in Fig. 3.21a and Fig. 3.22a. Because of the existence of 7 mm steel bar, the vertical deformation of specimen was severely restrained. Therefore, the specimen was not able to deform that much along vertical direction as the freely expanding specimen and deformed more along horizontal direction. Tensile splitting may occur, which may lead to the vertical cracks.

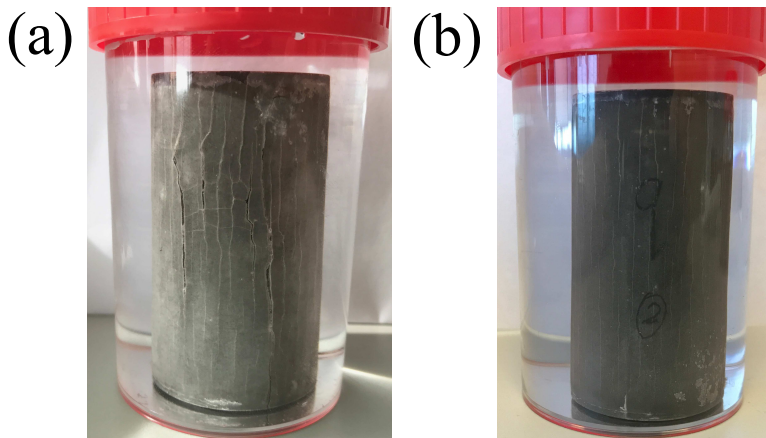


Figure 3.19: Restrained specimens immersed in 30 g/L SO_4^{2-} . (a) 581-day immersion under high-restraint condition (7 mm) (specimen 3) and (b) 765-day immersion under low-restraint condition (3 mm) (specimen 4).

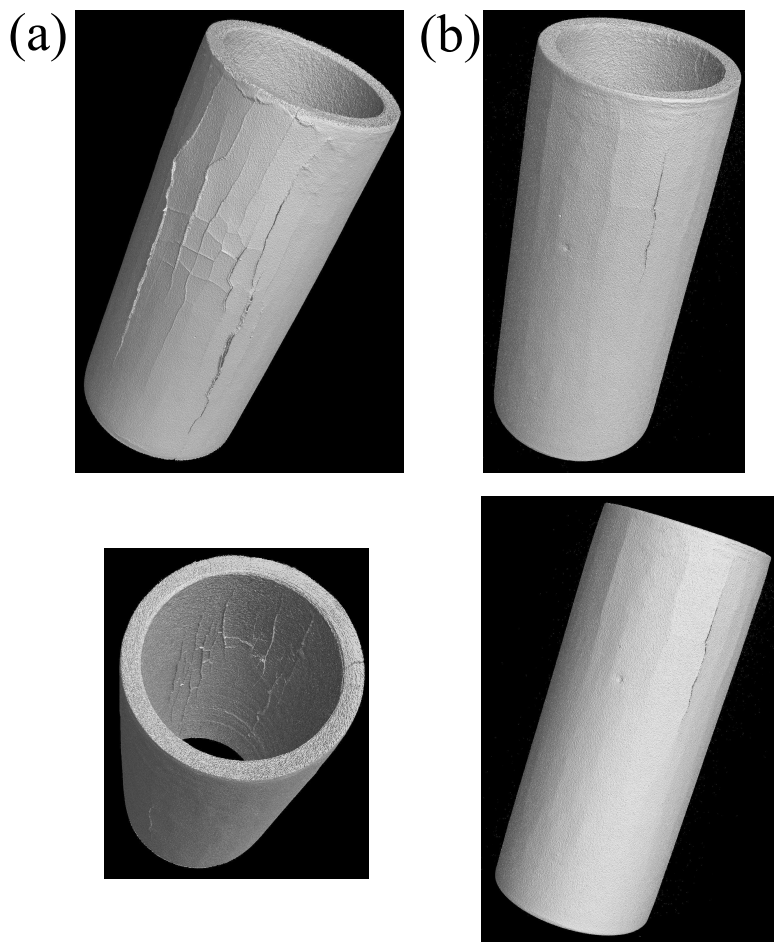


Figure 3.20: 3D renderings of restrained specimens immersed in 30 g/L SO_4^{2-} by CT scanning after (a) 581-day immersion under high-restraint condition (7 mm) (specimen 3) and (b) 765-day immersion under low-restraint condition (3 mm) (specimen 4).

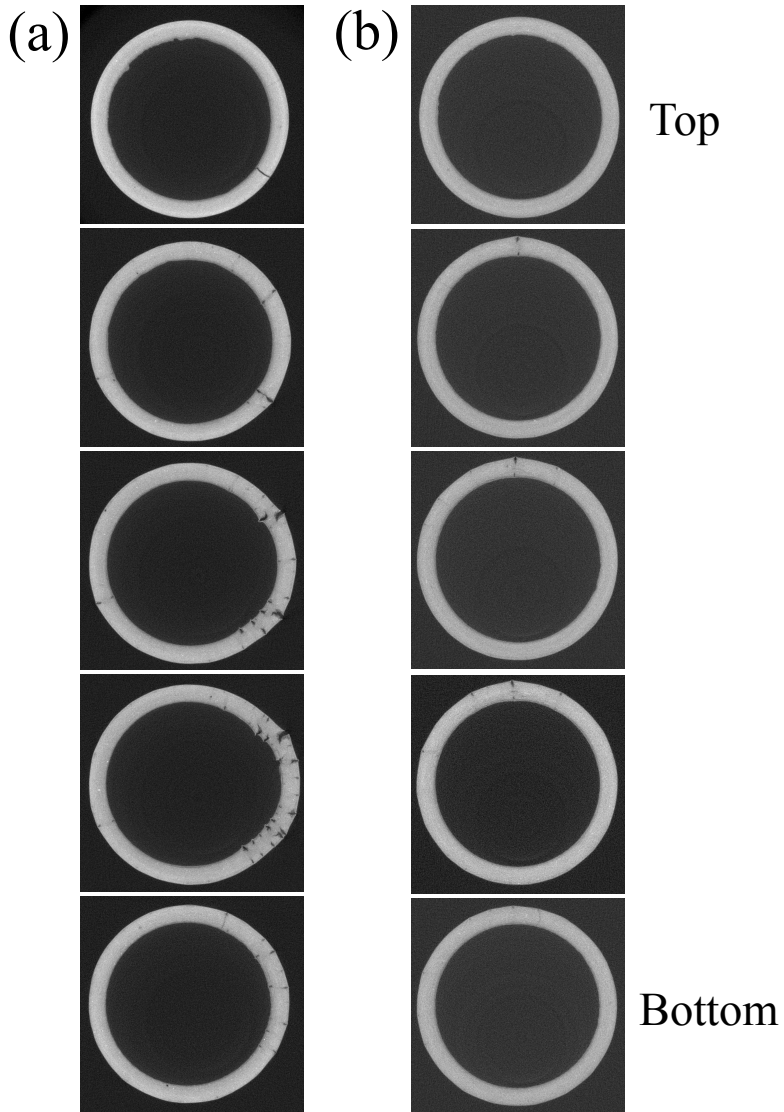


Figure 3.21: Reconstructed microtomography slices from top to bottom of restrained specimens immersed in 30 g/L SO_4^{2-} after (a) 581-day immersion under high-restraint condition (7 mm) (specimen 3) and (b) 765-day immersion under low-restraint condition (3 mm) (specimen 4).

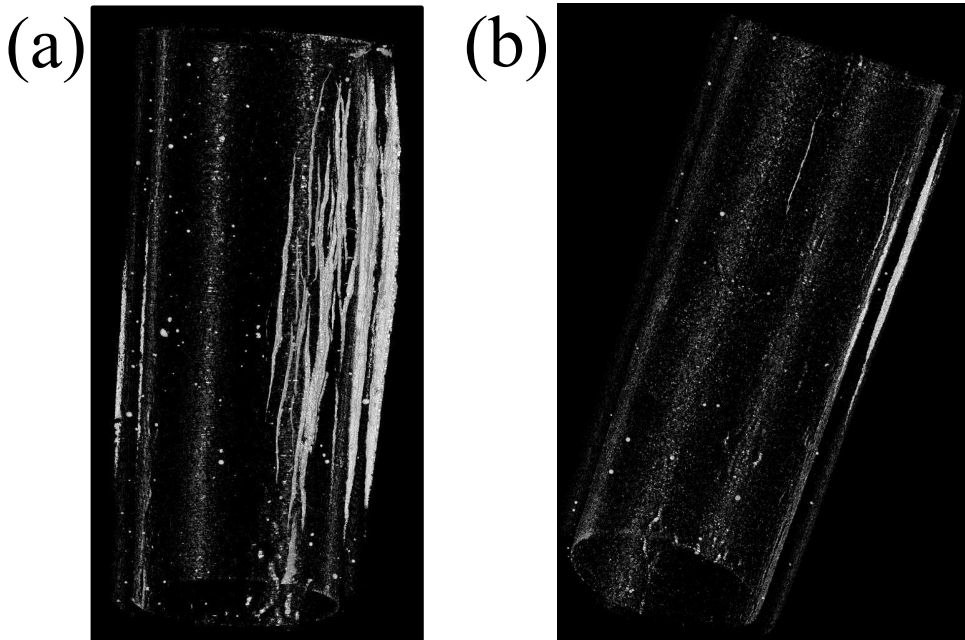


Figure 3.22: 3D crack pattern of restrained specimens immersed in 30 g/L SO_4^{2-} after (a) 581-day immersion under high-restraint condition (7 mm) (specimen 3) and (b) 765-day immersion under low-restraint condition (3 mm) (specimen 4). Based on Fig. 3.20 and Fig. 3.4.

For the specimen immersed in strong sulfate solution under low-restraint condition (3 mm - 30 g/L) (specimen 4), the generated stress reached the highest value and began to decrease from 628-day immersion (Fig. 2.8). The highest generated stress was 11.2 MPa. Then the internal structure of the specimen was studied at 765-day immersion by CT scanning, as shown in Fig. 3.19b. The 3D renderings after tomographic reconstruction is shown in Fig. 3.20b. And the reconstructed microtomography slices were presented in Fig. 3.21b. Image analysis was carried out to obtain the segmented cracks, as described in section 3.3.2. After the 3D construction of the images, a 3D view of the internal cracks of the specimen is shown in Fig. 3.22b. Several vertical cracks on the surface were observed in Fig. 3.19b. However, only one main vertical crack was found in Fig. 3.20b and Fig. 3.22b. Therefore, the specimen should be damaged with one main vertical crack. Several vertical cracks on the surface also existed, however, the depth of the cracks should be small. As a result, the vertical cracks cannot be detected by CT scanning due to the limited resolution compared with the crack size. As shown in Fig. 3.21b, if one vertical crack started from the surface of outer circle, another vertical crack also existed in the inner circle of the pipe. These two vertical cracks tended to coalesce as a single crack. Compared with specimen 3, the vertical deformation of specimen 4 was restrained under a lower level. Therefore, specimen 4 can deform more than specimen 3 along vertical direction, which means specimen 3 deformed more than specimen 4 along horizontal direction. More deformation along horizontal direction may lead to more vertical cracks, which explained the observation of one main vertical crack in specimen 4 and several vertical cracks in specimen 3.

3.5. SUMMARY AND CONCLUSIONS

IN this chapter, an experimental study on the damage caused by sulfate induced expansion was examined. The change of sulfur ingress profile at different exposure time was investigated based on SEM - EDS microanalysis. The crack pattern and crack development were studied by SEM and CT scanning. Image analysis was applied. Based on the experimental results and discussions, the following conclusions can be drawn:

- The sulfur distributions of unrestrained specimens immersed in weak and strong sulfate solutions were examined and analyzed. It was observed that sulfur accumulated in the hydrated matrix, which indicated the location of the newly formed sulfur-containing phases.
- For the unrestrained specimens immersed in weak sulfate solution, the sulfur ingress profile had a notable gradient along the penetration depth at 21-day immersion. Then an almost uniform sulfur distribution was found at 189-day immersion and no localized cracks were observed. However, for the unrestrained specimens immersed in strong sulfate solution, a layer of sulfur-rich phases was observed under SEM at 133-day immersion. The layer was subparallel to the exposed surface with the distance from the exposed surface of around 250 μm . Therefore, a stronger sulfate solution can lead to an earlier crack localization.
- In the initial stage before the formation of localized cracks, the amount of newly formed sulfur-containing phases was dominant by the diffusion speed of external

sulfate ions. Stronger sulfate solution resulted in faster penetration. Therefore, when the exposure time was equal, a stronger sulfate solution resulted in a larger sulfur gradient. As a result, a stronger sulfate solution can lead to a larger gradient of local expansive pressure. Therefore, the main difference between the weak and strong sulfate solution is the pressure gradient. The localized cracks can be formed when the pressure gradient is large enough.

- No visually noticeable cracks were observed on the specimens immersed in weak sulfate solution up to 807-day immersion. However, all the unrestrained and restrained specimens immersed in strong sulfate solution were damaged noticeably before 807-day immersion. Therefore, a stronger sulfate solution can lead to a faster degradation.
- The internal structure of the damaged specimens immersed in strong sulfate solution was studied. For the unrestrained specimens, a combination of the horizontal cracks which started some distance away from the exposed surface and the vertical cracks which started from the exposed surface was observed. For the high restrained specimen (7 mm - 30 g/L), several vertical cracks were found. For the low restrained specimen (3 mm - 30 g/L), only one main vertical crack was observed. Therefore, the level of external restraint influences the damage type of the specimens.

4

MICROSTRUCTURAL EVOLUTION OF CEMENT PASTE EXPOSED TO STRONG SODIUM SULFATE SOLUTION

This chapter focuses on the complex process of crack initiation and propagation during material degradation at microscopic scale. The damage evolution of cement paste samples immersed in 30 g/L sodium sulfate solution was investigated experimentally. SEM - EDS microanalysis and image analysis were applied. The localization process of the subparallel cracks near the exposed surface at the depth of about 250 μm was studied. Progressive precipitation of gypsum crystals inside the localized cracks was found. The change of sulfur gradient versus exposure time was analyzed. Based on that, the change of expansive pressure gradient versus exposure time was discussed.

4.1. INTRODUCTION

EXTERNAL sulfate attack is a progressive durability problem for concrete structures exposed to aggressive environment rich in sulfate ions. Sulfate ions can penetrate into hardened cement matrix, and react with cement hydration products to form metal sulfates such as ettringite and thaumasite, as well as gypsum when stronger sulfate concentrations are present [20–23]. The reactions between sulfate ions and cementitious phases are known to be complex in which ionic transport, expansive reactions and mechanical damage interact with each other. These aspects gradually increase macroscopic expansion and cause severe mechanical damage.

For the external sulfate induced research, expansion measurement is the most common method to evaluate the sulfate resistance. Several other parameters are also concerned regarding the concrete degradation, such as loss or increase of mass, strength and elastic modulus decrease [78, 86]. However, the complex process of crack initiation and propagation has been rarely studied. The ingress of external sulfate ions is a process, which involves a dynamic gradient of internal expansive pressure along the diffusion direction. The influence of dynamic pressure gradient has been largely neglected. In this chapter, the damage evolution of cement paste samples immersed in strong sodium sulfate solution was investigated. The crack development and gypsum precipitation were studied based on experimental observations at microscopic scale. The sulfur gradient before exposure and after 70-day, 105-day and 133-day exposure was analyzed. Based on that, the dynamic gradient of internal pressure was discussed. The study in this chapter aims at understanding the effect of internal pressure gradient on the crack initiation and propagation due to external sulfate attack.

In chapter 3, SEM-EDS microanalysis was carried out on the specimens exposed to weak (1.5 g/L) and strong (30 g/L) sodium sulfate solutions. The purpose is to obtain the sulfur profiles at different immersion days. In this chapter, SEM-EDS microanalysis was also carried out on the specimens exposed to the strong sodium sulfate solution (30 g/L). The experimental methods in these two chapters are same. However, this chapter focuses more on the analyses based on the experimental results. Chapter 3 only considers sulfur. In this chapter, sulfur, aluminum and calcium combined with BSE micrographs were all considered. The experimental details regarding specimens, sample preparation and SEM-EDS technique can be found in section 3.2.1.

4.2. IMAGE ANALYSIS

4.2.1. BSE MICROGRAPH

THE intensity of BSE signal is mainly a function of the average atomic number of the local area of the sample [112]. Pores and cracks are filled by epoxy. The average atomic number of epoxy is much lower than that of cement hydration products. Also cement hydration products have much lower average atomic numbers than anhydrous cement particles [92, 113]. BSE micrograph is a 8-bit gray-scale digital image. The gray level extends from 0 (black) to 255 (white). The phase with greatest average atomic number is the brightest, and that with lower average atomic number is darker, as shown in Fig. 4.1. Image segmentation was performed individually on the basis of gray level histogram of each image [114–116]. As a result, three phases can be isolated: pore (crack),

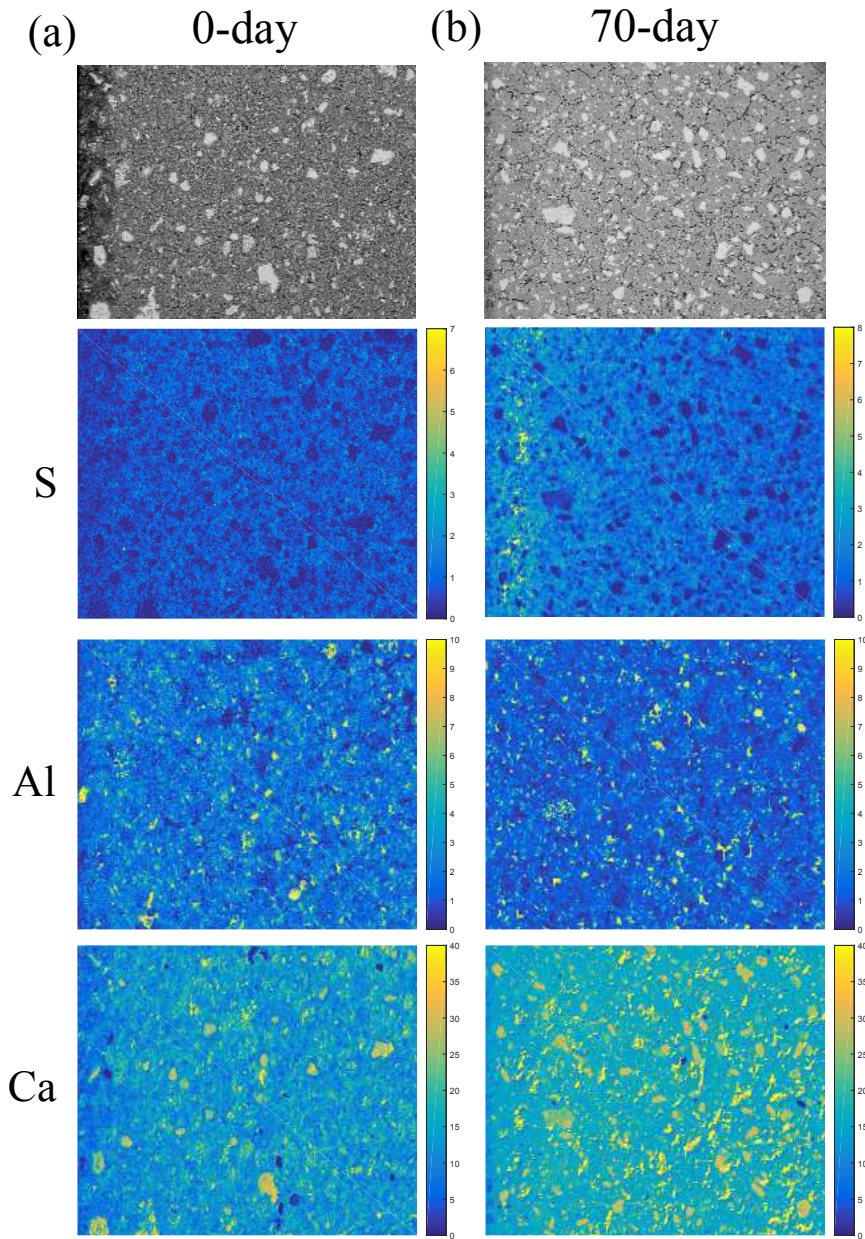


Figure 4.1: BSE micrographs and rescaled EDS elemental distribution maps in atomic percentage (%) for (a) 0-day, (b) 70-day, (c) 105-day and (d) 133-day immersion in 30 g/L SO_4^{2-} . Left edge of each image was the exposed surface. From top to bottom: BSE micrograph, sulfur distribution map, aluminum distribution map and calcium distribution map

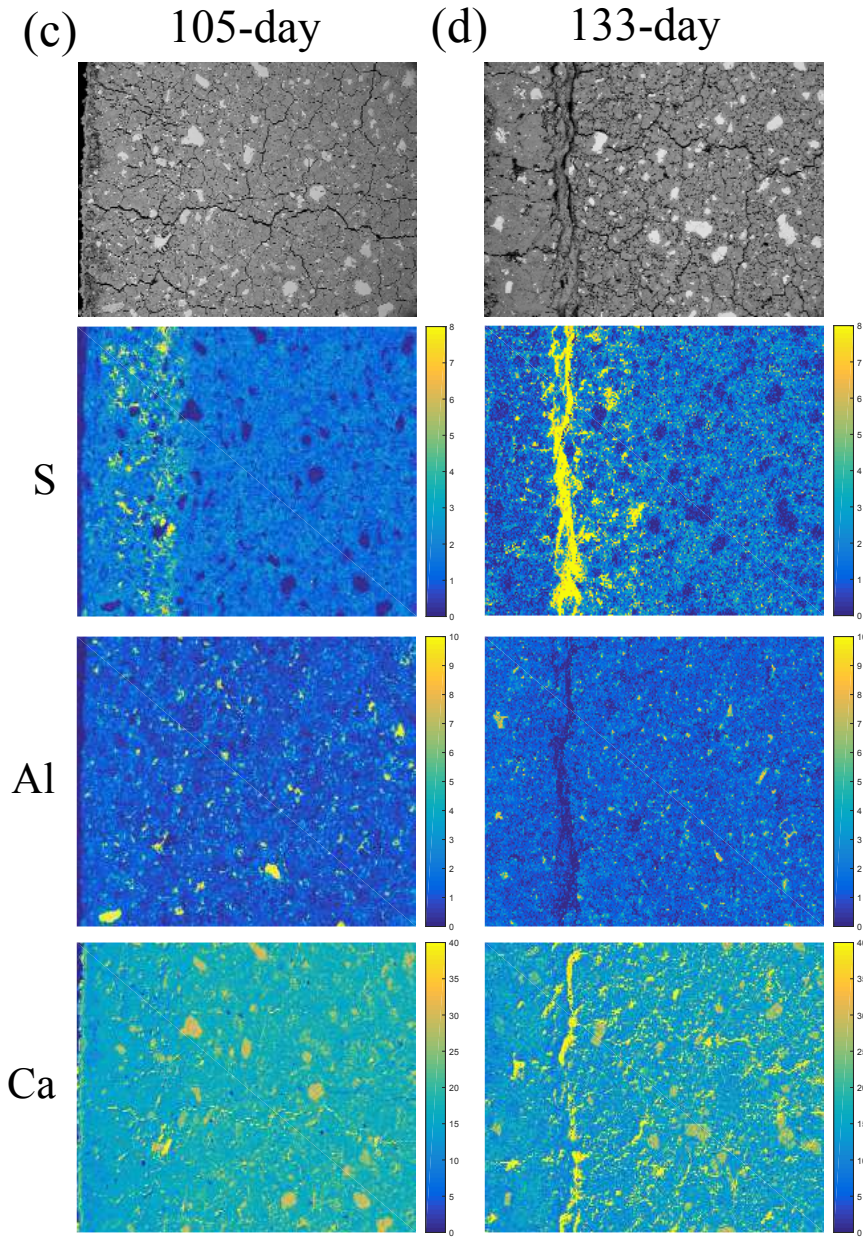


Figure 4.1: (continue) BSE micrographs and rescaled EDS elemental distribution maps in atomic percentage (%) for (a) 0-day, (b) 70-day, (c) 105-day and (d) 133-day immersion in 30 g/L SO_4^{2-} . Left edge of each image was the exposed surface. From top to bottom: BSE micrograph, sulfur distribution map, aluminum distribution map and calcium distribution map

cement hydration product and anhydrous cement particle, which are displayed as black, gray and white in Fig. 4.2, respectively. Cement hydration product is a mixture of several products (eg: C-S-H, calcium hydroxide and monosulfate).

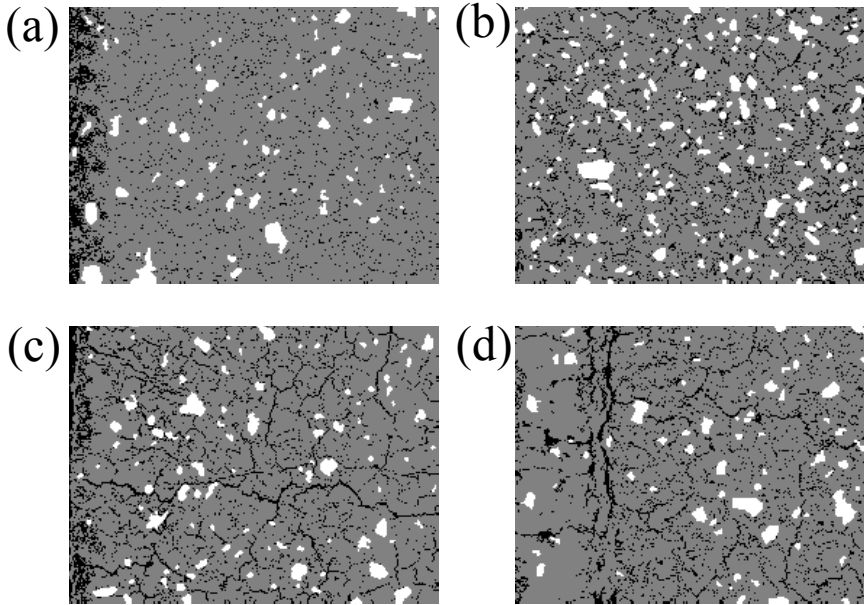


Figure 4.2: Segmented microstructure for (a) 0-day, (b) 70-day, (c) 105-day and (d) 133-day immersion in 30 g/L SO_4^{2-} (black - pore or crack, gray - cement hydration product, white - anhydrous cement particle).

4.2.2. EDS ELEMENTAL DISTRIBUTION MAP

The acquired EDS elemental distribution map is a scaled image in which the characteristic X-rays for each element of interest at each analysis point (pixel in elemental distribution map) are counted and uniformly scaled to be the gray level from 0 to 255 [98–101]. The intensity of the elemental map is proportional to the element concentration, which can reflect the relative relation of element concentration at each pixel. However, the real element concentration cannot be obtained directly because of the scaled intensity value. Meanwhile, the highest normalized concentration of each element was recorded in the EDS software, which is related to the gray value of 255 in the scaled elemental map and can be used for the image rescaling. Therefore, a MATLAB code for image rescaling was developed to get the normalized atomic percentage or weight percentage of the element at each pixel. The rescaled elemental distribution maps based on atomic percentage are shown in Fig. 4.1. In order to show the results clearly, the sulfur atomic percentages above 8 %, the aluminum atomic percentages above 10 % and the calcium atomic percentages above 40 % were displayed as 8 %, 10 % and 40 %, respectively.

4.2.3. COMBINED ANALYSIS

After the image segmentation of BSE micrographs and the rescaling of EDS elemental distribution maps, several combined analyses were done with MATLAB codes, which mainly included two purposes.

The first purpose was to get single element ingress profile, such as sulfur ingress profile along diffusion direction. Based on the rescaled sulfur distribution map in weight percentage and the segmented microstructure, only the pixels belonging to hydration product were counted, which represents the area with gray color in Fig. 4.2. Then the average of the counted pixels in sulfur weight percentage along each column (parallel to the exposed surface) was calculated, and a single value was obtained for each column. The obtained value represents the average sulfur weight percentage at the corresponding penetration depth.

The second purpose was to compare different element concentrations at the same pixel location. Sulfur/calcium atomic ratio was taken as an example. Based on the rescaled sulfur distribution map in atomic percentage, the rescaled calcium distribution map in atomic percentage and the segmented microstructure, only the pixels belonging to hydration product were counted. Then the sulfur/calcium atomic ratio at each counted pixel was calculated.

4.3. RESULTS AND DISCUSSION

SULFUR profiles were calculated by image analyses on the EDS sulfur distribution maps in weight percentage. Fig. 4.3 presents the results for samples before exposure as well as after 70-day, 105-day and 133-day immersion in 30 g/L sodium sulfate solution. The depth in the figure stands for the distance from the exposed surface, which is in contact with the aggressive solution. A remarkable gradient of sulfur content along diffusion direction can be found in the sulfur profile at 70-day immersion. The profile shows three distinct parts: a near-surface reduced sulfur content in solid phases due to leaching, a maximum sulfur content peak and a gradual decrease in sulfur content.

Based on Fig. 4.1d and Fig. 4.3, three zones can be identified from the surface inwards, which are the zone with an ingress depth between 0 mm and 0.25 mm (zone 1), the zone with an ingress depth between 0.25 mm and 0.5 mm (zone 2) and the zone with an ingress depth between 0.5 mm and 1.25 mm (zone 3). It was found that, after 70-day immersion, the sulfur content in zone 2 increases drastically, however, the sulfur content in zone 1 decreases slowly.

4.3.1. PRECIPITATION OF GYPSUM

Each single analysis spot is a summary of one pixel from the images, which covers an area of about $5 \times 5 \mu\text{m}^2$. Due to the fine intermixing of the hydration phases in the interaction volume at each analysis spot, most of the data points correspond to a mixture of several phases, such as calcium-silicate-hydrate (C-S-H), calcium hydroxide (CH), monosulfate (AFm), ettringite and gypsum. The problem can be walked around considering elemental ratios rather than absolute element concentrations.

Phases and phase intermixes can be identified based on plots of elemental atomic ratios. As marked in Fig. 4.4, pure ettringite has a composition of $S/\text{Ca} = 0.5$ and Al/Ca

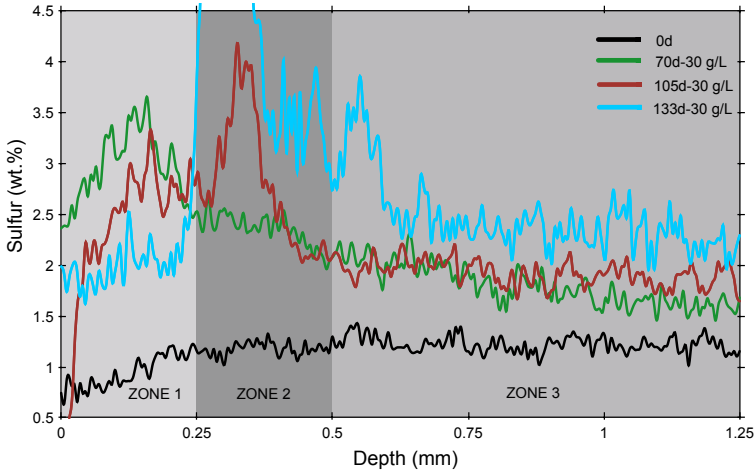


Figure 4.3: Sulfur profiles of hydration product pixels along the diffusion direction

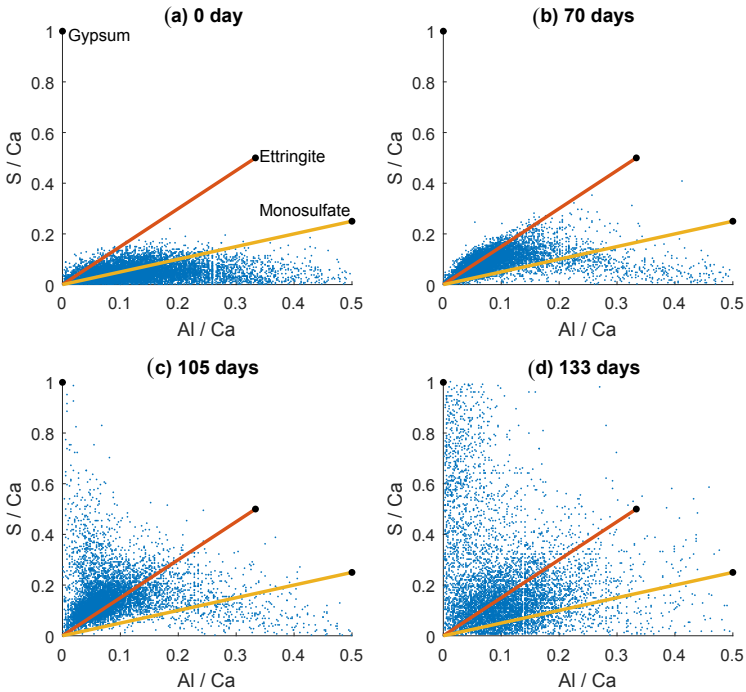


Figure 4.4: EDS plots of S/Ca versus Al/Ca atomic ratios on hydration product pixels at penetration depth between 0.25 mm and 0.5 mm (zone 2) for (a) 0-day, (b) 70-day, (c) 105-day and (d) 133-day immersion in 30 g/L SO_4^{2-}

= 1/3 in atomic ratio. For pure gypsum, the atomic ratios are $S/Ca=1$ and $Al/Ca=0$. If ettringite or gypsum is mixed with C-S-H or CH, the S/Ca and Al/Ca atomic ratios decrease due to the increase of calcium content. However, the S/Al atomic ratio can reflect the relative relation between ettringite content and gypsum content, which is the slope in Fig. 4.4.

The S/Al atomic ratio of an ideal ettringite crystal is 1.5. Therefore, gypsum should exist if the analysis spot has a slope larger than 1.5 in the plots. When gypsum content in the interaction volume becomes higher, the slope of data points also increases. Fig. 4.4 presents the plots of all the analysis spots of hydration product in zone 2 at different immersion days. As shown in the plots, only few amount of gypsum can be found for the samples before exposure and after 70-day immersion. Then a lot of gypsum was available at 105-day immersion. However, the S/Ca atomic ratio of most analysis spots was not high, which indicated gypsum was mixed with C-S-H or CH in most pixel areas. After that, even a cloud of mainly pure gypsum appeared at 133-day immersion. These results explained the phenomenon of fast sulfur increase in zone 2 in Fig. 4.3, which was due to the continuous precipitation of gypsum.

4.3.2. CRACK INITIATION AND PROPAGATION

For most analysis spots, ettringite and gypsum were mixed with C-S-H or CH, which led to that S/Ca and Al/Ca atomic ratios were lower than the pure phase. Therefore, the S/Al atomic ratio seems to be an important value to reflect the relative content between ettringite and gypsum. Gypsum should exist when the S/Al atomic ratio is larger than 1.5. Then the increase of S/Al atomic ratio can reflect a higher percentage of gypsum content in all the sulfur-containing phases.

Fig. 4.5a displays the pixels with S/Al atomic ratio above 1.5 as white, therefore the white pixels indicate the existence of gypsum. Comparing the results at 70-day immersion with that at 0-day immersion, it can be found the amount of white pixels in zone 1 at 70-day immersion increased noticeably, and the amount of white pixels in zone 3 at 70-day immersion is similar as that at 0-day immersion. However, the sulfur content in zone 3 at 70-day immersion in Fig. 4.3 was much higher than that at 0-day immersion, which indicated the existence of ettringite was responsible for the sulfur increase in zone 3 at 70-day immersion. Afterwards, numerous white pixels appeared in zone 3 at 105-day immersion, which suggested that the formation of ettringite took place first thereafter began the gypsum precipitation. The phenomenon can be understood as the external sulfate ions first reacted with fine AFm crystals embedded in C-S-H to form ettringite [11]. The formation of ettringite in nanopores occurred when the supersaturated condition was reached, which led to a significant local expansive pressure. As the sulfate ions continued to penetrate, they reacted with Ca^{2+} to form gypsum, which consumed Ca^{2+} from solution and more CH were decomposed into the pores.

Considering one pixel area of about $5 \times 5 \mu m^2$ (one analysis spot), the formation of ettringite in small pores (much smaller than $5 \mu m$) may exert significant expansive pressures on the pore wall. The microcracks can happen upon the pressure building up. Afterwards, gypsum precipitated in the formed microcracks. Therefore, it can be assumed that the precipitation of gypsum in microcracks leads to a higher gypsum content in the pixel area. This may indicate a higher degree of damage in the same pixel area. In

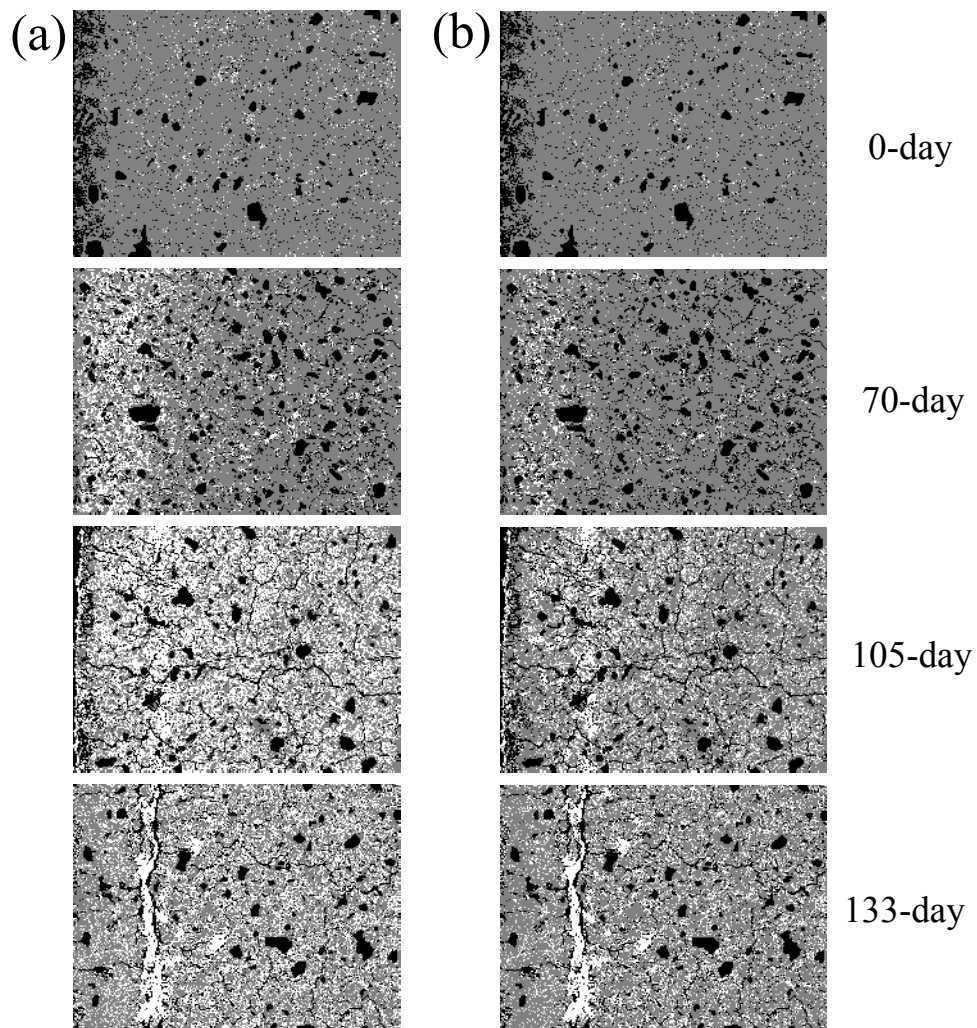


Figure 4.5: Images of pixels with (a) $S/Al > 1.5$, (b) $S/Al > 2$, (c) $S/Al > 2.5$, (d) $S/Al > 4$ in atomic ratio. Display as white. Left edge of each image was the exposed surface. From top to bottom: 0-day, 70-day, 105-day and 133-day immersion in 30 g/L SO_4^{2-}

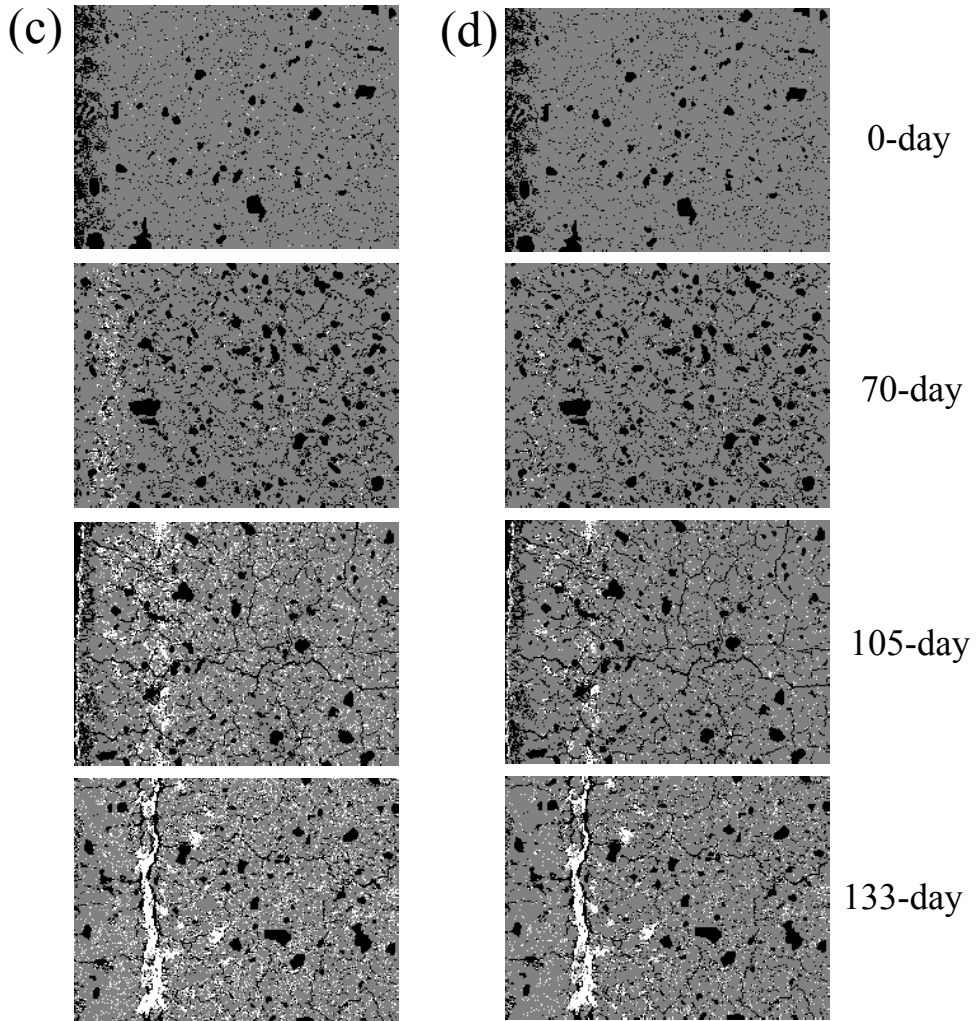


Figure 4.5: Images of pixels with (a) $S/Al > 1.5$, (b) $S/Al > 2$, (c) $S/Al > 2.5$, (d) $S/Al > 4$ in atomic ratio. Display as white. Left edge of each image was the exposed surface. From top to bottom: 0-day, 70-day, 105-day and 133-day immersion in 30 g/L SO_4^{2-}

this study, it is assumed that more content of gypsum in one pixel area indicates more damage of that pixel area.

Meanwhile, a higher S/Al atomic ratio in one pixel can reflect a higher percentage of gypsum content of all the sulfur-containing phases. Therefore, it can be assumed that a higher S/Al atomic ratio may illustrate the formation of more microcracks in the pixel area, when the S/Al atomic ratio is above 1.5. The pixels with S/Al atomic ratios above 1.5, 2, 2.5 and 4 are displayed in white in Fig. 4.5a, Fig. 4.5b, Fig. 4.5c and Fig. 4.5d, respectively.

The cracks observed on the BSE micrographs can be caused by sulfate attack or material drying during sample preparation or SEM observation. However, the cracks which are filled with gypsum should be caused by sulfate attack. As shown in Fig. 4.1d, the localized cracks were clearly found with a layer of mainly pure gypsum at 133-day immersion. Before the localized cracks occurred, the distributed cracks should also have been formed which might have been filled by gypsum and therefore was not observed through the BSE imaging. Hence, the pixels with high gypsum content can be considered as the indication of crack locations.

The white pixel area with a higher S/Al atomic ratio in Fig. 4.5 can represent more damage of the local material (one pixel area) following gypsum participation. Fig. 4.5c is taken as an example to estimate the process of crack initiation and propagation. The pixel area with a S/Al atomic ratio above 2.5 was considered to be damaged at certain level, which was simply defined as cracked material. Few white pixels were distributed uniformly before sulfate exposure (0-day immersion). Then numerous distributed white pixels were observed in zone 1 at 70-day immersion, which indicated the occurrence of distributed cracks in zone 1. Afterwards, at 105-day immersion, distributed and connected white pixels began to appear along a line in zone 2, which was subparallel to the exposed surface. It can be understood as that the distributed cracks were formed and the localized cracks also began to occur in zone 2. Finally, a line of white pixels can be seen at 133-day immersion, which means a main crack was formed because of crack localization. As a summary, the distributed cracks occurred in zone 1 at 70-day immersion. Afterwards, localized cracks began to appear at 105-day immersion at a distance of around 250 μm from the exposed surface. Finally, localized cracks coalesced and a main crack was observed at 133-day immersion.

4.3.3. DEVELOPMENT OF INTERNAL EXPANSIVE PRESSURE

As mentioned above, ettringite formed in nanopores may exert significant expansive pressure on the pore wall. The formation of gypsum in the initial stage may also result in local expansive pressure [39, 41]. Then the microcracks can form upon the pressure build up. Once the microcracks were formed, gypsum began to precipitate in the formed microcracks, which possibly has a negligible contribution to the expansive pressure. However, in Fig. 4.3, the sulfur profiles contain the sulfur from both ettringite and gypsum. For the pixels with higher gypsum content, most of the sulfur in those pixels belongs to the gypsum crystals which participate in the microcracks and should not be included in the pressure calculations. As shown in Fig. 4.5c, pixels with S/Al atomic ratio above 2.5 was considered as the high gypsum content area, which was caused by gypsum precipitation in the microcracks. Therefore, in order to avoid overestimation,

only the sulfur profiles representing the pixels with a S/Al atomic ratio of 2.5 or less were assumed contributing to the internal pressure calculation. The new sulfur profiles are presented in Fig. 4.6.

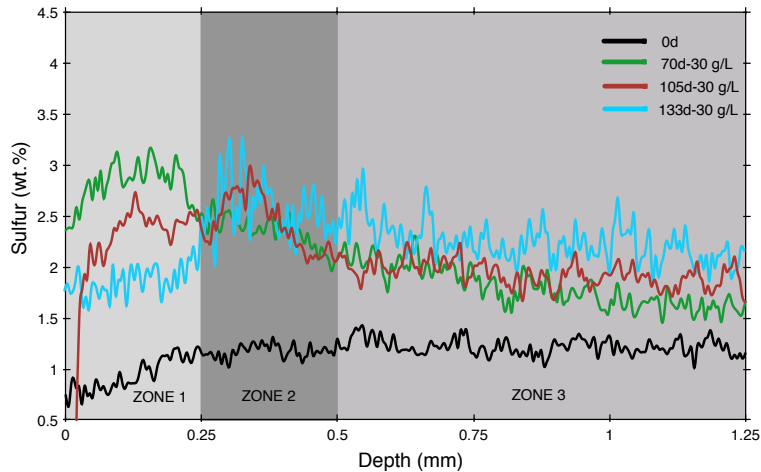


Figure 4.6: Sulfur profiles of hydration product pixels along the diffusion direction excluding the pixels with S/Al>2.5 in atomic ratio.

As can be seen in Fig. 4.6, a noticeable negative slope of sulfur content between the first and second zones can be found at 70-day immersion, which indicates a large gradient of internal expansive pressure along diffusion direction. Under this condition, the first zone can be expected to expand more compared with the second zone where sulfur content was lower than the former. Therefore, the first zone is under compressive stress and the second zone is subject to tensile stress due to deformation compatibility. A larger pressure gradient can lead to a higher tensile stress in the second zone. When the tensile stress exceeds the material strength, the material is damaged. Therefore, a steep gradient of internal expansive pressure can lead to the localized cracks.

The pressure gradient at 70-day immersion was not large enough to form the localized cracks, thus the sulfur content in zone 1 may continue increasing after 70-day immersion to generate localized cracks at the boundary between zone 1 and zone 2, which may happen between 70-day and 105-day immersion. Once the localized cracks occurred, increasingly more gypsum began to precipitate in the localized cracks. Moreover, the smaller sulfate-bearing crystals tended to dissolve and transfer their ions to a larger crystal in an adjacent pore [54, 55, 111]. Therefore, the gypsum and even ettringite in zone 1 were dissolved and their ions moved into the localized cracks slowly, which explains the phenomenon of sulfur decreasing in zone 1 after 70-day immersion in Fig. 4.3 and Fig. 4.6. Finally, with the expansive pressure developing, the localized cracks developed to coalesce into a main crack at 133-day immersion.

On the other hand, even though the pressure gradient before 70-day immersion was not large enough to form the localized cracks, the distributed cracks can occur. The heterogeneity of material and internal pressure distribution leads to internal restraints

in material, which results in local stresses (eigenstresses) in material after deformation compatibility. Once the eigenstress exceeds the material strength, crack in the material occurs. Therefore, the distributed cracks in zone 1 at 70-day immersion may be caused by the heterogeneity of material and pressure distribution.

It was found that the sulfur content in zone 3 kept rising with exposure time increasing, which means the internal expansive pressure kept growing. Considering the small thickness of the specimen, the pressure gradient was not enough to form another localized crack. However, for the concrete structures, the size of the cross-section is large. Therefore, after one layer is damaged, the surface of the undamaged part will be exposed to sulfate solutions. Then the pressure gradient will increase again to damage another layer in the inner part. Finally, the concrete structures will be damaged layer by layer from the surface inwards.

4.4. SUMMARY AND CONCLUSIONS

IN this chapter, an experimental study on the crack initiation and propagation of specimens immersed in 30 g/L sodium sulfate solution was presented. The specimens before exposure and after 70-day, 105-day and 133-day exposure were investigated. The atomic ratios of sulfur/calcium, aluminum/calcium and sulfur/aluminum were analyzed based on SEM - EDS microanalysis. Image analyses were applied for microstructure segmentation and phase analysis. Based on the experimental results and discussions, the following conclusions can be drawn:

- Three zones are identified from the surface inwards for the specimens exposed to 30 g/L sodium sulfate solution. The sulfur content in zone 2 increased fast after 70-day immersion, which was caused by the continuous precipitation of gypsum.
- It was found that the distributed cracks occurred in zone 1 at 70-day immersion. Afterwards, localized cracks appeared at 105-day immersion at a distance of around 250 μm from the exposed surface. Once the localized cracks were formed, more and more gypsum kept precipitating in the formed cracks. Finally, localized cracks connected with each other and a main crack was formed at 133-day immersion, which was subparallel to the exposed surface. The main crack was filled with mainly pure gypsum.
- Due to the penetration process of external sulfate ions, a dynamic gradient of internal expansive pressure along diffusion direction existed. The part with more internal pressure is expected to expand larger compared with the part with less internal pressure. Therefore, the first part is under compressive stress and the second part is subject to tensile stress due to deformation compatibility.
- The crack localization was mainly due to a critically steep gradient of internal expansive pressure. A large pressure gradient was found at 70-day immersion. Afterwards, the pressure gradient kept increasing until the localized cracks were formed. The location of the localized cracks depends on the pressure gradient. In the case in this study, the localized cracks occurred at a distance of around 250 μm from the exposed surface.

- The heterogeneities of material and internal pressure lead to internal restraints in material, which result in local stresses (eigenstresses) in material after deformation compatibility. Once the eigenstress exceeds the local material strength, crack in the local material occurs. This can cause local distributed cracks, which may result in localized cracks depending on the eigenstress distribution. The gradient of internal pressure influences the eigenstress distribution. Before 70-day immersion, the internal pressure gradient was not large enough to form localized cracks. However, nonuniform pressure distribution existed in the heterogeneous material, which led to the distributed cracks at 70-day immersion.

4.5. DISCUSSION OF RESULTS FROM PART 2 AND CONCLUSIONS

PART 2 of the thesis contains all the experimental investigations related to external sulfate attack in this study, which includes chapter 2, 3 and 4. These three chapters are related with each other. For some issues, the conclusions cannot be drawn without combining all the experimental results in the three chapters, which are discussed in this section.

- *The fracture of the specimen caused by the internal pressure is different from that caused by the external loading.*

As observed in section 2.3.1, the free expansions of the specimens exposed to weak and strong sulfate solutions were 0.173% and 1.364% at 189-day immersion, respectively. The specimens without sulfate exposure subjected to the uniaxial tensile loading were also studied in chapter 5. Tensile strength of around 5.7 MPa with the strain of around 0.031% was obtained. It is found that the free expansions caused by external sulfate attack at 189-day immersion are far more than the elastic limit of the specimens subjected to the uniaxial tensile loading. However, no visually noticeable cracks were observed in both weak and strong sulfate solutions for freely expanding specimens until 189-day immersion. Only for the sample immersed in strong sulfate solution after 133-day immersion, continuous micro-cracks filled with mainly gypsum crystals started to form, which was discussed in chapter 4. Therefore, the fracture of the specimen caused by the internal pressure should be different from that caused by the external loading.

For the specimen subjected to the uniaxial tensile loading, the crack localization is easy to occur once the first crack is formed. However, for the freely expanding specimen under internal expansive pressure in this study, the crack localization was caused by the steep gradient of local internal pressure, as discussed in chapter 4. Even though the value of the local internal pressure is high, a small pressure gradient along the diffusion direction may result in only deformation and distributed cracks. In this study, the pressure gradient at 189-day immersion was not large enough yet to cause the observed damage, which explained the phenomenon that no visually noticeable cracks were observed. However, the formed distributed cracks can lead to large deformation, which is far more than the elastic limit of the specimens subjected to the uniaxial tensile loading.

- *The three stages for the freely expanding specimen immersed in strong sulfate solution (30 g/L).*

As discussed in section 2.3.1, the attack process for the freely expanding specimen immersed in strong sulfate solution is suggested to be divided into three stages: the first stage (from 0-day to 98-day immersion), the second stage (from 98-day to 350-day immersion) and the third stage (from 350-day immersion).

The crack development of the freely expanding specimen immersed in strong sulfate solution was discussed in chapter 3 and 4. The crack initiation and propagation of the specimens before 189-day immersion can be found in Fig. 4.5c and Fig. 3.7. The cracking process of the specimens between 294-day and 469-day immersion is presented in Fig. 3.16 and Fig. 3.17.

It is found that the localized cracks began to occur between 70-day and 105-day immersion (Fig. 4.5c). The start of stage 2 (98-day immersion) is in this time interval. Therefore, the acceleration of the free expansion in stage 2 should be caused by the crack localization. Then, during stage 2, more and more localized cracks were formed, as shown in Fig. 3.7e (189-day immersion), Fig. 3.16a (294-day immersion) and Fig. 3.16b (343-day immersion). After that, the localized cracks began to coalesce and the large main cracks started to occur, which led to a rapid damage of the specimen (stage 3), as presented in Fig. 3.16c (420-day immersion) and Fig. 3.16d (469-day immersion).

- *The damage type of the specimen under unrestrained condition is different from that under restrained condition.*

Three types of longitudinal restraints were applied on the cement paste pipes in this study: non-restraint, low-restraint and high-restraint conditions. The crack patterns of the damaged specimens under the three types of restraint exposed to strong sulfate solution (30 g/L) were studied in chapter 3. For the unrestrained specimens, a combination of the horizontal cracks and the vertical cracks was found. However, for the restrained specimens, only vertical cracks were observed. The vertical crack is along the longitudinal direction of the specimen. The horizontal crack is in the plane of the cross-section and along the tangential direction of the circle. The differences of the crack patterns indicate that the damage types of the specimens under unrestrained and restrained conditions are different.

For the specimens under restrained conditions, the specimens tended to expand. However, they were restrained by the steel bars. Therefore, the steel bars were under tensile stress, while the specimens were under compressive stress. The internal expansive pressure caused by the external sulfate attack led to expansion of the specimens, however, the specimens were in fact under external compressive stress at the restrained boundaries. In this case, the whole specimen may be damaged due to tensile splitting in the final stage.

However, the unrestrained specimens can expand freely without any external loading. As discussed in chapter 4, the heterogeneities of material and internal pressure lead to internal restraints in the material, which result in local stresses (eigenstresses) in the material after deformation compatibility. The damage of the un-

restrained specimens depends on the magnitude and distribution of the eigenstresses. The steep gradient of internal pressure along the diffusion direction led to the crack localization.

**PART 3: NUMERICAL
INVESTIGATIONS COMPARED WITH
EXPERIMENTAL ANALYSES**

5

EXPERIMENTAL AND NUMERICAL STUDY ON MECHANICAL PROPERTIES OF CEMENT PASTE PIPE WITHOUT SULFATE EXPOSURE

The mechanical properties of cement paste pipes after 90-day curing were investigated experimentally and numerically in this chapter, which aims at offering the realistic mechanical properties of cement paste for the simulations in chapter 6. Two types of specimens were subjected to uniaxial tensile loading, which were unnotched and single notched specimens. After uniaxial tensile experiments of unnotched specimens, the Young's modulus and tensile strength of specimens were obtained. Then the uniaxial tensile experiments were also carried out on single notched specimens. The complete stress-strain responses with softening information were obtained. The crack initiation and propagation were also discussed.

Both of these two types of specimens subjected to uniaxial tensile loading were simulated by a 3D lattice model and compared with the experimental observations. The local mechanical properties of lattice elements were discussed. After tensile simulations of the unnotched specimen, the Young's modulus and tensile strength were obtained for lattice elements. Then, the softening behavior of lattice elements was achieved after tensile simulations of the single notched specimen. The experimental and simulated stress-strain responses and cracking process were compared with each other. It was found that the simulated results matched quite well with the experimental results.

5.1. INTRODUCTION

EXTERNAL sulfate attack may cause gradual but severe mechanical damage on cementitious materials. In order to be able to model the degradation, some essential mechanical properties of unexposed specimens are required, such as tensile strength, constitutive response and fracture energy. However, these parameters of the specimens used in this research cannot be found in the literature. The direct way to obtain these mechanical properties is to perform experiments. A uniaxial (direct) tension test is thought to be the most direct method of determining the mode I fracture properties of concrete [117]. In order to obtain a complete stress-strain curve for concrete in uniaxial tension, it is essential to eliminate occurrence of sudden failure closed to the peak stress [118, 119]. One of the methods to address this issue is introducing a single notch on the specimen [120].

The uniaxial tensile test of cement paste specimens is rarely studied in the literature. Toutanji et al. [121] tested the cylindrical specimens with a diameter of 16 mm and a length of 120 mm in uniaxial tension. The tensile strength of 8.8 MPa and 9.8 MPa were obtained for the cement paste specimens with a water/cement ratio of 0.31 and 0.28, respectively. However, the complete stress-strain curve for cement paste specimens with a water/cement ratio of 0.40 cannot be found in the literature, which needs to be used in this research.

In this chapter, firstly, the uniaxial tensile test were carried out on unnotched and single notched specimens. Young's modulus and tensile strength of unnotched specimens and the complete stress-strain curve of single notched specimens were obtained. Afterwards, a 3D lattice model was constructed to simulate the two types of specimens subjected to uniaxial tensile loading. The Young's modulus and tensile strength of lattice elements were obtained after tensile simulations of the unnotched specimen. Then the tensile simulations of the single notched specimen were also carried out, through which the softening behavior of lattice elements was achieved. Finally, the experimental and simulated stress-strain responses and cracking process were compared with each other.

5.2. MATERIALS AND METHODS

5.2.1. MATERIALS AND SPECIMENS

AN ordinary Portland cement (CEM I 42,5 N) with a water/cement ratio of 0.40 was used in this study. PVC moulds with stainless steel rods in the center were fabricated in order to produce the cement paste pipes with a wall thickness of 2.5 mm (outer diameter 30 mm, inner diameter 25 mm), as described in section 2.2.1. After 60-day curing in saturated limewater, the cement paste pipes were cut and polished at both ends to ensure that they were parallel and that the length was 35 mm. Then the prepared specimens were put back to the saturated limewater.

Two types of specimens were tested in this chapter, which were the unnotched cement paste pipes (Fig. 5.1a) and single notched cement paste pipes (Fig. 5.1b). Single notched specimens were chosen in order to make it possible for measuring the post-peak stress-strain curve of the specimens during experiments, which can trigger crack growth from a known location [120]. Previous experiments showed that crack nucleation and growth happens at the notch due to stress concentration [122]. A notch with a depth

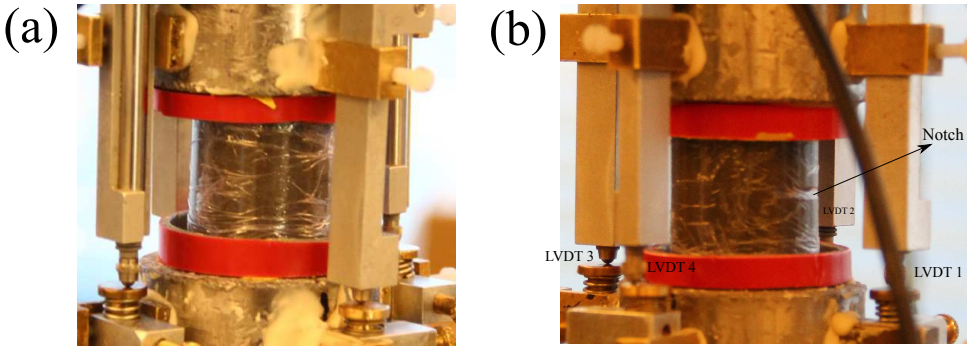


Figure 5.1: Setup of uniaxial tensile tests. (a) An unnotched cement paste pipe and (b) a single notched cement paste pipe.

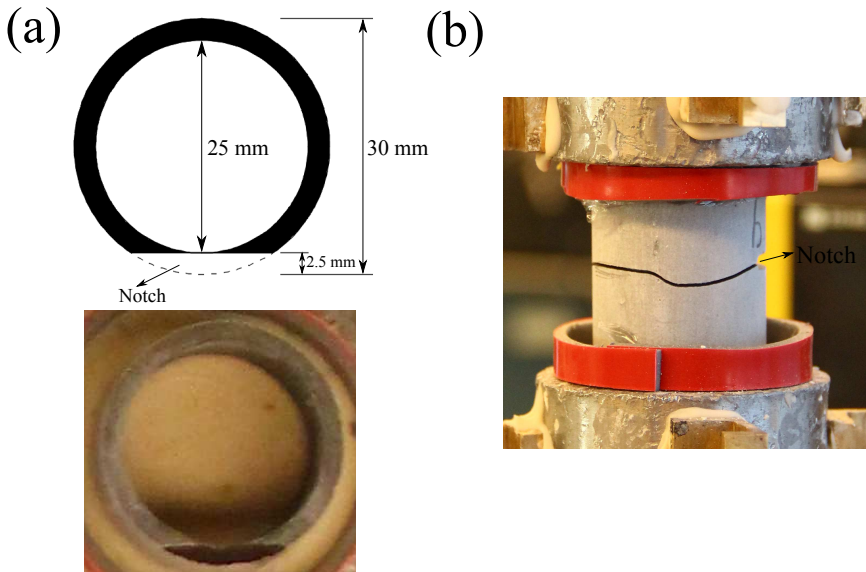


Figure 5.2: Uniaxial tensile test of single notched cement paste pipes (Fig. 5.1b). (a) Geometric size of the notch and (b) cracked specimen.

of 2.5 mm and a width of 2.25 mm was sawn at one side of the specimen at half-height (Fig. 5.2). After that, the prepared specimens were put back to the saturated limewater.

After 90-day curing in saturated limewater, all specimens were taken out of limewater for uniaxial tensile tests. In order to prevent drying cracks, the specimens were wrapped with plastic foil during the entire test procedure (Fig. 5.1). In addition, a sponge, which was saturated with water, was also put inside the hollow part of the specimens to minimize drying. The plastic foil was removed when the test was finished, as shown in Fig. 5.2b.

5.2.2. UNIAXIAL TENSILE TEST

Uniaxial tensile tests were performed in an Instron 8872 servo-hydraulic system. The specimens were glued between steel platens of the testing machine and loaded in deformation control. For the unnotched cement paste pipes (Fig. 5.1a), the tests were controlled by the average value of the four linear variable differential transducers (LVDTs) at a constant loading speed of $0.2 \mu\text{m}/\text{sec}$.

For the single notched cement paste pipes (Fig. 5.1b), firstly the tests were controlled by LVDT 1 which was located at the side of the notch. The rate of deformation was $0.02 \mu\text{m}/\text{sec}$. Afterwards, when the stress-strain curve passed the peak and the applied tensile stress dropped to around 1.3 MPa, the tests were controlled by the average value of the four LVDTs.

5.2.3. LATTICE FRACTURE MODEL

Fracture processes of cementitious materials can be studied with the Delft lattice model [123]. In this model, material is discretized as a network of beam elements which can transfer forces. The fracture process is simulated by the removal of lattice elements step by step. At every analysis step, a prescribed displacement is imposed on the lattice structure to find one critical element that has the highest stress/strength ratio, and then removing it from the system or changing it to have a weaker mechanical property. The basic removal procedure is to remove one element at one lattice analysis step. In the case of implementing local softening behavior, the strength and stiffness of each element are decreased step by step. The analysis procedure is repeated until a pre-determined failure criterion is achieved, such as a certain value of the displacement. The lattice element can fail only in tension. This method can simulate crack propagation, and thus, predict the global stress-strain response [124]. Details about the complete computational procedure and the equations of the model are available in the literature [125].

Two types of uniaxial tensile tests were simulated on the specimens, which were corresponding to the experiments. The first type is the uniaxial tensile simulation of the unnotched cement paste pipe, as shown in Fig. 5.3a. The wall thickness of the pipe is 2.5 mm (outer diameter 30 mm, inner diameter 25 mm) and the length is 35 mm, which are same as the experiment (Fig. 5.1a).

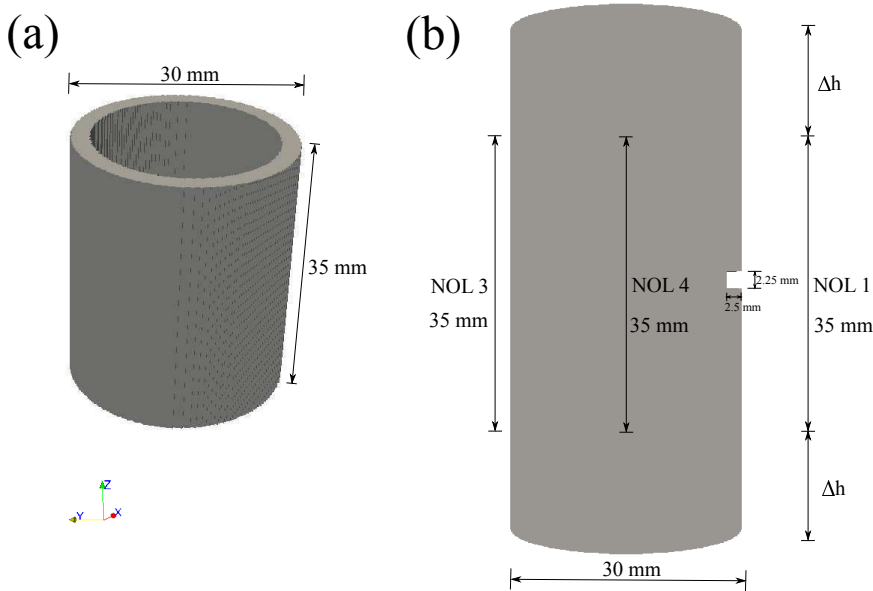


Figure 5.3: Cell-based images of the structure of cement paste pipes for uniaxial tensile simulations. (a) Un-notched pipe and (b) single notched pipe (NOL represents numerical output location, considering LVDT used in Fig. 5.1b).

The second type is the uniaxial tensile simulation of the single notched cement paste pipe (Fig. 5.3b). During the experiments, due to the rotations that happened at the boundaries which were not infinitely stiff, the deformations of the four LVDTs were different. In order to take the rotations of the boundaries into account in the simulations, it was chosen to increase the height of the specimen. As shown in Fig. 5.3b, “ Δh ” represents the increased height. Four locations were chosen at the simulated structure, which were same as the locations of LVDTs in the experiments. For each location, two nodes were chosen, which were along the same vertical line. The distance between the two nodes is expressed as NOL. The original NOL is 35 mm, which is same as the LVDTs in the experiments (Fig. 5.1b). During the simulations, the change of NOL was recorded. A single notch with the depth of 2.5 mm and the thickness of 2.25 mm was also applied at the half-height of the simulated pipe, which was the same as the experimental setup. NOL 1 was located at the side of the notch.

The specimens were meshed at the resolution of 0.25 mm/cell, and a 3D quadrangular lattice network was constructed. A sub-cell was created within each cell sharing the same center, and the length ratio of the sub-cell to the cell is defined as randomness. The value of randomness is always between 0 and 1 [126]. More details about the influence of randomness can be found in [127]. A lattice node was positioned within the cell randomly and neighbor nodes were connected by a lattice element. During the 3D mesh generation process, the randomness of the lattice system was set to 0.5 for all the non-boundary cells and 0 for all the boundary cells. The randomness of 0.5 can introduce irregular geometry of the mesh. The cross-section of the lattice element was assumed to

be circular and was chosen such that the stiffness of the system is equal to the stiffness of the local element. For all the simulations in this section, all the lattice elements were assumed to have the same local mechanical properties.

5.3. EXPERIMENTAL RESULTS AND DISCUSSION

5.3.1. UNNOTCHED CEMENT PASTE PIPES

THREE unnotched cement paste pipes (specimen 1, 2 and 3) were tested in uniaxial tension, as shown in Fig. 5.1a. The Young’s modulus of 20.3 GPa and tensile strength of 5.7 MPa were found, as presented in Table 5.1. However, the tests stopped immediately after the peak stress of the stress-strain curve. The tests were controlled by the average deformation of the four LVDTs. Before the peak stress, the average deformation kept increasing. However, after the peak stress, the average deformation began to decrease. Increasing deformation is needed for the continuation of the tests. Therefore, a large deformation occurred immediately after the peak stress which led to a sudden damage of the specimen and the stop of the test. The reasons are discussed detailedly in section 5.3.3. In this case, the post-peak stress-strain curve cannot be measured if the unnotched specimens were chosen.

Table 5.1: Experimental results of global mechanical properties of unnotched cement paste pipes (Fig. 5.1a)

Specimen number	Young’s modulus (GPa)	Tensile strength (MPa)
Specimen 1	20.9	5.6
Specimen 2	20.3	5.7
Specimen 3	19.7	5.7
Average	20.3	5.7

5.3.2. SINGLE NOTCHED CEMENT PASTE PIPES

Two single notched cement paste pipes (specimen 4 and 5) were tested in uniaxial tension, as shown in Fig. 5.1b. The stress-strain responses with post-peak softening information are presented in Fig. 5.4. The strain in the curves was calculated as the deformation measured by the LVDT divided by the original length of the specimen (35 mm). As can be found in Fig. 5.4a, after reaching peak stress, LVDT 1 and LVDT 2 kept increasing, on the contrast, LVDT 3 and LVDT 4 started to decrease, which was due to the localization of cracking. The applied tensile load was along vertical direction, therefore the main crack started from the notch tip and developed along horizontal direction. After reaching peak stress, the tests changed to the stage of unloading. Because of the decrease of applied tensile load, the deformation of uncracked part also decreased, which led to the snap back phenomenon (LVDT 3 and LVDT 4). For the cracked part, even though the unloading resulted in deformation decrease, However, the crack opening can lead to deformation increase. Therefore the deformation after peak stress could possibly continue increasing. The main crack started from the notch tip, which was located either between LVDT 1 and LVDT 2 or between LVDT 1 and LVDT 4. In Fig. 5.4a, LVDT 1 and LVDT 2

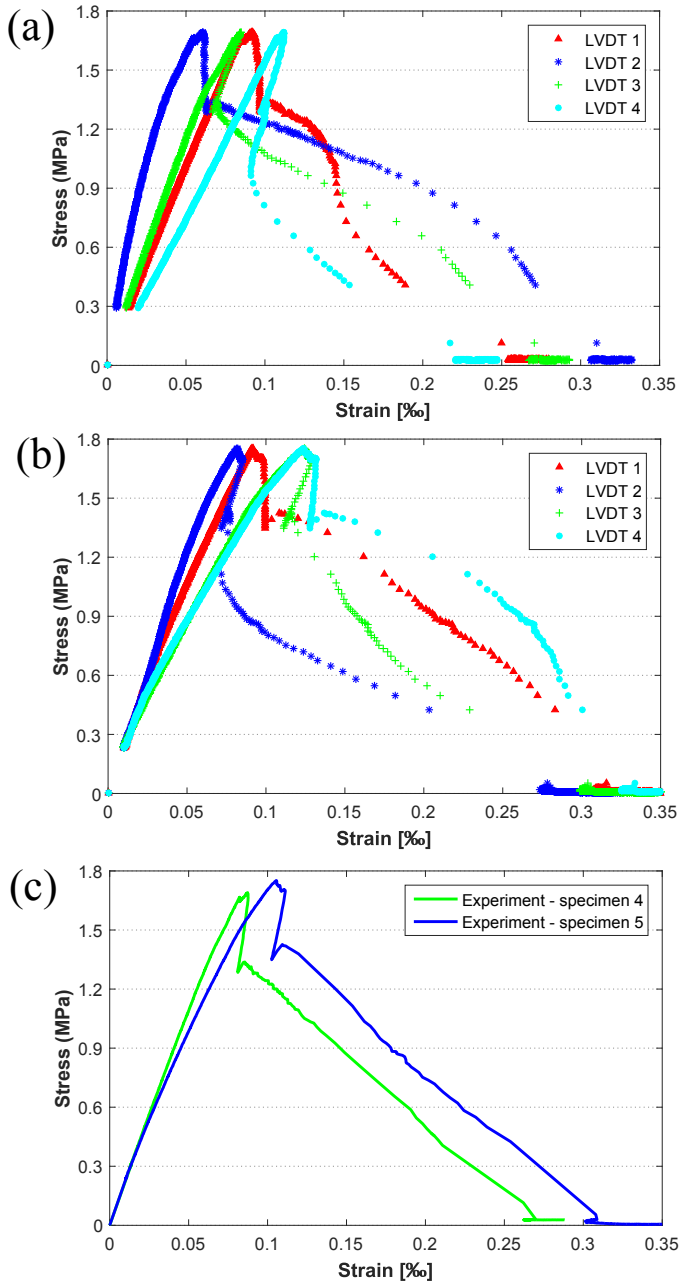


Figure 5.4: Experimental stress-strain responses of single notched cement paste pipes (Fig. 5.1b) subjected to uniaxial tensile loading along vertical direction. (a) Specimen 4, (b) specimen 5 and (c) comparison between specimen 4 and specimen 5 (strain is the average value of the four LVDTs).

continued increasing after peak stress, therefore the main crack started at the notch tip between LVDT 1 and LVDT 2. After peak stress, both of LVDT 3 and LVDT 4 decreased firstly and then increased. LVDT 3 increased earlier. Therefore, the main crack continued to develop and passed the location of LVDT 3. After that, another main crack started at the other notch tip between LVDT 1 and LVDT 4. Since these two main cracks were at two different planes, an inclined plane made these two cracks connect and the whole specimen was fractured finally, as presented in Fig. 5.2b.

The crack propagation process can also be found through Fig. 5.4b. After peak stress, LVDT 1 and LVDT 4 kept increasing. LVDT 2 and LVDT 3 decreased firstly and then increased, while LVDT 3 increased earlier. Therefore, one main crack firstly started at the notch tip between LVDT 1 and LVDT 4. The crack continued to pass the location of LVDT 4 and then LVDT 3. After that, another main crack started at the other notch tip between LVDT 1 and LVDT 2. Finally, these two cracks met and the whole specimen was fractured.

5.3.3. DISCUSSION

The experimental results have shown that it was possible to obtain the softening behavior of the cement paste pipes when a notch was introduced.

At the unloading stage, the deformation of uncracked material decreased with the load decreasing. On the other hand, the crack opening can lead to the increase of deformation. For the notched specimens, the main crack started from the notch (section 5.3.2). Therefore, the tests were controlled by LVDT 1, which was located at the side of the notch. During the tensile tests, LVDT 1 kept increasing until the end, even though the other three LVDTs may decrease after peak stress, as can be found in Fig. 5.4a and b. The stress-strain response, for which the average of the four LVDTs is used to plot the strain, is shown in Fig. 5.4c. It can be seen that the average of the four LVDTs began to decrease after peak stress. For the deformation controlled tensile tests, the increase of deformation is needed for the test continuation. Therefore, when the tests are controlled by the average of the four LVDTs, the post-peak stress-strain curve can still not be obtained even for the single notched specimens.

For the unnotched specimens in section 5.3.1, the location for crack nucleation and growth is unknown. Therefore, the tests were controlled by the average of the four LVDTs, which started to decrease after peak stress. As a result, the post-peak stress-strain curve cannot be obtained during the experiments.

5.4. NUMERICAL SIMULATION RESULTS AND DISCUSSION

5.4.1. UNNOTCHED CEMENT PASTE PIPE

As mentioned in section 5.3.1, the Young's modulus of 20.3 GPa and tensile strength of 5.7 MPa were found experimentally for the unnotched specimens. For the local mechanical properties of the lattice elements, a value of 20.3 GPa for the Young's modulus was chosen. However, the local tensile strength needs to be determined through simulations.

A linear elastic behavior for the lattice elements was assumed. The external tensile loading was imposed on the top and bottom surfaces in the z-direction (Fig. 5.3a). Several uniaxial tensile simulations were carried out. Each time, the local tensile strength of

lattice elements was assumed. Then the global tensile strength of specimen was simulated. The simulated results are listed in Table 5.2. It was found that the global tensile strength of 5.7 MPa could be achieved when the local tensile strength of 6.8 MPa was applied on the lattice elements.

In that way, the Young's modulus and tensile strength of lattice elements were obtained based on the experimental results, which are presented as point 1 in Fig. 5.6 and Table 5.5.

Table 5.2: Simulated results of global tensile strength of the unnotched cement paste pipe (Fig. 5.3a)

Simulation number	Assumed local tensile strength of lattice elements (MPa)	Simulated global tensile strength (MPa)
Simulation 1	5.7	4.8
Simulation 2	6.5	5.5
Simulation 3	6.9	5.8
Simulation 4	6.8	5.7

5.4.2. SINGLE NOTCHED CEMENT PASTE PIPE

This section discusses the simulations of the single notched specimen (Fig. 5.3b). The external tensile loading was imposed on the top and bottom surfaces in the z-direction. The linear elastic part of lattice elements was obtained in section 5.4.1 (point 1 in Fig. 5.6). In this section, the softening part of lattice elements is discussed.

INFLUENCE OF INCREASED HEIGHT OF SIMULATED STRUCTURE

As discussed in section 5.2.3, in order to simulate the situation in experiments, the length of the simulated pipe was chosen to be larger. The increased height is expressed as Δh (Fig. 5.3b). The Young's modulus and tensile strength of lattice elements were chosen as 20.3 GPa and 6.8 MPa, respectively, as shown in Fig. 5.6a.

The simulated stress-strain responses of specimens with different increased height (Δh) are shown in Fig. 5.5. As can be found in Fig. 5.5a, when the height of the simulated pipe was same as the experiments, the responses of the four NOLs were also same. When the increased height (Δh) was above 0, the responses of the four NOLs started to be different. A larger increased height (Δh) can lead to a greater difference among the four NOLs. In experiments, the strain of LVDT 1 at peak load was close to 0.1 ‰ (Fig. 5.4a and b). In Fig. 5.5d, the strain of NOL 1 at peak load was also close to 0.1 ‰. Therefore, $\Delta h=15$ was chosen for the following simulations.

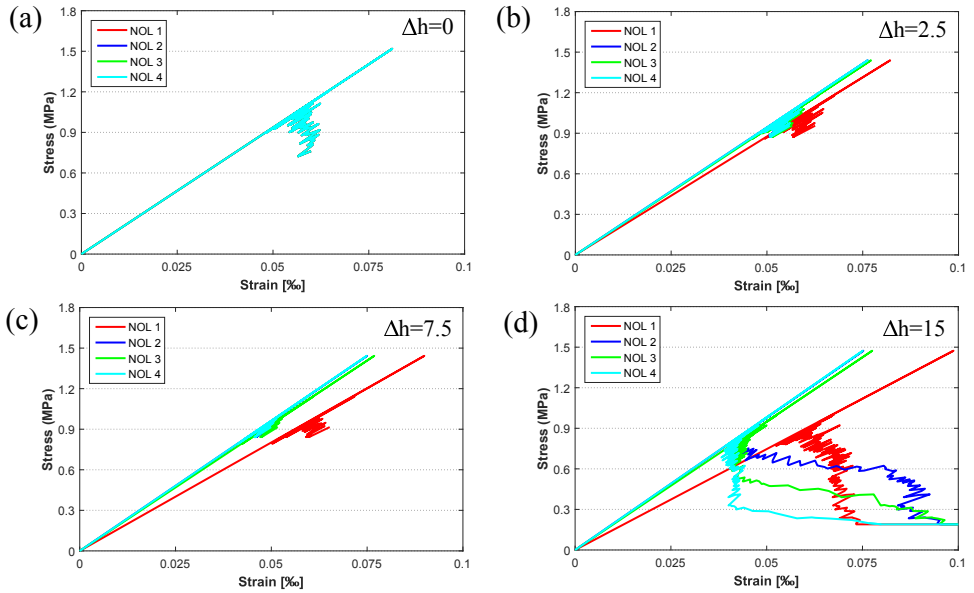


Figure 5.5: Influence of increased height (Δh), which is corresponding to Fig. 5.3b. Simulated stress-strain responses of the single notched cement paste pipe (Fig. 5.3b) subjected to uniaxial tensile loading along vertical direction. Lattice elements behave as linear elastic (Fig. 5.6a). (a) $\Delta h=0$, (b) $\Delta h=2.5$, (c) $\Delta h=7.5$ and (d) $\Delta h=15$

INFLUENCE OF LOCAL MECHANICAL PROPERTIES OF LATTICE ELEMENTS

Five simulations were carried out. The linear elastic behavior was used for the lattice elements in “simulation linear 1”. For the other four simulations, the softening behavior was applied on the lattice elements. The assumed local mechanical properties were shown in Fig. 5.6. Point 1 in Fig. 5.6a, b and c are same, which was obtained in section 5.4.1. The other points were assumed, which formed a multi-linear curve for each case. One more point was added on “simulation multi-linear 4” to form “simulation multi-linear 5”.

The simulated stress-strain responses of the specimen are presented in Fig. 5.7. As shown in Fig. 5.7a, it is found that the softening behavior of the specimen is not obtained in the case of lattice elements with linear elastic behavior. A softening behavior of the specimen closer to the experimental result can be obtained by changing the softening behavior of lattice elements, as presented in Fig. 5.7b, c, d and e.

Furthermore, the comparisons between experimental and simulated stress-strain responses of the specimen are summarized in Fig. 5.8. The strain in the curves stands for average strain of the four LVDTs or NOLs. The corresponding local mechanical properties applied on lattice elements are shown in Fig. 5.6. The softening part of the simulated curves is quite different among the simulations (Fig. 5.8f). Fig. 5.8e shows the best simulated results compared with the other four simulations, and matches very well with the experimental curves. Therefore, Fig. 5.6c is suggested to be the local mechanical properties of lattice elements.

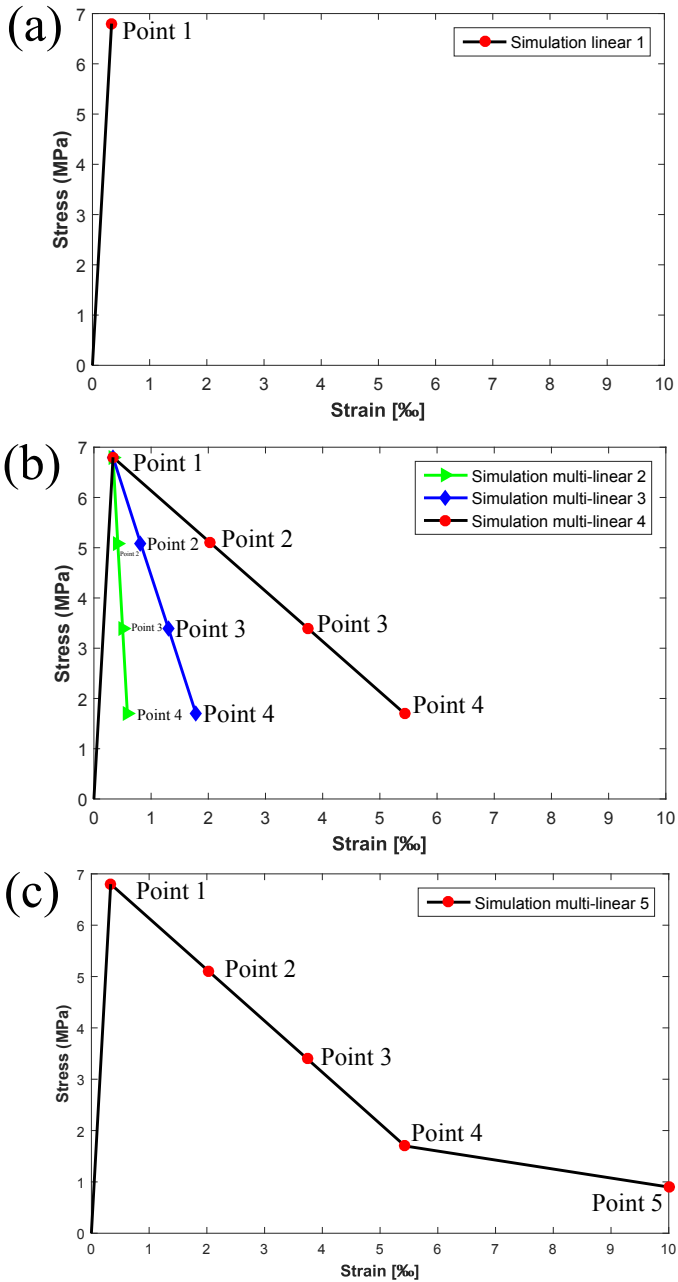


Figure 5.6: Assumed local mechanical properties of lattice elements. (a) Simulation linear 1 (linear elastic behavior), (b) simulation multi-linear 2, 3, 4 (multi-linear behavior) and (c) simulation multi-linear 5 (multi-linear behavior).

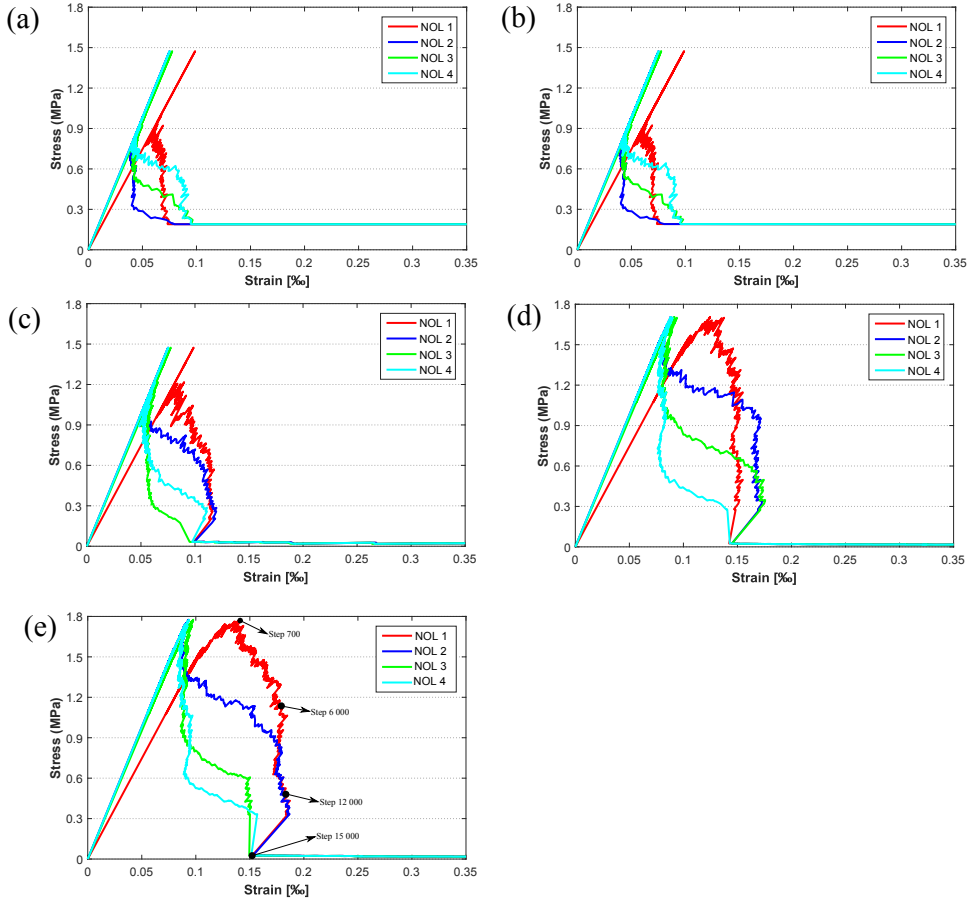


Figure 5.7: Simulated stress-strain responses of the single notched cement paste pipe (Fig. 5.3b, $\Delta h=15$ mm) subjected to uniaxial tensile loading along vertical direction. The local mechanical properties of lattice elements are referred to Fig. 5.6. (a) Simulation linear 1, (b) simulation multi-linear 2, (c) simulation multi-linear 3, (d) simulation multi-linear 4 and (e) simulation multi-linear 5.

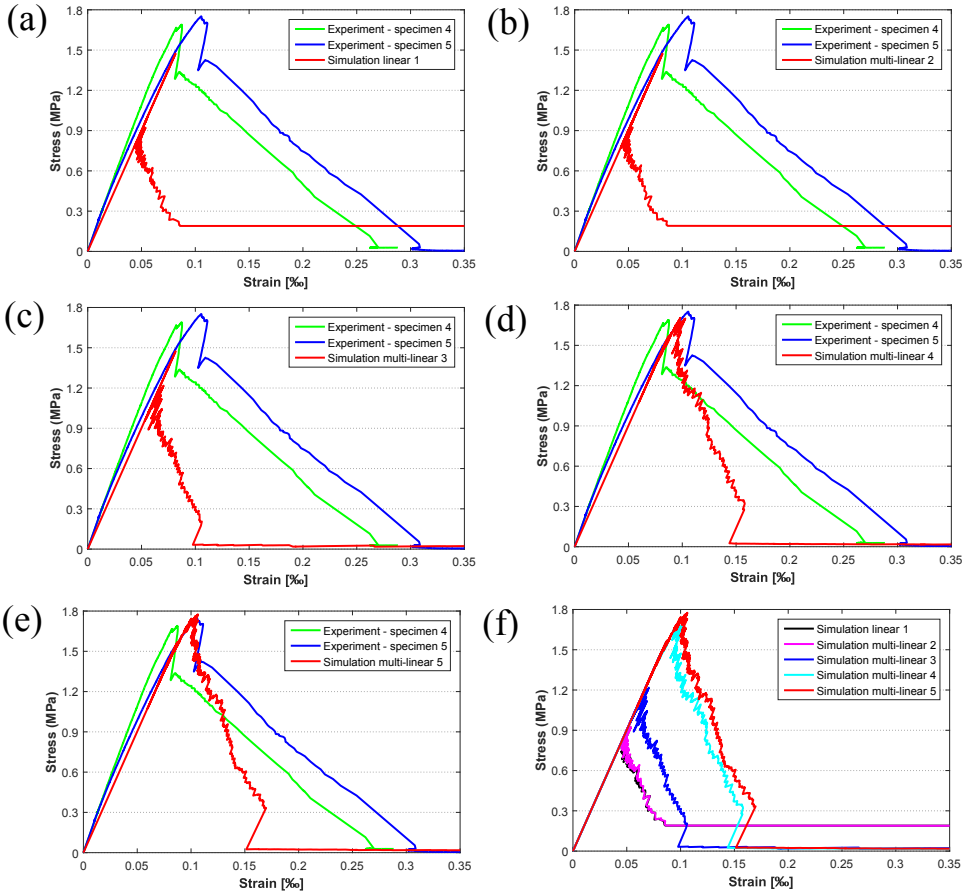


Figure 5.8: Results of the single notched cement paste pipe (experiment: Fig. 5.1b, simulation: Fig. 5.3b, $\Delta h=15$ mm) subjected to uniaxial tensile loading along vertical direction. Strain is the average value of the four LVDTs or NOLS. Comparisons between experimental and simulated stress-strain responses (a) simulation linear 1, (b) simulation multi-linear 2, (c) simulation multi-linear 3, (d) simulation multi-linear 4, (e) simulation multi-linear 5 and (f) comparisons among simulated stress-strain responses.

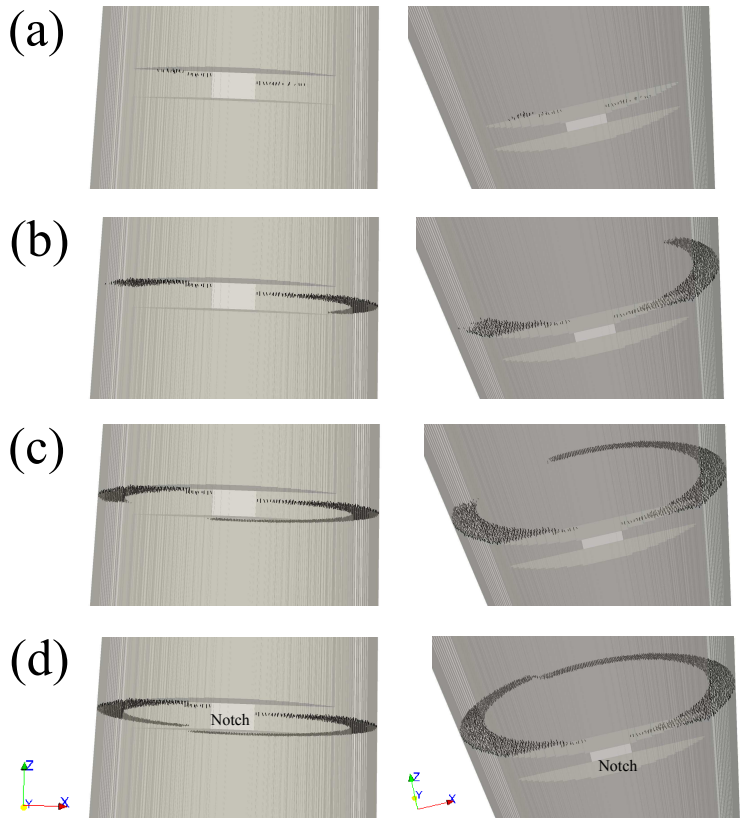


Figure 5.9: Simulated crack patterns of the single notched cement paste pipe subjected to uniaxial tensile loading along vertical direction at (a) step 700, (b) step 6 000, (c) step 12 000 and (d) step 15 000 (black-damaged element), corresponding to Fig. 5.7e. Fig. 5.6c was used as the local mechanical properties of lattice elements.

The fracture energy of experiments and lattice elements with assumed local mechanical properties is listed in Table 5.3, which was calculated as the length in the loading direction multiplied by the area below the stress-strain curve (Fig 5.4c and Fig. 5.6). The length of 35 mm was used for calculations in experiments, and the length of 0.25 mm was assumed for calculations in lattice elements. It can be found that the fracture energy of "simulation multi-linear 5" is similar as the fracture energy of experiments. Therefore, if the fracture energy of lattice elements with assumed local mechanical properties is close to the fracture energy of experiments, the simulated stress-strain responses of the specimen is also close to the curves measured by experiments.

Table 5.3: Calculations of fracture energy

		Fracture energy (J/m^2)
Lattice elements with assumed local mechanical properties, corresponding to Fig. 5.6	Simulation linear 1	0.3
	Simulation multi-linear 2	0.6
	Simulation multi-linear 3	1.8
	Simulation multi-linear 4	5.7
	Simulation multi-linear 5	7.2
Experimental results, corresponding to Fig. 5.4c	Experiment - specimen 4	7.1
	Experiment - specimen 5	8.9

The simulated cracking process caused by uniaxial tensile loading are shown in Fig. 5.9. Fig. 5.6c was used as the local mechanical properties of lattice elements. The corresponding stress-strain response at certain analysis step is marked in Fig. 5.7e. As presented in Fig. 5.9, it is found that the crack firstly started at the notch between NOL 1 and NOL 2. Then another crack started at the notch between NOL 1 and NOL 4. Finally, these two cracks met at the location between NOL 3 and NOL 4. As can be seen, these two cracks were at two different planes, therefore, an inclined plane made these two cracks connect. As shown in Fig. 5.7e, after peak stress, NOL 1 continued to increase, however, the other three NOLs started to decrease. Afterwards, NOL 2 firstly started to increase, following with NOL 3 and then NOL 4. That also indicated the crack firstly started at the notch between NOL 1 and NOL 2. It can be concluded that the simulated cracking process is similar to the experimental observation.

5.4.3. DISCUSSION

The linear elastic part of lattice elements (Fig. 5.6a) was obtained after simulations of the unnotched specimen. Afterwards, based on simulations of the single notched specimen, the softening part of lattice elements was suggested, as shown in Fig. 5.6c. When Fig. 5.6c was used for lattice elements for the unnotched specimen, the simulated tensile strength of the specimen was found to be 6 MPa, which was just a slight increase of the tensile strength, as listed in Table 5.4. Therefore, Fig. 5.6c is chosen as the final local mechanical properties of lattice elements. The details of Fig. 5.6c are listed in Table 5.5.

Table 5.4: Simulated results of mechanical properties of the unnotched cement paste pipe (Fig. 5.3a)

Assumed local mechanical properties of lattice elements	Simulated global Young's modulus (GPa)	Simulated global tensile strength (MPa)
Lattice elements behave as Fig. 5.6a	20.3	5.7
Lattice elements behave as Fig. 5.6c	20.3	6.0

Table 5.5: Suggested local mechanical properties of the lattice elements, corresponding to Fig. 5.6c

Point	Young's modulus (MPa)	Tensile strength (MPa)
1	20 332	6.8
2	2 507	5.1
3	910	3.4
4	313	1.7
5	90	0.9

5.5. SUMMARY AND CONCLUSIONS

IN this chapter, the cement paste pipes with a wall thickness of 2.5 mm and a water/cement ratio of 0.40 were used. The uniaxial tensile tests were carried out on the specimens after 90-day limewater curing. The mechanical properties of the unnotched and single notched specimens were investigated experimentally and numerically. The main results are summarized as below.

- A uniaxial tensile loading was applied on the unnotched specimens along longitudinal direction. The Young's modulus of 20.3 GPa and tensile strength of 5.7 MPa were found. However, the softening behavior of the specimen cannot be obtained.
- The specimens with a notch were also subjected to uniaxial tensile loading. A single notch was sawn at one side of the specimens at half-height, which can trigger crack growth from a known location. Therefore, the complete stress-strain responses with softening information were obtained. Based on the stress-strain responses of the four LVDTs and experimental observations, it was found that one main crack started from notch tip and developed along the horizontal direction. Then another main crack also started from the other notch tip. Finally, these two cracks met and connected, which resulted in the fracture of the specimens.
- A 3D lattice model with a resolution of 0.25 mm/cell was constructed to simulate the stress-strain responses measured by uniaxial tensile experiments. A single notch was also applied at the half-height of the simulated pipe, which was the same as the experimental setup. Both of the specimens without and with a notch were simulated. The local mechanical properties of lattice elements were

discussed. After the tensile simulations of the unnotched specimen, the Young's modulus of 20.3 GPa and tensile strength of 6.8 MPa were obtained for lattice elements.

- The softening behavior of lattice elements was studied by the tensile simulations of the single notched specimen. The local mechanical properties which behave as a multi-linear curve were achieved for lattice elements. The simulated stress-strain responses of the four NOLs and cracking process were compared with the experimental observations. It was found that the simulated results matched quite well with the experimental results.
- The obtained local mechanical properties of lattice elements can be used for other simulations with the same material (cement paste with a water/cement ratio of 0.40, CEM I 42,5 N, 90-day limewater curing) and the same mesh resolution (0.25 mm/cell). In our research, the same specimens were exposed to sodium sulfate solutions. The expansion and degradation of the specimens due to external sulfate attack were simulated in chapter 6. The work in this chapter provides the realistic mechanical properties of the lattice elements for the simulations in chapter 6.

6

MESOSCALE MODELING OF EXPANSION AND DAMAGE OF CEMENT PASTE PIPE IN STRONG SODIUM SULFATE SOLUTION

This chapter presents a numerical study on expansion and degradation processes of the specimen immersed in strong sulfate solution (30 g/L) under high-restraint condition (7 mm), which were investigated experimentally in chapter 2 and 3. A 3D lattice model with a mesh resolution of 0.25 mm/cell is constructed. The local mechanical properties of cement paste lattice elements were obtained in chapter 5. The magnitude of local expansive pressure is discussed in this chapter.

6.1. INTRODUCTION

EXTERNAL sulfate attack in a saturated situation is a complex issue in which ionic transport, expansive reactions and mechanical damage interact with each other. These phenomena may be accompanied by significant macroscopic expansion and severe mechanical damage. Crystallization pressure theory has often been referred to as the most likely mechanism to explain the origin of the expansion. According to the crystallization pressure theory [53, 55, 56], the driving force is the supersaturation of pore solution. Then, the crystal growth in the confined space leads to the expansive pressure on the pore walls. The magnitude of the expansive pressure inside nanopores can be estimated based on crystallization pressure theory. However, an experimental verification is still missing since direct measurement of the expansive pressure on nanopore walls is highly challenging. In addition, considering the big differences in scale, the magnitude of expansive pressure at nanoscale is almost impossible to be used for the simulations on concrete structure. Therefore, this research proposes determining the local expansive pressure indirectly through measuring the expansion and generated stress of larger scale specimens in experiments and discussing that in simulations. The expansion and degradation of the specimens exposed to sulfate solutions were studied in the previous chapters. This chapter focuses on the simulations.

In this chapter, the specimen immersed in strong sodium sulfate solution (30 g/L) under high-restraint condition (7 mm) is investigated numerically. A 3D lattice model is constructed to simulate the expansion and degradation observed in experiments. Firstly, the expansion behaviors after 21-day, 70-day, 105-day, 133-day and 189-day exposure are simulated. Next, an equation with a simplistic consideration based on crystallization pressure theory and measured sulfur distribution is proposed, which attempts to find a simple way to estimate local expansive pressure at larger scale. Finally, one simulation is carried out to study the cracking process of the specimen.

6.2. NUMERICAL DETAILS AND METHODS

6.2.1. LATTICE FRACTURE MODEL

FRACTURE processes of cementitious materials can be studied with Delft lattice model [123]. In this model, material is discretized as a network of beam elements which can transfer forces. The fracture process is simulated by the removal of lattice elements step by step. Although mostly used for modeling fracture of materials under external loading or deformation as described in chapter 5, Delft lattice model has also been used for simulating damage of materials due to internal loading, such as autogenous shrinkage [128], frost salt scaling [129], reinforcement corrosion [130], drying shrinkage [131] and freeze-thaw damage [132].

In this chapter, the attention is focused on the simulation of development of eigenstresses and progressive damage caused by external sulfate attack (ESA). The loading that is applied on the mesh is the local expansive pressure of local material (each element in the mesh) based on sulfur distribution at different immersion time, which is the pressure under unrestrained condition. However, the expansion of each element is restrained by the surrounding connected elements. Therefore, after applying the local expansive pressures on the elements in the mesh, the nodal displacements and the

corresponding internal forces are redistributed to satisfy the equilibrium relations [124]. After the redistribution, if the tensile stress in one of the elements exceeds the tensile strength of the material, this element is removed from the lattice system (assumption of linear elastic behavior) or changed to have a weaker mechanical property (assumption of multi-linear behavior). Stress in the removed element is released and other elements connected to the broken element are less restrained. Then the deformations of all the nodes and the stresses in all the surviving elements are recalculated and compared again with their strength, which results in the next element to break.

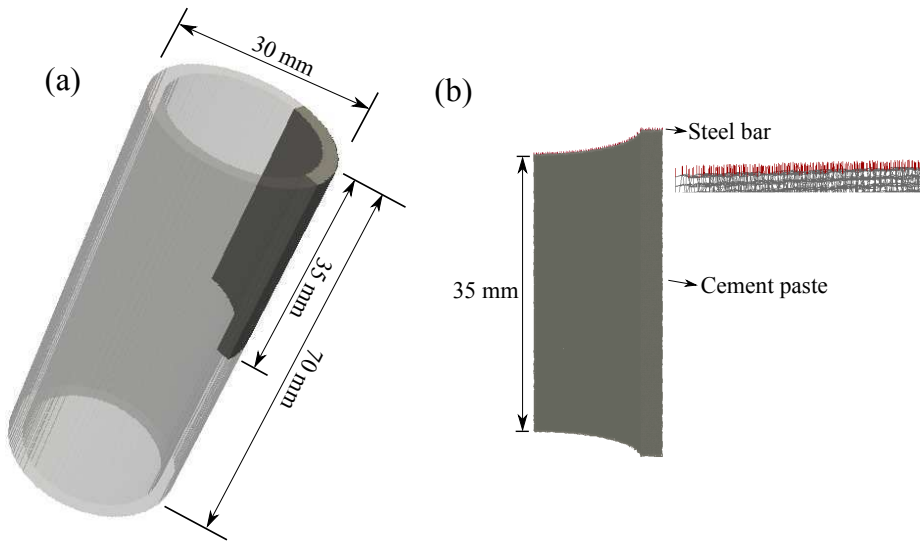


Figure 6.1: The structure of cement paste pipes for simulations. (a) Cell-based image of 1/8 pipe and (b) lattice mesh used in the simulations.

Due to large computational expense, only a quarter of the half pipe was simulated in this chapter based on geometric symmetry, as shown in Fig. 6.1a. The wall thickness of the pipe was 2.5 mm (outer diameter 30 mm, inner diameter 25 mm). The length of the simulated structure was 35 mm. The structure was meshed at the resolution of 0.25 mm/cell, and a 3D quadrangular lattice network was constructed. The randomness of all the cells was set to 0.5, which resulted in the irregular geometry of the lattice mesh. The cross-section of the lattice element was assumed to be circular and was chosen such that the stiffness of the system is equal to the stiffness of the local element. The lattice system of cement paste was displayed as gray in Fig. 6.1b. All the cement paste lattice elements were assumed to have the same local mechanical properties, which were discussed and obtained in chapter 5 through uniaxial tensile experiments and simulations of same specimen with same mesh resolution. In this chapter, the local mechanical properties applied on cement paste lattice elements are listed in Table 6.1.

The cement paste pipe under high-restraint condition (7 mm) was simulated in this chapter. The restrained condition by 7 mm steel bar was implemented by adding a layer of vertical lattice elements, which are displayed in red in Fig. 6.1b. Based on the lattice

Table 6.1: Local mechanical properties applied on lattice elements

Type of lattice elements	Point	Young's modulus (MPa)	Tensile strength (MPa)
Cement paste	1	20 332	6.8
	2	2 507	5.1
Steel bar	1	193 000	600
	2	193 000	600

mesh of cement paste (gray in Fig. 6.1b), all the nodes at top boundary were copied and shifted up vertically with a distance of 0.25 mm to create a layer of new nodes. Then the newly created nodes were connected with the original top boundary nodes to generate the needed vertical elements. The cross-section of steel bar lattice elements was also assumed to be circular and was calculated as follows. A value was assumed for the expansion of the cement paste pipe. Next, the tensile force in the 7 mm steel bar in the experiment caused by the assumed expansion can be calculated. Similarly, the compressive force in the steel bar elements in the lattice mesh caused by the assumed expansion of the cement paste can also be calculated if the cross-section is known. For the same expansion, the two forces above should be equal. All the steel bar lattice elements were assumed to have the same local mechanical properties, which are listed in Table 6.1.

During the simulations, the vertical displacements of all the nodes at bottom and top surface were prescribed to be 0. Also, the horizontal displacements (x-direction and y-direction) of all the nodes at the second layer of top part (nodes at the bottom of the red elements in Fig. 6.1b) were prescribed to be 0. The local expansive pressure was only applied on the gray elements (cement paste). The expansion of gray elements resulted in the compressive stress in the red elements (steel bar) when the above boundary condition was applied, therefore, the cement paste was restrained by the steel bar. Larger diameter of steel bar lattice elements can lead to stronger restraint. The total reaction force along vertical direction at the top or bottom surface was defined as the generated force, which was used for the calculation of the generated stress. The restrained expansion was expressed as the length change of cement paste pipe along the vertical direction divided by the original length.

6.2.2. MODELING BASICS OF ESA MECHANISM

In this chapter, it is assumed that expansion is due to crystallization pressure developing inside the nanopores within the cement paste [10, 11, 38]. As discussed in chapter 1, the crystallization pressure σ_c is generally expressed as shown in Eq. 6.1.

$$\sigma_c = \frac{R_g T}{V_c} \ln \left(\frac{Q}{K} \right) \tag{6.1}$$

where σ_c represents the crystallization pressure exerted on the surrounding pore wall, R_g is the gas constant, T is the absolute temperature, V_c is the crystal molar volume, Q is the ion activity product and K is the equilibrium constant [54, 55].

The supersaturation of the pore solution with respect to ettringite ($C_6A\bar{S}_3H_{32}$) is

given below (Eq. 6.2) [11, 55].

$$\frac{Q_{Ettringite}}{K_{Ettringite}} = \frac{(C_{Ca^{2+}})^6 \cdot (C_{Al(OH)_4^-})^2 \cdot (C_{OH^-})^4 \cdot (C_{SO_4^{2-}})^3 \cdot (C_{H_2O})^{26}}{K_{Ettringite}} \quad (6.2)$$

If we assume that only the concentration of SO_4^{2-} changes from the equilibrium value for ettringite as a simplistic consideration [11], the crystallization pressure can be calculated as in Eq. 6.3.

$$\sigma_c = \frac{R_g T}{V_c} \ln\left(\frac{Q}{K}\right) = \frac{R_g T}{V_c} \ln\left(\frac{[C_{SO_4^{2-}}]_{new}}{[C_{SO_4^{2-}}]_{eq}}\right)^3 = \frac{3R_g T}{V_c} \ln\left(\frac{[C_{SO_4^{2-}}]_{new}}{[C_{SO_4^{2-}}]_{eq}}\right) \quad (6.3)$$

where $R_g=8.314 \text{ J/mol} \cdot \text{K}$, $T=293.15 \text{ K}$, $V_c=708.5 \text{ cm}^3/\text{mol}$ for ettringite [11].

$[C_{SO_4^{2-}}]_{new} / [C_{SO_4^{2-}}]_{eq}$ was simply assumed as $[C_{sulfur}]_{new} / [C_{sulfur}]_{eq}$. Then, the local expansive pressure can be simply assumed to be calculated by Eq. 6.4.

$$\sigma_c = \frac{3R_g T}{V_c} \ln\left(\frac{[C_{sulfur}]_{new}}{[C_{sulfur}]_{eq}}\right) \quad (6.4)$$

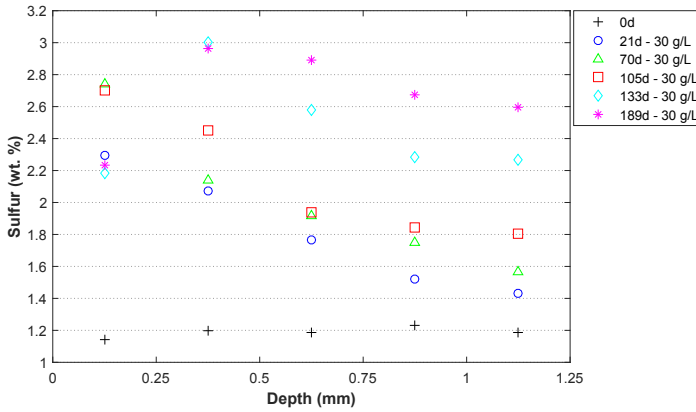


Figure 6.2: Sulfur profiles along diffusion direction after being exposed to 30 g/L SO_4^{2-} (half of wall thickness).

The sulfur profiles of specimens immersed in 30 g/L sodium sulfate solution at different exposure time can be found in section 3.4.1 (Fig. 3.10b). However, as discussed in chapter 4, the precipitation of gypsum also contributes to Fig. 3.10b, which can lead to a high sulfur content and possibly has a negligible contribution to the expansive pressure. It was assumed that the sulfur content above 3 wt% was mainly due to the gypsum precipitation. Therefore, in order to avoid overestimation, the new sulfur profiles were used in this chapter. Based on Fig. 3.10b, the sulfur content was assumed to be 3 wt% when it was above 3 wt%. Then the new sulfur profiles were obtained. In order to meet the same resolution as the lattice mesh (0.25 mm/cell), the new sulfur profiles were rewritten as shown in Fig. 6.2. Each point in Fig. 6.2 represents an average value of 0.25 mm depth of

the new sulfur profiles. $[C_{sulfur}]_{eq}$ was taken as the average value of sulfur content before sulfate exposure (0-day), which was 1.19 wt%. $[C_{sulfur}]_{new}$ was taken as the value shown in Fig. 6.2.

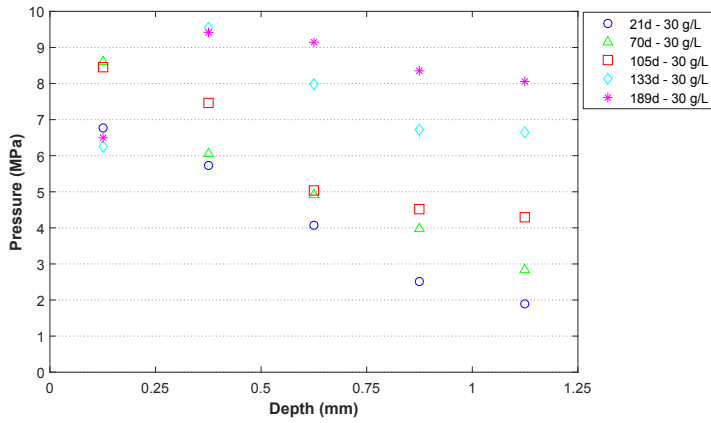


Figure 6.3: Initial estimation of the expansive pressure in lattice node along diffusion direction after being exposed to 30 g/L SO_4^{2-} (half of wall thickness), based on Fig. 6.2 and Eq. 6.4 ($m=1$ in Eq. 6.6).

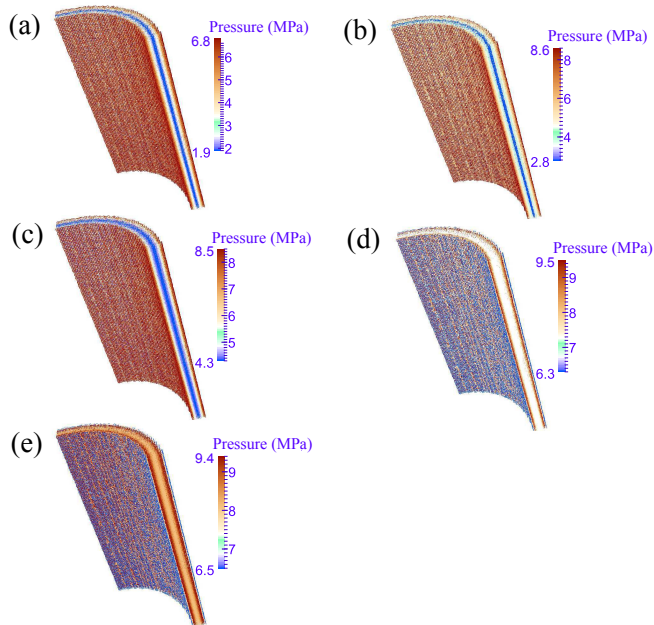


Figure 6.4: Initial estimation of the expansive pressure of lattice elements (based on Fig. 6.3), which was used as the input for the simulations at (a) 21-day, (b) 70-day, (c) 105-day, (d) 133-day and (e) 189-day exposure to 30 g/L SO_4^{2-} (whole of wall thickness).

Based on the obtained sulfur distribution (Fig. 6.2) and crystallization pressure theory (Eq. 6.4), the initial estimation of the local expansive pressure distribution along diffusion direction for half-wall thickness can be obtained, as plotted in Fig. 6.3. Each point in Fig. 6.3 stands for one value of expansive pressure applied on a cubic cell with a length of 0.25 mm, which is the pressure of one node at certain location in the lattice system.

In this chapter, all the nodes at same depth had the same value of expansive pressure. The irregular geometry of lattice mesh could lead to the heterogeneity of the expansive pressure at the same depth. The expansive pressure was only applied on the cement paste lattice elements, which was taken as the average value of the pressures in the connected two nodes. The pressures in nodes are shown in Fig. 6.3. Therefore, the initial estimation of the local expansive pressure applied on lattice elements can be obtained, as displayed in Fig. 6.4.

The input for the simulation is the initial estimated expansive pressure (σ_c , Fig. 6.4) in each lattice element based on the crystallization pressure theory (Eq. 6.4). After applying this input (Fig. 6.4), the simulated generated stress of the simulated specimen can be obtained. However, the simulated generated stress may be different from the experimentally obtained generated stress. In order to make the simulated and experimental generated stresses be equal to each other, one factor was put in the original equation (Eq. 6.4), as described in Eq. 6.5. The factor is defined as the final scaling factor (f), which considers features such as the size difference between the nanopores and the calculated volume. The final scaling factor (f) needs to be figured out in the simulations in this chapter.

$$\sigma_{suggested} = f\sigma_c \quad (6.5)$$

where σ_c represents the initial estimated expansive pressure which is based on the crystallization pressure theory, as described in Eq. 6.4. $\sigma_{suggested}$ stands for the suggested expansive pressure, which can lead to that the simulated external generated stress is equal to the experimentally obtained external generated stress. f means final scaling factor, which scales σ_c to be $\sigma_{suggested}$. This equation is for the calculation of local expansive pressure for future simulations. f (final scaling factor) needs to be figured out in the simulations in this chapter.

However, during the modeling process, it may be not one step to reach the experimentally obtained generated stress. In fact, during the modeling process, the lattice elements are removed step by step, which is realized by the function of a modeling parameter. The modeling parameter is defined as the scaling factor (m) in this chapter. Fig. 6.3 offers the inputs for the simulations. However, for each analysis step, the actual pressures applied on lattice elements are equal to the input multiply by the scaling factor (m) at that analysis step, as described in Eq. 6.6. The value of the scaling factor (m) at each analysis step is to make just one lattice element to be damaged and is calculated by the simulation system. Then, the simulated generated stress at each analysis step can also be obtained. When the simulated generated stress is equal to the experimentally obtained generated stress, the scaling factor (m) at that analysis step is equal to the final scaling factor (f).

$$\sigma_{actual} = m\sigma_c \quad (6.6)$$

where σ_c represents the initial estimated expansive pressure which is based on the crystallization pressure theory, as described in Eq. 6.4. σ_{actual} stands for the actual pressure applied on lattice elements at each analysis step, which is related to the scaling factor (m) at that analysis step. This equation is for the modeling process. At each analysis step, one scaling factor (m) is calculated by the simulation system to damage one lattice element.

6.3. NUMERICAL SIMULATION RESULTS AND DISCUSSION

6.3.1. RESTRAINED EXPANSION AND GENERATED STRESS

THE expansion and degradation of specimen immersed in 30 g/L SO_4^{2-} under high-restraint condition (7 mm) were studied numerically in this chapter. Firstly, the expansion behaviors after 21-day, 70-day, 105-day, 133-day and 189-day exposure were simulated individually in this section.

The simulation of 70-day exposure was a continued simulation of 21-day exposure, which means the simulation of 70-day exposure was carried out with the damaged structure caused by 21-day exposure if the damage occurred. The same procedure of continued simulations was applied on the simulations of 105-day, 133-day and 189-day exposure, which were based on the simulated damaged structures from 70-day, 105-day and 133-day exposure, respectively. In such a way, the continuous expansion and degradation in experiments were simulated.

For each exposure time, the measured restrained expansion and generated stress in experiments are summarized in Table 6.2, which is based on Fig. 2.7 and Fig. 2.8. Therefore, for each simulated case, the simulation was stopped when the simulated generated stress reached the measured generated stress at that exposure time, which is named as the final analysis step. Then, the scaling factor (m) at the final analysis step can be obtained, which is taken as the final scaling factor (f).

Table 6.2: The measured restrained expansion and generated stress of specimen immersed in 30 g/L SO_4^{2-} under high-restraint condition (7 mm)

Duration (days)	Restrained expansion (%)	Generated stress (MPa)
21	0.0080	2.5
70	0.0175	5.5
105	0.0214	6.8
133	0.0257	8.1
189	0.0317	10.1

The final scaling factor (f) and the simulated restrained expansion at the final analysis step are listed in Table 6.3. It can be found that the simulated expansion matches very well with the measured expansions for each exposure time, which indicates that the function of the 7 mm steel bar was implemented correctly in the simulations.

Table 6.3: The simulated expansion and scaling factor when the simulated generated stress reached the measured generated stress in experiments

Pressure gradient from Fig. 6.3	Generated stress (MPa)	Final scaling factor (f)	Expansion (%)
21d - 30 g/L	2.5	0.99	0.0080
70d - 30 g/L	5.5	1.74	0.0175
105d - 30 g/L	6.8	1.90	0.0217
133d - 30 g/L	8.1	1.80	0.0258
189d - 30 g/L	10.1	2.01	0.0322

This research focuses on the magnitude of local expansive pressure. The generated stresses at the two ends of the specimen were measured experimentally and part of the results are listed in Table 6.2. However, the distribution of local expansive pressure along diffusion direction always had a dynamic gradient at different exposure time, which led to the measured generated stress and expansion for the restrained specimens. Therefore, considering the non-uniform distribution, the local expansive pressure cannot be estimated directly based on the experimental measurements, which was discussed through simulations in this chapter.

As shown in Table 6.3, the final scaling factor (f) for each simulated case was obtained through simulations, which can make the simulated generated stresses and expansions equal to the experimental measurements at the corresponding exposure time. Based on Eq. 6.5, the magnitude of the local expansive pressure can be calculated (σ_c was taken from Fig. 6.3). The calculated local expansive pressure can lead to the experimental observations at the corresponding exposure time.

6.3.2. SUGGESTED EQUATION TO ESTIMATE EXPANSIVE PRESSURE

In this chapter, the initial estimation of local expansive pressure (Eq. 6.4) is based on the crystallization pressure theory, which happens inside the nanopores. Therefore, for the original crystallization pressure equation, the calculated pressure should be the pressure applied on the wall of nanopore. However, due to the experimental limit, the sulfur distributions were obtained at microscale with a resolution of $4.94 \mu\text{m}$ for each analysis spot, as described in Ma et al. [88]. Due to the computational limit, the calculated pressure at each analysis spot in this chapter covered a cubic volume with a length of 0.25 mm, which is much larger than the size of nanopores. In order to consider the influence mentioned above, the final scaling factor (f) is added in Eq. 6.4 as a simplistic consideration, which is described in Eq. 6.5. Therefore, with the purpose of attempting to find a simple way to estimate the local expansive pressure at a larger scale, Eq. 6.5 is proposed as a start.

The value of the final scaling factor (f) was obtained through simulations in section 6.3.1, which was shown in Table 6.3. For the ideal situation, it is expected that the final scaling factors (f) in different simulated cases can be the same value. As shown in Table 6.3, the final scaling factors (f) of the last four simulated cases are very close with each

other. The average value is 1.86. However, the final scaling factor (f) of the first simulated case (21-day exposure) is quite different from the other four.

If the final scaling factor (f) is suggested to be 1.86 for all the cases, the corresponding generated stress can be obtained through simulations, which is listed in Table 6.4. Compared with the measured generated stress in experiments, the differences between simulations and experiments were calculated, which were shown as $\Delta\sigma$ in Table 6.4. It is found that, for the simulated case of 21-day exposure, the simulated generated stress is quite different from the experimentally measured generated stress. This is maybe caused by the fact that the simulation mesh in this chapter is too big for the simulated case of 21-day exposure, considering that the sulfur content along the penetration direction changes fast with a small increase of the penetration depth at 21-day exposure. However, for all the other simulated cases, $\Delta\sigma$ is within $\pm 7\%$. Therefore, the final scaling factor (f) of 1.86 is acceptable for the future estimations. The final scaling factor (f) also includes the influence of creep and stress relaxation. This influence is probably also different at early ages and it might vary in time.

As a result, Eq. 6.5 is suggested to be used for the estimation of the local expansive pressure in the future simulations, which is valid for a certain scale of observation, i.e. 0.25 mm/cell. The final scaling factor (f) used for calculations is suggested to be 1.86. The sulfur content can be measured by experiments or predicted by transport-reaction models.

Table 6.4: The differences between simulated and experimental generated stress when the final scaling factor (f) is taken as 1.86

Pressure gradient from Fig. 6.3	Final scaling factor (f)	Simulated generated stress (MPa)	Measured generated stress (MPa)	$\Delta\sigma$ (%)
21d - 30 g/L	1.86	4.7	2.5	88
70d - 30 g/L	1.86	5.9	5.5	7
105d - 30 g/L	1.86	6.7	6.8	-1
133d - 30 g/L	1.86	8.4	8.1	4
189d - 30 g/L	1.86	9.4	10.1	-7

$$\Delta\sigma = (\text{Simulated stress} - \text{Measured stress}) / \text{Measured stress}$$

6.3.3. LARGEST GENERATED STRESS AND CRACK PATTERN

The continued simulations mentioned above were stopped at 189-day exposure. In order to study the cracking process of the specimen after 189-day immersion, one simulation was carried out with the damaged structure from the simulated case of 189-day exposure.

The local expansive pressure at 189-day (Fig. 6.3) was assumed to be the local expansive pressure in this simulation, which is the input for the simulation. The actual pressure applied on the lattice elements at each analysis step is related to the scaling factor (m) at that analysis step, as described in Eq. 6.6.

One analysis step means that one element is damaged. The simulated generated

stress of the simulated specimen at each analysis step and the corresponding scaling factor (m) are shown in Fig. 6.5. As can be found in Fig. 6.5b, with increasing analysis step, the scaling factor (m) kept on increasing until step 5 and then started to decrease. At each analysis step, one scaling factor was found by the simulation system to damage one lattice element. The actual pressure applied on lattice elements at each analysis step was equal to the input pressure multiplied by the scaling factor at that analysis step. Therefore, the increase of the scaling factor means the increase of expansive pressure applied on lattice elements, which is representing the increase of exposure time that also implies increase of expansive pressure. The difference is that the pressure gradient in experiments is changing. However, the pressure gradient in the simulation is taken from the experimental results at 189-day exposure and therefore keeps the same during simulation process. The decrease of scaling factor was caused by the crack localization.

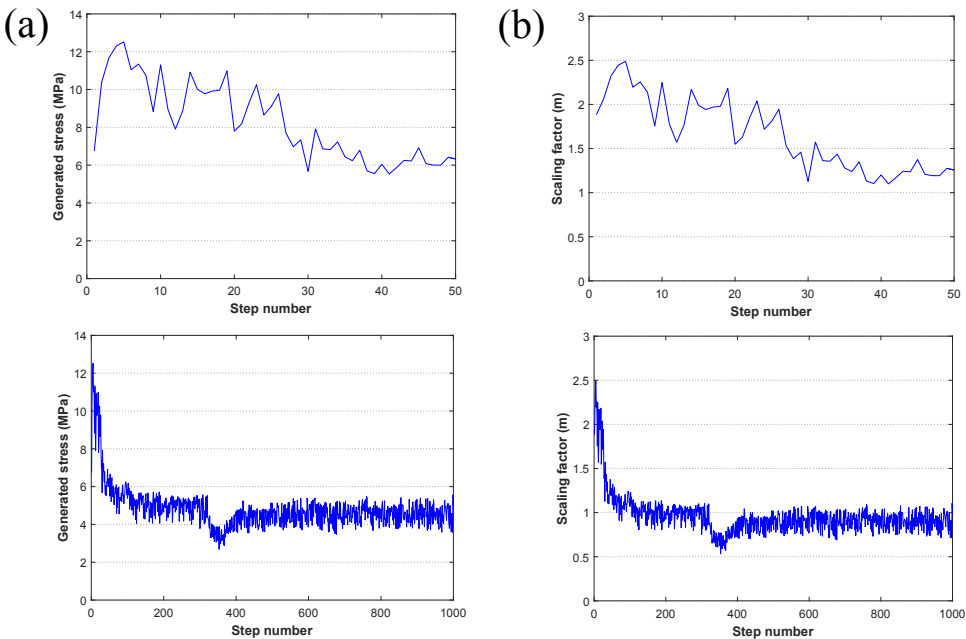


Figure 6.5: (a) Numerical results of generated stress of specimen immersed in 30 g/L SO_4^{2-} under high-restraint condition (7 mm) with the increase of analysis step and (b) the scaling factor (m) applied at the corresponding analysis step.

As shown in Fig. 6.5a, the generated stress at the two ends of the simulated specimen kept on increasing until analysis step 5 and then began to decrease. The largest generated stress was 12.5 MPa. For the specimen immersed in 30 g/L SO_4^{2-} under high-restraint condition (7 mm), the largest generated stress measured by experiment was 13.4 MPa which occurred at 565-day immersion (Fig. 2.8). It can be found that the two values of largest generated stress were very close. However, there were still two factors which may influence the simulated results. First, the gradient of local expansive pressure applied on this simulation was based on the sulfur distribution at 189-day exposure. The

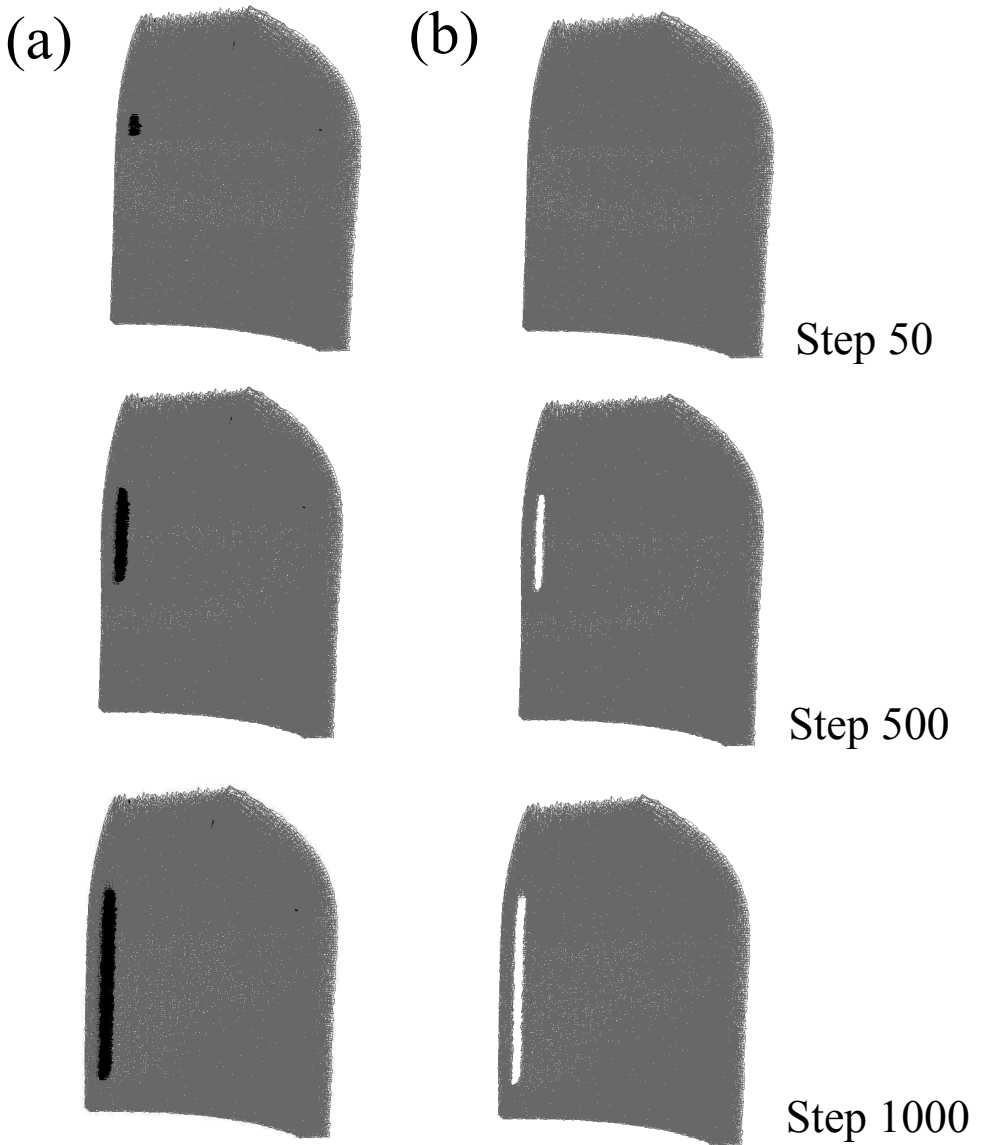


Figure 6.6: Numerical results of cracking process of specimen immersed in 30 g/L SO_4^{2-} under high-restraint condition (7 mm) with the increase of analysis step. (a) Crack pattern (black-damaged element) and (b) deformed lattice of undamaged elements.

increase of immersion time is assumed to be realized by the pressure gradient at 189-day exposure multiplied by the increasing scaling factor. However, in the experiment, the pressure gradient kept on being smaller with immersion time increasing. The pressure gradient influences the crack localization. A smaller pressure gradient is expected to result in a bigger value of the largest generated stress, which is probably due to that a bigger value of internal pressure is needed to lead to the crack localization for a smaller pressure gradient. Therefore, if several time point after 189-day exposure were chosen and the corresponding pressure gradient was used as the input, the simulated largest generated stress is expected to be larger than 12.5 MPa. Second, the specimens were restrained at the two ends by the steel bars and therefore were under compressive stress during sulfate exposure. Creep can happen during the immersion tests. The consideration of creep may lead to a lower external generated stress.

As observed in the experiment, for the specimen immersed in 30 g/L SO_4^{2-} under high-restraint condition (7 mm), the generated stress initially kept on increasing and then started to decrease. The decrease of generated stress means that the specimen could not bear more compressive stress at the two ends and localized cracks started to develop. Before crack localization, the distributed microcracks were formed. However, for the simulation in this section, the crack localization occurred very fast. As presented in Fig. 6.5a, the generated stress started to decrease at analysis step 5 and then the cracks began to localize. This phenomenon can be caused by the large mesh resolution, which is 0.25 mm/cell. Therefore, the distributed microcracks cannot be shown in this simulation. However, the crack pattern of the specimen at damaged stage can be discussed. The simulated process of crack propagation is shown in Fig. 6.6. It is found that one vertical crack was formed. As observed in the experiment, the specimen was also damaged with vertical cracks. Therefore, the numerical study showed the same trend of cracking of the specimen as in the experimental observations.

6.4. SUMMARY AND CONCLUSIONS

IN this chapter, a numerical study was carried out on the specimen immersed in strong sulfate solution (30 g/L) under high-restraint condition (7 mm). The expansion and degradation processes of the specimen were simulated, which were also investigated experimentally in chapter 2 and 3. A 3D lattice model with a mesh resolution of 0.25 mm/cell was constructed. The local mechanical properties of cement paste lattice elements were obtained in chapter 5. The magnitude of local expansive pressure was discussed in this chapter. The main results are summarized as below.

- The expansion behaviors after 21-day, 70-day, 105-day, 133-day and 189-day exposure were simulated. For each simulated case, the simulation was stopped when the simulated generated stress reached the experimental measurement. According to the simulated results, an equation with a simplistic consideration based on crystallization pressure theory and sulfur content is proposed, which attempts to find a simple way to estimate local expansive pressure caused by external sulfate attack. The sulfur distributions at different exposure time were obtained from experimental measurements.
- One simulation was carried out to study the cracking process of the specimen.

The largest generated stress of 12.5 MPa and the localization of one vertical crack were observed in the simulated results, which showed a good agreement with the experimental results.

The increase of generated stress was caused by the continuous penetration of external sulfate ions into the hardened cementitious material, which can react with cement hydration products and result in the development of crystallization pressure within the pore network of cement paste. Therefore, this chapter is trying to link the measured sulfur content to the resulting expansive pressure. The expansive pressure on the pore wall is an internal pressure inside the cement paste, which causes the material to expand. If the external restraint was not applied on the specimen, the internal pressure would lead to free expansion. If the external restraint was applied on the specimens, which is realized by the steel bars in the center of the specimens in this study, the specimens tended to expand and therefore were under compressive stress at the two ends during the immersion tests. Due to the compressive stress, creep can occur. Therefore, the measured restrained expansion was in fact the final consequence of external sulfate attack and creep. External sulfate attack led to the increase of expansion, however, creep resulted in the decrease of expansion. As a result, if creep is not considered in the simulations, the simulated restrained expansion and generated stress can be larger than the measured restrained expansion and generated stress, respectively. In the present study, creep is partly overcome by introducing the final scaling factor. However, it would be better to consider creep and stress relaxation for further studies.

PART 4: CONCLUSIONS AND DISCUSSION OF RESULTS

7

CONCLUSIONS AND DISCUSSION OF RESULTS

In this chapter, a brief summary of the work presented in this PhD thesis is given. Furthermore, general conclusions and findings of this research are presented and discussed. In the end, some recommendations for further work are given.

7.1. RETROSPECTION

CHEMICAL degradation of cementitious materials is a serious threat to the durability and performance of concrete structures. External sulfate attack is a progressive degradation process that may cause expansion, cracking, loss of binder cohesion and increased permeability in cementitious materials. External sulfate attack in a saturated situation is a complex issue in which ionic transport, expansive reactions and mechanical damage interact with each other. These phenomena may be accompanied by significant macroscopic expansion and severe mechanical damage. However, the theories concerning the exact origin of the expansive pressure are still under debate. In recent years, the crystallization pressure theory has become the most widely cited hypothesis, and ettringite formation from monosulfate is also generally considered as the major cause, but more evidences for this mechanism are still needed. Moreover, the magnitude of the expansive pressure at different scale is still missing, since direct measurement of the expansive pressure on the walls of nanopores is highly challenging. Also the expansion behavior of larger scale specimens is in lack of complete experimental data from the literature. Furthermore, the process of crack initiation and propagation is seldom discussed. The development of pressure gradient has been largely neglected in the current literature. In this thesis, an attempt is made to contribute to the body of knowledge related to the problems mentioned above. Laboratory experiments and numerical simulations are used during the study.

Chapter 2 presents an experimental study on the expansion behavior of cement paste pipes under three types of longitudinal restraints, which are immersed in sodium sulfate solutions with SO_4^{2-} ion concentrations of 1.5 g/L and 30 g/L. The free expansion, restrained expansion and generated stress are quantified. The pore size distributions are analyzed periodically. Chapter 3 shows an experimental study on the degradation of cement paste exposed to sodium sulfate solutions. The sulfur ingress profiles of samples immersed in two types of sulfate concentrations are analyzed periodically. The three-dimensional crack patterns of the specimens immersed in strong sulfate solution (30 g/L) under three types of restraints are studied. The cracking process and the different crack patterns due to restrained level are discussed.

Chapter 4 studies the complex process of crack initiation and propagation during material degradation at microscopic scale. The damage evolution of unrestrained specimens immersed in 30 g/L sodium sulfate solution is investigated experimentally. The localization process of the subparallel cracks near the exposed surface at the depth of about 250 μm is studied.

Chapter 5 focuses on the mechanical properties of cement paste pipes just after 90-day curing in saturated limewater. Two types of specimens subjected to uniaxial tensile loading are studied experimentally and numerically, which are unnotched and single notched specimens. The obtained local mechanical properties of cement paste lattice elements are used in chapter 6. Chapter 6 presents a numerical study on expansion and degradation processes of the specimen immersed in strong sulfate solution (30 g/L) under high-restraint condition. After comparing with the experimental results in chapter 2 and 3, the magnitude of local expansive pressure caused by external sulfate attack is discussed in chapter 6.

7.2. GENERAL CONCLUSIONS AND DISCUSSION

IN every chapter of the thesis, conclusions related to that part of the work are drawn. Here, general conclusions and a discussion of their consequences for both scientific research and understanding of material performance and also for the engineering practice are given.

- *The external sulfate induced expansion is mainly due to the crystallization pressure developing inside the nanopores within the cement paste.*

In chapter 2, it was found that the pores with diameters between 10 nm and 70 nm were continuously filled during the exposure to both of the sulfate concentrations, which offers the experimental evidences for supporting the crystallization pressure theory to explain the origin of expansive pressure. The filling of nanopores in strong sulfate solution (30 g/L) was much faster than that in weak sulfate solution (1.5 g/L), which explained the observation of a faster expansion in strong sulfate solution.

As revealed by the mechanism of expansion, external sulfate attack is a multiscale problem in engineering practice, which occurs inside the nanopores of cement paste. For a concrete structure, mortar is the expansive part. Considering mortar, the internal expansive pressure only exists in the cement paste. Therefore, the expansive pressure in cement paste is the key parameter.

- *Both weak and strong sulfate solutions can lead to a rather high expansive pressure in cement paste.*

The expansive pressure on the pore wall is an internal pressure inside the cement paste, which causes the material to expand. If the external restraint was not applied on the specimen, the internal pressure led to free expansion. If the external restraint was applied on the specimens, in this study this was realized by the steel bars inside the specimens, the specimens tended to expand and therefore were under external compressive stress at the two ends. The amount of compressive stress was defined as the amount of generated stress. In this case, the internal pressure led to the generated stress and the corresponding restrained expansion.

This study aims at using the measured generated stress to reflect the internal expansive pressure. It was found that a stronger sulfate solution could result in a larger generated stress, when the exposure time was equal. In addition, both weak and strong sulfate solutions can lead to a rather high generated stress after a certain immersion time. The tensile strength of the specimen just after 90-day lime-water curing was studied experimentally in chapter 5, which was found to be 5.7 MPa. Compared with the tensile strength of the specimen, the measured generated stresses were rather high.

As discussed in section 1.1.3, 1.5 g/L SO_4^{2-} stands for natural condition in the moderately aggressive environment. 30 g/L SO_4^{2-} represents accelerating condition, which can also exist in natural environment for some special cases. For the engineering practice, attention should be paid on the sulfate concentration in service environment. This study indicates that, even for moderately aggressive

environment ($1.5 \text{ g/L SO}_4^{2-}$), the internal expansive pressure can reach a value higher than the tensile strength of cement paste after a long period of immersion. For a stronger sulfate solution, the time being needed to reach the tensile strength is shorter. Therefore, both weak and strong sulfate solutions can lead to degradation problems in engineering practice. A higher sulfate concentration can result in a faster degradation.

- *The gradient of expansive pressure plays a key role on the cracking of the specimens.*

In chapter 4, the crack initiation and propagation of unrestrained specimens immersed in strong sulfate solution (30 g/L) was studied. It was found that the critically steep gradient of local expansive pressure led to the localized crack. Before the crack localization, the heterogeneities of material and internal pressure resulted in the distributed cracks.

Due to the penetration process of external sulfate ions, a dynamic gradient of local expansive pressure along diffusion direction existed. A stronger sulfate solution resulted in a faster penetration. As a result, when the exposure time was equal, a stronger sulfate solution led to a larger gradient of local expansive pressure. The localized cracks can be formed when the pressure gradient is large enough. Therefore, the main difference between the weak and strong sulfate solutions is the internal pressure gradient.

As mentioned in chapter 3, no visually noticeable cracks were observed for the specimens immersed in weak sulfate solution (1.5 g/L) up to 807-day immersion. However, all the unrestrained and restrained specimens immersed in strong sulfate solution (30 g/L) were damaged obviously before 628-day immersion. Therefore, a stronger sulfate solution can lead to a faster degradation, which is mainly due to the difference of pressure gradient.

The penetration of external sulfate ions can lead to firstly the increase of permeability and then the damage of material, which occurs from the surface inwards. Considering the large dimension of concrete structure and the slow penetration process of external sulfate ions, the severe mechanical damage of the whole structure may occur after a very long time. A higher sulfate concentration can result in an earlier damage. Therefore, for the evaluation or prediction of the safety of concrete structures exposed to sulfate environment, the sulfate concentration and the design of service life should be both considered. It may be possible that the mechanical degradation of the whole structure keeps small and can even be ignored during the design time of service life, when the sulfate concentration is rather low. Therefore, the influence on concrete cover should be a more important concern for both weak and strong sulfate solutions.

- *More attention needs to be paid on concrete cover when exposed to weak sulfate environment (1.5 g/L).*

In this study, the small wall thickness (2.5 mm) of the specimens ensured a faster exposure of the entire cross-section, which led to the almost uniform distribution of local expansive pressure from 189-day immersion in weak sulfate solution (1.5

g/L). More uniform distribution of local expansive pressure was expected with exposure time increasing. Therefore, starting from 189-day immersion when pressure gradient almost disappeared, the measured generated stress can reflect the internal expansive pressure at the corresponding exposure time.

At 807-day immersion, even though the external generated pressure (11.1 MPa) which is caused by the internal expansive pressure was much higher than the tensile strength (5.7 MPa) of material, no visually noticeable cracks were observed for both unrestrained and restrained specimens. This phenomenon was due to the fact that the pressure gradient was small. However, for a specimen with a much larger dimension, the external sulfate ions may only reach the surface part after a long period of immersion. In this case, a steep pressure gradient is possible to appear, which may result in the damage in the surface area. Subsequently the specimen might be damaged further layer by layer.

On the other hand, cement paste was used in this study. This is a fairly homogeneous material which also has a more or less homogeneous local expansive pressure. In this case, there is no gradient. However, for concrete structures, a nonuniform distribution of local expansive pressure exists even for the same penetration depth, considering that the internal expansive pressure in sand or aggregates is zero. As a result, the nonuniform distribution of pressure can lead to more damage.

For the surface of concrete structures in engineering practice, the internal expansive pressure only exists in cement paste and can be much higher than the tensile strength of cement paste. In this case, it possibly results in an increased permeability and mechanical damage, which occurs layer by layer from the surface inwards. Therefore, for the concrete structures immersed in moderately aggressive environment (1.5 g/L) or slightly aggressive environment, the degradation of concrete cover should be under great concern. Degradation of the cover can lead to an acceleration of other durability problems, such as chloride induced corrosion.

- *External restraint has a marked influence on external sulfate induced degradation.*

The crack patterns of the damaged specimens immersed in strong sulfate solution (30 g/L) were studied in chapter 3. For the unrestrained specimen, a combination of horizontal cracks which started some distance away from the exposed surface and vertical cracks which started from the exposed surface was observed. The vertical crack is along the longitudinal direction of the specimen. The horizontal crack is in the plane of the cross-section and along the tangential direction of the circle. For the specimen under low-restraint condition (3 mm - 30 g/L), one main vertical crack was found. For the specimen under high-restraint condition (7 mm - 30 g/L), several vertical cracks were observed. Therefore, the level of external restraint influences the damage type of the specimens. Furthermore, a higher restraint can lead to an earlier damage of the specimen.

For the engineering practice, concrete structures are always subjected to external loading and restraining during service time. Based on the findings in this study, the concrete structure under a higher external compressive stress or restraining is

possibly damage earlier on the surface, when exposed to the same sulfate environment.

- *Simulations provide a step forward in understanding external sulfate attack on cementitious materials.*

In chapter 6, after comparing simulated results with experimental measurements, an equation with a simplistic consideration based on crystallization pressure theory and measured sulfur content was proposed, which attempted to link the magnitude of local expansive pressure with sulfur content. The calculated local pressure is valid for a certain scale of observation, i.e. 0.25 mm/cell. This equation can be used in practice for estimating local expansive pressure if the sulfur content is known. The sulfur content can be measured by experiments or predicted by transport-reaction models.

In this study, both the experimental and numerical investigations were carried out on cement paste. For concrete structures exposed to sulfate environment, the same numerical method can be used for evaluating or predicting the resulting degradation, if the sulfur distribution inside the concrete is known. Attention should be paid on the fact that the local expansive pressure is only applied on cement paste for a concrete structure. Then the boundary conditions in practice can also be employed on the simulations. And the mechanical damage can be simulated. Afterwards, for the damaged structure which is from the mechanical simulation, the permeability can be evaluated by transport models.

- *The experimental setup employed in this study works perfectly for ESA related researches and other studies on internal pressure induced problems.*

The specimen with a small wall thickness ensured a faster exposure of the entire cross-section. The application of steel bars offered different restraining levels. The strain gauge measurement system performed perfectly for measuring restrained expansions and generated stresses, even though the restrained expansions were in a range of several microns.

A complete experimental dataset was obtained in this research regarding the process of specimen expansion and degradation when exposed to sulfate solutions, which offered all the necessary information for the numerical studies in this research and can also be used for other researches with different numerical methods.

7.3. RECOMMENDATIONS FOR FUTURE WORK

IN this research work, an attempt was made to contribute to the body of knowledge related to cement paste expansion and degradation due to external sulfate attack. Many issues were tackled, while others arose or were left untouched. In the future, the following could be done:

- For the restrained specimens exposed to sulfate solutions in this study, the specimens tended to expand while being restrained by the steel bars. Therefore, the

specimens were under compressive stress at the two ends during immersion tests. Due to the compressive stress, creep would occur. The internal expansive pressure led to the restrained expansion, however, the restrained expansion would decrease due to creep. The measured restrained expansion was the final consequence of external sulfate attack and creep. In this case, if creep is not considered in the simulations, the simulated restrained expansion can be larger than the measured restrained expansion. Also, the simulated generated stress can be higher than the measured generated stress. In the present study, this is partly overcome by introducing the final scaling factor. However, it would be better to consider creep and stress relaxation for further studies.

- Testing of the decrease of mechanical properties at mesoscale and microscale. The uniaxial tensile tests can be carried out on the cement paste pipes exposed to sulfate solutions at different immersion time. In addition, a combination of nanoindentation technique and SEM-EDS microanalysis can be used for linking the decrease of mechanical properties with sulfur content.
- Evaluation of the increase of material permeability. External sulfate attack can result in a total strength loss and an increased permeability of concrete. The increase of permeability can lead to an acceleration of other durability problems, such as chloride induced corrosion.
- Extending research into concrete specimens and structures. This study focused on the expansive pressure in the cement paste, which is the origin of expansion. For the engineering practice, the influence on concrete should be considered. Therefore, experimental and numerical studies on concrete can be carried out as the extending research.
- External sulfate attack in a saturated situation is a complex issue in which ionic transport, expansive reactions and mechanical damage interact with each other. This study focuses on the expansive reactions and mechanical damage. The extended study can be a coupled model considering the whole process. External sulfate ions penetrate into the hardened concrete, and result in internal expansive pressure. The development of expansive pressure leads to the mechanical damage, which increases the permeability of concrete. In this case, the transport model, the reaction model and the mechanical model need to be coupled with each other.

REFERENCES

REFERENCES

- [1] F. W. Locher, W. Richartz, S. Sprung, Erstarren von zement. teil i: Reaktion und gefügeentwicklung, *Zement Kalk Gips* 29 (10) (1976) 435–442.
- [2] J. Stark, K. Bollmann, Delayed ettringite formation in concrete, *NORDIC CONCRETE RESEARCH-PUBLICATIONS-* 23 (2000) 4–28.
- [3] J. Zelić, R. Krstulović, E. Tkalčec, P. Krolo, Durability of the hydrated limestone-silica fume portland cement mortars under sulphate attack, *Cement and concrete research* 29 (6) (1999) 819–826.
- [4] K. Scrivener, J. Skalny, Internal sulphate attack and delayed ettringite formation, *Rilem Proceedings PRO 35, Proc. of the International Rilem TC 186-ISA Workshop* (2002) 4–6.
- [5] T. C. Powers, Structure and physical properties of hardened portland cement paste, *Journal of the American Ceramic Society* 41 (1) (1958) 1–6.
- [6] J. P. Skalny, J. Marchand, I. Odler, *Sulfate attack on concrete*, Spon Press, London, 2002.
- [7] C. Ouyang, A. Nanni, W. F. Chang, Internal and external sources of sulfate ions in portland cement mortar: two types of chemical attack, *Cement and Concrete Research* 18 (5) (1988) 699–709.
- [8] W. Kunther, B. Lothenbach, K. L. Scrivener, On the relevance of volume increase for the length changes of mortar bars in sulfate solutions, *Cement and Concrete Research* 46 (2013) 23–29.
- [9] W. Kunther, Investigation of sulfate attack by experimental and thermodynamic means, PhD thesis, EPFL, 2012.
- [10] B. Lothenbach, B. Bary, P. Le Bescop, T. Schmidt, N. Leterrier, Sulfate ingress in portland cement, *Cement and Concrete Research* 40 (8) (2010) 1211–1225.
- [11] C. Yu, W. Sun, K. Scrivener, Mechanism of expansion of mortars immersed in sodium sulfate solutions, *Cement and concrete research* 43 (2013) 105–111.
- [12] A. Bonakdar, B. Mobasher, N. Chawla, Diffusivity and micro-hardness of blended cement materials exposed to external sulfate attack, *Cement and Concrete Composites* 34 (1) (2012) 76–85.

- [13] EN 206, Concrete - Specification, performance, production and conformity, European Standard.
- [14] ACI 201, Guide to Durable Concrete, American Concrete Institute, Farmington Hills, MI.
- [15] H. Huang, Thermodynamics of autogenous self-healing in cementitious materials, PhD thesis, Delft University of Technology, The Netherlands, 2014.
- [16] A. Chabreliè, Mechanisms of degradation of concrete by external sulfate ions under laboratory and field conditions, PhD thesis, Ecole Polytechnique Federale De Lausanne, Lausanne, Switzerland, 2010.
- [17] J. Skalny, J. Marchand, I. Odler, Sulfate attack on concrete, 1st ed. Spon Press, London, 2002.
- [18] E. Rozière, A. Loukili, R. El Hachem, F. Grondin, Durability of concrete exposed to leaching and external sulphate attacks, *Cement and Concrete Research* 39 (12) (2009) 1188–1198.
- [19] H. Binici, O. Aksoğan, Sulfate resistance of plain and blended cement, *Cement and Concrete Composites* 28 (1) (2006) 39–46.
- [20] T. Schmidt, B. Lothenbach, M. Romer, J. Neuenschwander, K. Scrivener, Physical and microstructural aspects of sulfate attack on ordinary and limestone blended portland cements, *Cement and Concrete Research* 39 (12) (2009) 1111–1121.
- [21] M. Santhanam, M. D. Cohen, J. Olek, Sulfate attack research - whither now?, *Cement and concrete research* 31 (6) (2001) 845–851.
- [22] A. Neville, The confused world of sulfate attack on concrete, *Cement and Concrete research* 34 (8) (2004) 1275–1296.
- [23] E. Irassar, V. Bonavetti, M. Gonzalez, Microstructural study of sulfate attack on ordinary and limestone portland cements at ambient temperature, *Cement and Concrete Research* 33 (1) (2003) 31–41.
- [24] EN 197-1, Cement - Part 1: Composition, specifications and conformity criteria for common cements, European Standard.
- [25] K. Van Breugel, Simulation of hydration and formation of structure in hardening cement-based materials, PhD thesis, Delft University of Technology, The Netherlands, 1991.
- [26] M. Halaweh, Effect of alkalis and sulfates on portland cement systems, PhD thesis, University of South Florida, United States, 2007.
- [27] M. Alexander, A. Bertron, N. De Belie, Performance of cement-based materials in aggressive aqueous environments, State-of-the-Art report, RILEM TC 211-PAE, 2013.

- [28] M. Collepardi, A state-of-the-art review on delayed ettringite attack on concrete, *Cement and Concrete Composites* 25 (4-5) (2003) 401–407.
- [29] S. Diamond, Delayed ettringite formation—processes and problems, *Cement and Concrete Composites* 18 (3) (1996) 205–215.
- [30] N. Crammond, The occurrence of thaumasite in modern construction—a review, *Cement and Concrete Composites* 24 (3-4) (2002) 393–402.
- [31] N. Crammond, The thaumasite form of sulfate attack in the uk, *Cement and Concrete Composites* 25 (8) (2003) 809–818.
- [32] J. R. Clifton, G. Frohnsdorff, C. Ferraris, Standards for evaluating the susceptibility of cement-based materials to external sulfate attack, *Materials Science of Concrete: Sulfate Attack Mechanisms*, J. Marchand and JP Skalny, eds., The American Ceramic Society (1999) 73–98.
- [33] M. Sahmaran, T. Erdem, I. Yaman, Sulfate resistance of plain and blended cements exposed to wetting–drying and heating–cooling environments, *Construction and Building Materials* 21 (8) (2007) 1771–1778.
- [34] J. A. Hartell, A. J. Boyd, C. C. Ferraro, Sulfate attack on concrete: effect of partial immersion, *Journal of Materials in Civil Engineering* 23 (5) (2010) 572–579.
- [35] P. Lens, A. Visser, A. Janssen, L. H. Pol, G. Lettinga, Biotechnological treatment of sulfate-rich wastewaters, *Critical Reviews in Environmental Science and Technology* 28 (1) (1998) 41–88.
- [36] A. Silva, M. Varesche, E. Foresti, M. Zaiat, Sulphate removal from industrial wastewater using a packed-bed anaerobic reactor, *Process Biochemistry* 37 (9) (2002) 927–935.
- [37] ASTM C1012, Standard Test Method for Length Change of Hydraulic-Cement Mortars Exposed to a Sulfate Solution, American Society of Testing and Materials: West Conshohocken, PA, USA.
- [38] W. Müllauer, R. E. Beddoe, D. Heinz, Sulfate attack expansion mechanisms, *Cement and concrete research* 52 (2013) 208–215.
- [39] M. Santhanam, M. D. Cohen, J. Olek, Effects of gypsum formation on the performance of cement mortars during external sulfate attack, *Cement and Concrete Research* 33 (3) (2003) 325–332.
- [40] M. Pauri, M. Collepardi, Thermo-hygrometrical stability of thaumasite and ettringite, *Il Cemento* 86 (1989) 177–184.
- [41] B. Tian, M. D. Cohen, Does gypsum formation during sulfate attack on concrete lead to expansion?, *Cement and concrete research* 30 (1) (2000) 117–123.
- [42] P. K. Mehta, Mechanism of sulfate attack on portland cement concrete—another look, *Cement and Concrete Research* 13 (3) (1983) 401–406.

- [43] P. K. Mehta, Mechanism of expansion associated with ettringite formation, *Cement and Concrete Research* 3 (1) (1973) 1–6.
- [44] PW Brown and HF Taylor, The role of ettringite in external sulfate attack, In *Materials Science of Concrete: Sulfate Attack Mechanism, Special Volume*. The American Ceramic Society, Westerville, OH, USA (1999) 73–98.
- [45] M. Whittaker, L. Black, Current knowledge of external sulfate attack, *Advances in Cement Research* 27 (9) (2015) 532–545.
- [46] M. Cohen, Modeling of expansive cements, *Cement and Concrete Research* 13 (4) (1983) 519–528.
- [47] M. Cohen, C. Richards, Effects of the particle sizes of expansive clinker on strength-expansion characteristics of type k expansive cements, *Cement and Concrete Research* 12 (6) (1982) 717–725.
- [48] I. Odler, M. Gasser, Mechanism of sulfate expansion in hydrated portland cement, *Journal of the American Ceramic Society* 71 (11) (1988) 1015–1020.
- [49] H. Schwiete, U. Ludwig, P. Jäger, et al., Investigations in the system $3 \text{ CaO} \cdot \text{Al}_2\text{O}_3 \cdot \text{CaSO}_4 \cdot \text{CaO} \cdot \text{H}_2\text{O}$, in: *Symposium on structure of portland cement paste and concrete*, Highway Research Board, Special Report, Vol. 90, 1964.
- [50] H. Lee, Expansive mineral growth and concrete deterioration: a microstructural and microanalytical study, PhD thesis, Iowa State University, Ames, Iowa, 1999.
- [51] P. Mehta, Scanning electron micrographic studies of ettringite formation, *Cement and Concrete Research* 6 (2) (1976) 169–182.
- [52] P. J. M. Monteiro, Ettringite formation on the aggregate-cement paste interface, *Cement and Concrete Research* 15 (2) (1985) 378–380.
- [53] G. W. Scherer, Crystallization in pores, *Cement and Concrete research* 29 (8) (1999) 1347–1358.
- [54] G. W. Scherer, Stress from crystallization of salt, *Cement and concrete research* 34 (9) (2004) 1613–1624.
- [55] R. J. Flatt, G. W. Scherer, Thermodynamics of crystallization stresses in DEF, *Cement and Concrete Research* 38 (3) (2008) 325–336.
- [56] M. Steiger, Crystal growth in porous materials-II: Influence of crystal size on the crystallization pressure, *Journal of crystal growth* 282 (3) (2005) 470–481.
- [57] R. J. Flatt, M. Steiger, G. W. Scherer, A commented translation of the paper by cw correns and w. steinborn on crystallization pressure, *Environmental geology* 52 (2) (2007) 187.
- [58] C. W. Correns, Growth and dissolution of crystals under linear pressure, *Discussions of the Faraday society* 5 (1949) 267–271.

- [59] J. W. Cahn, Surface stress and the chemical equilibrium of small crystals—i. the case of the isotropic surface, *Acta Metallurgica* 28 (10) (1980) 1333–1338.
- [60] A. W. Adamson, *Physical Chemistry of Surfaces*, 5th ed., Wiley, New York, 1990.
- [61] R. Khatri, V. Sirivivatnanon, J. Yang, Role of permeability in sulphate attack, *Cement and concrete research* 27 (8) (1997) 1179–1189.
- [62] T. C. Powers, T. L. Brownyard, Studies of the physical properties of hardened portland cement paste, in: *Journal Proceedings*, Vol. 43, 1946, pp. 101–132.
- [63] P. J. Monteiro, K. E. Kurtis, Time to failure for concrete exposed to severe sulfate attack, *Cement and Concrete Research* 33 (7) (2003) 987–993.
- [64] K. Ramyar, G. Inan, Sodium sulfate attack on plain and blended cements, *Building and environment* 42 (3) (2007) 1368–1372.
- [65] H. Cao, L. Bucea, A. Ray, S. Yozghatlian, The effect of cement composition and ph of environment on sulfate resistance of portland cements and blended cements, *Cement and Concrete Composites* 19 (2) (1997) 161–171.
- [66] B. Mather, Field and laboratory studies of the sulfate resistance of concrete, Tech. rep., ARMY ENGINEER WATERWAYS EXPERIMENT STATION VICKSBURG MS (1967).
- [67] N. Shanahan, A. Zayed, Cement composition and sulfate attack: Part i, *Cement and Concrete Research* 37 (4) (2007) 618–623.
- [68] A. M. Hossack, M. D. Thomas, Evaluation of the effect of tricalcium aluminate content on the severity of sulfate attack in portland cement and portland limestone cement mortars, *Cement and Concrete Composites* 56 (2015) 115–120.
- [69] ASTM C150, Standard Specification for Portland Cement, American Society of Testing and Materials: West Conshohocken, PA, USA.
- [70] H. F. Taylor, *Cement chemistry*, Thomas Telford, 1997.
- [71] M. Santhanam, M. D. Cohen, J. Olek, Mechanism of sulfate attack: A fresh look: Part 1: Summary of experimental results, *Cement and concrete research* 32 (6) (2002) 915–921.
- [72] S. S. Mirvalad, Improving performance of portland-limestone cements in sulfate exposures using supplementary cementing materials, Ph.D. thesis (2013).
- [73] M. D. Cohen, B. Mather, Sulfate attack on concrete: research needs, *Materials Journal* 88 (1) (1991) 62–69.
- [74] M. Santhanam, M. D. Cohen, J. Olek, Mechanism of sulfate attack: a fresh look: Part 2. proposed mechanisms, *Cement and concrete research* 33 (3) (2003) 341–346.

- [75] N. Buenfeld, J. Newman, The development and stability of surface layers on concrete exposed to sea-water, *Cement and Concrete Research* 16 (5) (1986) 721–732.
- [76] Rasheeduzzafar, O. S. B. Al-Amoudi, S. N. Abduljawad, M. Maslehuddin, Magnesium-sodium sulfate attack in plain and blended cements, *Journal of Materials in Civil Engineering* 6 (2) (1994) 201–222.
- [77] C. F. Ferraris, J. R. Clifton, P. E. Stutzman, E. J. Garboczi, Mechanisms of degradation of portland cement-based systems by sulfate attack, in: K.L. Scrivener, J.F. Young (Eds.), *Mechanisms of chemical degradation of cement-based systems* (1997) 185–192.
- [78] R. El-Hachem, E. Rozière, F. Grondin, A. Loukili, New procedure to investigate external sulphate attack on cementitious materials, *Cement and Concrete Composites* 34 (3) (2012) 357–364.
- [79] D. Planel, J. Sercombe, P. Le Bescop, F. Adenot, J.-M. Torrenti, Long-term performance of cement paste during combined calcium leaching–sulfate attack: kinetics and size effect, *Cement and Concrete Research* 36 (1) (2006) 137–143.
- [80] R. El-Hachem, E. Rozière, F. Grondin, A. Loukili, Multi-criteria analysis of the mechanism of degradation of portland cement based mortars exposed to external sulphate attack, *Cement and Concrete Research* 42 (10) (2012) 1327–1335.
- [81] E. Samson, J. Marchand, Modeling the transport of ions in unsaturated cement-based materials, *Computers & Structures* 85 (23-24) (2007) 1740–1756.
- [82] Y. Maltais, E. Samson, J. Marchand, Predicting the durability of portland cement systems in aggressive environments - laboratory validation, *Cement and Concrete Research* 34 (9) (2004) 1579–1589.
- [83] ASTM C452, Standard Test Method for Potential Expansion of Portland-Cement Mortars Exposed to Sulfate, American Society of Testing and Materials: West Conshohocken, PA, USA.
- [84] N. Patsikas, N. Katsiotis, P. Pipilikaki, D. Papageorgiou, E. Chaniotakis, M. Beazi-Katsioti, Durability of mortars of white cement against sulfate attack in elevated temperatures, *Construction and Building Materials* 36 (2012) 1082–1089.
- [85] C. F. Ferraris, P. E. Stutzman, K. A. Snyder, Sulfate resistance of concrete: a new approach, *PCA R&D Serial No. 2486* (2006) 1–78.
- [86] K. Van Tittelboom, N. De Belie, A critical review on test methods for evaluating the resistance of concrete against sulfate attack, *Concrete in aggressive aqueous environments, performance, testing and modeling* (2009) 298–306.
- [87] R. E. Beddoe, R. Lippok, Hygral stress in hardened cement paste, *Materials and Structures* 32 (9) (1999) 627–634.

- [88] X. Ma, O. Çopuroğlu, E. Schlangen, N. Han, F. Xing, Expansion and degradation of cement paste in sodium sulfate solutions, *Construction and Building Materials* 158 (2018) 410–422.
- [89] X. Ma, O. Çopuroğlu, E. Schlangen, N. Han, F. Xing, Experimental and numerical study on cement paste degradation under external sulfate attack, *Proceedings of 9th International Conference on Fracture Mechanics of Concrete and Concrete Structures* (2016).
- [90] S. Diamond, A critical comparison of mercury porosimetry and capillary condensation pore size distributions of portland cement pastes, *Cement and concrete research* 1 (5) (1971) 531–545.
- [91] R. A. Cook, K. C. Hover, Mercury porosimetry of hardened cement pastes, *Cement and Concrete research* 29 (6) (1999) 933–943.
- [92] G. Ye, Experimental study and numerical simulation of the development of the microstructure and permeability of cementitious materials, PhD thesis, Delft University of Technology, The Netherlands, 2003.
- [93] E. W. Washburn, in *proc. the national academy of sciences*, PNASA (1921) 7–21.
- [94] R. A. Cook, K. C. Hover, Experiments on the contact angle between mercury and hardened cement paste, *Cement and concrete research* 21 (6) (1991) 1165–1175.
- [95] Z. Yu, Microstructure development and transport properties of portland cement - fly ash binary systems - in view of service life predictions, PhD thesis, Delft University of Technology, The Netherlands, 2015.
- [96] O. Çopuroğlu, The characterisation, improvement and modelling aspects of frost salt scaling of cement-based materials with a high slag content, PhD thesis, Delft University of Technology, The Netherlands, 2006.
- [97] J. Pacheco, Corrosion of steel in cracked concrete: chloride microanalysis and service life predictions, PhD thesis, Delft University of Technology, The Netherlands, 2015.
- [98] N. B. Winter, Scanning electron microscopy of cement and concrete, WHD Microanalysis Consultants Ltd, 2012.
- [99] K. J. Krakowiak, W. Wilson, S. James, S. Musso, E.-J. Ulm, Inference of the phase-to-mechanical property link via coupled x-ray spectrometry and indentation analysis: Application to cement-based materials, *Cement and Concrete Research* 67 (2015) 271–285.
- [100] C. Yu, W. Sun, S. Karen, Application of image analysis based on sem and chemical mapping on pc mortars under sulfate attack, *Journal of Wuhan University of Technology* 29 (3) (2014) 534–539.

- [101] C. Famy, A. Brough, H. Taylor, The csh gel of portland cement mortars: Part i. the interpretation of energy-dispersive x-ray microanalyses from scanning electron microscopy, with some observations on csh, afm and aft phase compositions, *Cement and Concrete Research* 33 (9) (2003) 1389–1398.
- [102] M. A. B. Promentilla, T. Sugiyama, T. Hitomi, N. Takeda, Quantification of tortuosity in hardened cement pastes using synchrotron-based x-ray computed microtomography, *Cement and Concrete Research* 39 (6) (2009) 548–557.
- [103] S. Lu, E. Landis, D. Keane, X-ray microtomographic studies of pore structure and permeability in portland cement concrete, *Materials and Structures* 39 (6) (2006) 611–620.
- [104] E. J. Garboczi, J. W. Bullard, Shape analysis of a reference cement, *Cement and Concrete Research* 34 (10) (2004) 1933–1937.
- [105] E. Gallucci, K. Scrivener, A. Groso, M. Stampanoni, G. Margaritondo, 3d experimental investigation of the microstructure of cement pastes using synchrotron x-ray microtomography (μct), *Cement and Concrete Research* 37 (3) (2007) 360–368.
- [106] M. Beck, J. Goebbels, A. Burkert, B. Isecke, R. Bäßler, Monitoring of corrosion processes in chloride contaminated mortar by electrochemical measurements and x-ray tomography, *Materials and corrosion* 61 (6) (2010) 475–479.
- [107] B. Šavija, M. Luković, S. A. S. Hosseini, J. Pacheco, E. Schlangen, Corrosion induced cover cracking studied by x-ray computed tomography, nanoindentation, and energy dispersive x-ray spectrometry (eds), *Materials and Structures* 48 (7) (2015) 2043–2062.
- [108] D. R. Baker, L. Mancini, M. Polacci, M. Higgins, G. Gualda, R. Hill, M. Rivers, An introduction to the application of x-ray microtomography to the three-dimensional study of igneous rocks, *Lithos* 148 (2012) 262–276.
- [109] G. T. Herman, *Image reconstruction from projections: the fundamentals of computerized tomography*, New York: Academic Press, 1980.
- [110] E. N. Landis, D. T. Keane, X-ray microtomography, *Materials characterization* 61 (12) (2010) 1305–1316.
- [111] G. W. Scherer, Factors affecting crystallization pressure, in: *International RILEM TC 186-ISA Workshop on Internal Sulfate Attack and Delayed Ettringite Formation*, Villars, Switzerland, (2002) 139-154.
- [112] K. L. Scrivener, Backscattered electron imaging of cementitious microstructures: understanding and quantification, *Cement and Concrete Composites* 26 (8) (2004) 935–945.

- [113] M. B. Haha, E. Gallucci, A. Guidoum, K. L. Scrivener, Relation of expansion due to alkali silica reaction to the degree of reaction measured by sem image analysis, *Cement and Concrete Research* 37 (8) (2007) 1206–1214.
- [114] G. İ. Sezer, K. Ramyar, B. Karasu, A. B. Göktepe, A. Sezer, Image analysis of sulfate attack on hardened cement paste, *Materials & Design* 29 (1) (2008) 224–231.
- [115] P. Soroushian, M. Elzafraney, Morphological operations, planar mathematical formulations, and stereological interpretations for automated image analysis of concrete microstructure, *Cement and Concrete Composites* 27 (7) (2005) 823–833.
- [116] H. Wong, N. Buenfeld, M. Head, Estimating transport properties of mortars using image analysis on backscattered electron images, *Cement and Concrete Research* 36 (8) (2006) 1556–1566.
- [117] J. Van Mier, M. Van Vliet, Uniaxial tension test for the determination of fracture parameters of concrete: state of the art, *Engineering Fracture Mechanics* 69 (2) (2002) 235–247.
- [118] B. Hughes, G. Chapman, The complete stress-strain curve for concrete in direct tension, *RILEM Bulletin No. 30*. (1966) 95–97.
- [119] R. Evans, M. Marathe, Microcracking and stress-strain curves for concrete in tension, *Matériaux et Construction* 1 (1) (1968) 61–64.
- [120] E. Schlangen, J. Van Mier, Experimental and numerical analysis of micromechanisms of fracture of cement-based composites, *Cement and concrete composites* 14 (2) (1992) 105–118.
- [121] H. Toutanji, L. Liu, T. El-Korchi, The role of silica fume in the direct tensile strength of cement-based materials, *Materials and Structures* 32 (3) (1999) 203.
- [122] J. G. Van Mier, M. Nooru-Mohamed, Geometrical and structural aspects of concrete fracture, *Engineering Fracture Mechanics* 35 (4-5) (1990) 617–628.
- [123] E. Schlangen, Experimental and numerical analysis of fracture processes in concrete, PhD thesis, Delft University of Technology, Delft, The Netherlands, 1993.
- [124] E. Schlangen, E. Garboczi, Fracture simulations of concrete using lattice models: computational aspects, *Engineering fracture mechanics* 57 (2) (1997) 319–332.
- [125] E. Schlangen, Z. Qian, 3d modeling of fracture in cement-based materials, *Journal of Multiscale Modelling* 1 (02) (2009) 245–261.
- [126] Z. Qian, E. Schlangen, G. Ye, K. van Breugel, Modeling framework for fracture in multiscale cement-based material structures, *Materials* 10 (6) (2017) 587.
- [127] Z. Qian, Multiscale modeling of fracture processes in cementitious materials, PhD thesis, Delft University of Technology, Delft, The Netherlands, 2012.

- [128] E. Schlangen, E. Koenders, K. Van Breugel, Influence of internal dilation on the fracture behaviour of multi-phase materials, *Engineering Fracture Mechanics* 74 (1) (2007) 18–33.
- [129] O. Çopuroğlu, E. Schlangen, Modeling of frost salt scaling, *Cement and Concrete Research* 38 (1) (2008) 27–39.
- [130] B. Šavija, M. Luković, J. Pacheco, E. Schlangen, Cracking of the concrete cover due to reinforcement corrosion: a two-dimensional lattice model study, *Construction and Building Materials* 44 (2013) 626–638.
- [131] M. Luković, B. Šavija, E. Schlangen, G. Ye, K. van Breugel, A 3d lattice modelling study of drying shrinkage damage in concrete repair systems, *Materials* 9 (7) (2016) 575.
- [132] L. Liu, G. Ye, E. Schlangen, H. Chen, Z. Qian, W. Sun, K. Van Breugel, Modeling of the internal damage of saturated cement paste due to ice crystallization pressure during freezing, *Cement and Concrete Composites* 33 (5) (2011) 562–571.

SUMMARY

Chemical degradation of cementitious materials is a serious threat to the durability and performance of concrete structures. External sulfate attack is one of the situations that may cause gradual but severe damage. Sulfate ions present in seawater, rivers, groundwater and industrial effluent can penetrate into the hardened concrete, and react with cement hydration products to form ettringite as well as gypsum crystals, if stronger sulfate concentrations are available. Such formations result in a solid volume increase and cause local expansive pressure within the pore network. Although the solid volume increase may initially reduce the porosity of cement paste, it will cause cracking at a later stage as the generated expansive pressure exceeds the tensile strength of cement paste. This, in turn, leads eventually to a total strength loss and an increased permeability of concrete.

External sulfate attack in a saturated situation is a complex issue in which ionic transport, expansive reactions and mechanical damage interact with each other. These phenomena may be accompanied by significant macroscopic expansion and severe mechanical damage. However, the theories concerning the exact origin of the expansive pressure are still under debate. In recent years, the crystallization pressure theory has become the most widely cited hypothesis, and ettringite formation from monosulfate is also generally considered as the major cause, but more evidences for this mechanism are still needed. Moreover, the magnitude of the expansive pressure at different scale is still missing, since direct measurement of the expansive pressure on the walls of nanopores is highly challenging. Also the expansion behaviors of larger scale specimens are lack of complete experimental data from the literature. Furthermore, the process of crack initiation and propagation is seldom discussed. The development of pressure gradient has been largely neglected in the current literature.

In this thesis, an attempt is made to increase the body of knowledge related to cement paste expansion and degradation due to external sulfate attack. Laboratory experiments and numerical simulations were used during the study.

External sulfate attack under continuous immersion condition is a slow diffusion process. Even though high water/cement ratios and high sulfate ion concentrations have been adopted as acceleration methods, research shows that the attack depth remains shallow even after several months. Therefore, specimens with a small thickness along the diffusion direction could be preferred for experimental research in order to ensure a faster exposure of the entire cross-section. In this study, small cement paste pipes with a wall thickness of 2.5 mm were prepared and immersed in sodium sulfate solutions with SO_4^{2-} ion concentrations of 1.5 g/L and 30 g/L. Three types of longitudinal restraints were applied on the specimens before exposure, which were created by a spring, a thin or a thicker stainless steel bar that was centered in the hollow specimens in order to facilitate the non-, low- or high-restraint condition. Strain gauges were used for the measurements of restrained expansions and generated stresses, with the purposes of

increasing the measurement accuracy and obtaining continuous experimental results. The free expansion until 420-day immersion was measured periodically. The restrained expansion and corresponding generated stress until 810-day immersion were quantified continuously.

The pore size distribution, sulfur distribution and crack pattern were also periodically analyzed. According to the MIP measurements, the pores with diameters between 10 nm and 70 nm were continuously filled during the immersion tests, and strong sulfate solution lead to a faster filling, which supports the crystallization pressure theory. The sulfur distributions at 0-day, 21-day, 70-day, 105-day, 133-day and 189-day immersion in strong and weak sulfate solutions were acquired based on SEM-EDS microanalysis, which can reflect the gradient of the local expansive pressure distribution at the corresponding immersion days. The corresponding expansions under three types of restraint were also obtained. The specimen immersed in strong sulfate solution under high-restraint condition (7 mm - 30 g/L) was almost damaged after 565-day exposure with the largest generated stress of 13.4 MPa. Several vertical cracks were found after 581-day immersion based on the image analyses of CT scanning results. The specimen immersed in strong sulfate solution under low-restraint condition (3 mm - 30 g/L) was almost damaged after 628-day exposure with the largest generated stress of 11.2 MPa. One main vertical crack was found after 765-day immersion. The crack development of the unrestrained specimen immersed in strong sulfate solution (30 g/L) was also studied by CT scanning at 189-day, 294-day, 343-day, 420-day and 469-day exposure. A combination of the horizontal cracks which started some distance away from the exposed surface and the vertical cracks which started from the exposed surface was observed. However, no visually noticeable cracks were observed for the specimens immersed in weak sulfate solution (1.5 g/L) up to 807-day immersion. The generated stresses of specimens under low-restraint condition (3 mm - 1.5 g/L) and high-restraint condition (7 mm - 1.5 g/L) after 807-day immersion were 8.8 MPa and 11.1 MPa, respectively.

The complex process of crack initiation and propagation during material degradation at microscopic scale was studied by SEM - EDS microanalysis. The damage evolution of unrestrained specimens immersed in strong sulfate solution (30 g/L) was investigated experimentally. The specimens before sulfate exposure and after 70-day, 105-day and 133-day immersion were studied. Image analysis was applied. The localization process of the subparallel cracks near the exposed surface at the depth of about 250 μm was studied. Progressive precipitation of gypsum crystals inside the localized cracks was observed. The change of sulfur gradient versus exposure time was analyzed. Based on that, the change of expansive pressure gradient versus exposure time was discussed.

Numerical models can be of use in understanding complex problems. Delft lattice model was used in this thesis. In order to obtain the realistic mechanical properties of lattice elements, the experimental and numerical studies on the mechanical properties of cement paste pipes just after 90-day curing was done prior to further simulations. Two types of specimens are subjected to uniaxial tensile loading, which are unnotched and single notched specimens. Two main results were obtained through experiments. The first one is the Young's modulus and tensile strength of unnotched specimens. The second one is the complete stress-strain curves of single notched specimens. A 3D lattice model with a mesh resolution of 0.25 mm/cell was constructed to simulate the two

types of specimens subjected to uniaxial tensile loading. After fitting with the experimental results, the local mechanical properties of cement paste lattice elements were obtained. Afterwards, a numerical study on expansion and degradation processes of the specimen immersed in strong sulfate solution under high-restraint condition (7 mm - 30 g/L) was performed. After comparing with the experimental results in previous chapters, the magnitude of local expansive pressure caused by external sulfate attack was discussed.

The experimental setup and techniques (such as strain gauge measurement system, SEM-EDS analysis and X-ray computed tomography) employed in this thesis can be used in the same or similar way for further studies on external sulfate attack or some other degradation problems. Also, the experimental results presented in this research can be used for further numerical studies.

SAMENVATTING

Chemische aantasting van cementgebonden materialen kan een serieuze bedreiging vormen voor de levensduur en prestatie van betonconstructies. Externe sulfaataantasting bijvoorbeeld kan een geleidelijke maar ernstige schade veroorzaken. Sulfaat-ionen, afkomstig uit zeewater, rivieren, grondwater en industrieel afvalwater dringen het verharde beton in en reageren met de cementhydratatieproducten, waarbij ettringiet wordt gevormd en bij hogere concentraties sulfaat-ionen gipskristallen. Dergelijke omzettingen zorgen voor een toename van het volume vaste stof en kunnen lokale expansieve druk in het porie-netwerk veroorzaken. Hoewel de toename van volume in eerste instantie de porositeit van cementpasta vermindert, veroorzaakt het in een later stadium scheurvorming als de gegenereerde expansieve druk groter wordt dan de treksterkte van cementpasta. Dit leidt op zijn beurt uiteindelijk tot sterkteverlies en een verhoogde permeabiliteit van het beton.

Externe sulfaataanval in verzadigde toestand is een complex probleem waarbij ionen transport, expansieve reacties en interne degradatie een rol spelen. Op macroscopische schaal kan dit gepaard gaan met een aanzienlijke uitzetting en ernstige mechanische schade. Niettemin staan de theorieën over de exacte oorsprong van de expansieve druk nog steeds ter discussie. De huidige, meest geciteerde, hypothese is de kristallisatiedruktheorie, waarbij de ettringietvorming uit monosulfaat als belangrijkste oorzaak wordt beschouwd, maar verdere onderbouwing hiervoor is gewenst. Daarnaast ontbreekt het aan informatie over de uitwerking van de expansieve druk op de verschillende niveau's (meso – micro) in het beton, aangezien directe meting van deze druk op de wanden van nanoporiën zeer uitdagend is. In experimentele gegevens in de literatuur ontbreekt het uitzettingsgedrag van grotere proefstukken. Verder wordt in de huidige literatuur de ontwikkeling van de drukgradiënt grotendeels verwaarloosd én wordt het proces van scheurinitiatie en -propagatie zelden besproken.

In dit proefschrift is getracht de kennis te vergroten van het gedrag van cementpasta met betrekking tot expansie en degradatie onder invloed van een externe sulfaataanval. Hiervoor is gebruik gemaakt van zowel laboratoriumexperimenten als numerieke simulaties.

Externe sulfaataanval in verzadigde toestand (onder water) is een langzaam verloopend diffusieproces. Hoewel hoge water/cement factoren en hoge sulfaationenconcentraties worden gebruikt om het proces te versnellen, toont onderzoek aan dat de indringdiepte desondanks beperkt blijft, zelfs na maanden van expositie. Vandaar dat voor experimenteel onderzoek proefstukken met een kleine dikte in de diffusierichting de voorkeur hebben, zodat een snellere indringing in de volledige doorsnede wordt bereikt. In deze studie zijn daarom kleine holle cilinders van cementpasta gemaakt met een wanddikte van 2,5 mm. Deze zijn ondergedompeld in natriumsulfaat-oplossingen met sulfaat (SO_4^{2-}) concentraties van 1,5 g/L en 30 g/L. De vervorming van de proefstukken is op 3 manieren in lengterichting verhinderd. De verhindering is gecreëerd met behulp

van een veer, een dunne of een dikkere roestvrijstalen staaf die gecentreerd in de holle proefstukken is opgenomen om respectievelijk geen, matige en sterke verandering van de vervormingen te creëren. Met het oog op het vergroten van de meetnauwkeurigheid en het verkrijgen van continue experimentele resultaten, zijn rekstrookjes gebruikt voor de metingen van spanningen ten gevolge van de opgelegde vervormingen. De niet verhinderde uitzetting is periodiek gemeten tot 420 dagen expositie. De vervormingen van de verhinderde proefstukken en de corresponderende spanningen zijn continu vastgelegd tijdens de expositie van 810 dagen.

De poriegrootte verdeling, de zwavelionen-concentratie over de doorsnede en het scheurpatroon zijn periodiek geanalyseerd. Op basis van de MIP-metingen is vastgesteld dat de poriën met diameters tussen 10 nm en 70 nm voortschrijdend gevuld werden tijdens de onderdompelingstests. Een hogere concentratie sulfaat oplossing leidt tot een snellere vulling. Dit ondersteunt de kristallisatiedruktheorie. De zwavelionen-concentratie over de doorsnede bij 0, 21, 70, 105, 133 en 189 dagen expositie in sterke en zwakke sulfaatoplossingen is verkregen op basis van SEM-EDS-microanalyse, wat de verdeling van de lokale expansieve druk weergeeft op de overeenkomstige expositiedagen. Daarbij zijn de bijbehorende uitzettingen in combinatie met de wijze van verandering verkregen. Het sterk verhinderde proefstuk dat ondergedompeld was in de sterke sulfaatoplossing (7 mm - 30 g/L) was zwaar beschadigd na 565 dagen expositie, met een grootste gegenereerde spanning van 13,4 MPa. Na 581 dagen expositie zijn verscheidene verticale scheuren gevonden op basis van de beeldanalyses van CT-scanresultaten. Het matig verhinderde proefstuk dat ondergedompeld was in de sterke sulfaatoplossing (3 mm - 30 g/L) was zwaar beschadigd na 628 dagen expositie, met de grootste gegenereerde spanning van 11,2 MPa. Na 765 dagen expositie is één verticale scheur gevonden. Het scheurpatroon van het niet verhinderde proefstuk, dat ondergedompeld was in de sterke sulfaatoplossing (30 g/L) is bestudeerd op basis van CT-scans bij 189, 294, 343, 420 en 469 dagen expositie. Hierbij is een combinatie waargenomen van horizontale scheuren, die op enige afstand van het geëxposeerde oppervlak starten, én van verticale scheuren, die vanaf het geëxposeerde oppervlak starten. Bij de proefstukken die ondergedompeld waren in de zwakke sulfaatoplossing (1,5 g/L), zijn geen visueel waarneembare scheuren waargenomen tot 807 dagen expositie. De gegenereerde spanningen van de matig verhinderde (3 mm - 1,5 g/L) en sterk verhinderde (7 mm - 1,5 g/L) proefstukken na 807 dagen expositie waren respectievelijk 8,8 MPa en 11,1 MPa.

Het complexe proces van scheurinitiatie en -propagatie tijdens de materiaaldegradatie is op microscopische schaal bestudeerd door middel van SEM - EDS microanalyse. De ontwikkeling van de degradatie van de niet verhinderde proefstukken ondergedompeld in de sterke sulfaatoplossing (30 g/L) is experimenteel onderzocht. De proefstukken zijn vóór expositie en na 70, 105 en 133 dagen expositie bestudeerd. Hierbij is gebruik gemaakt van beeldanalysetechnieken. Het lokalisatieproces van de sub-parallelle scheuren nabij het geëxposeerde oppervlak op een diepte van ongeveer 250 μm is onderzocht. Binnen de gelokaliseerde scheuren is progressieve precipitatie van gipskristallen waargenomen. Het verloop van de gradiënt van zwavelionen-concentratie in het geëxposeerde proefstuk is in de tijd geanalyseerd. Hierop gebaseerd, is de verandering van de expansieve drukgradiënt versus de expositietijd besproken.

Numerieke modellen kunnen van nut zijn bij het begrijpen van complexe proble-

men. In dit proefschrift is het Delftse Lattice model gebruikt. Om realistische mechanische eigenschappen te verkrijgen als input voor de staafelementen zijn, voorafgaand aan verdere simulaties, experimentele en numerieke studies uitgevoerd naar de mechanische eigenschappen van 90 daagse cementpasta cilinders. Twee typen proefstukken zijn onderworpen aan een uni-axiale trekbelasting: een ingezaagd (1 notch) en een niet-ingezaagd proefstuk. Op basis van de experimenten zijn twee belangrijke resultaten verkregen. Als eerste de meting van de E-modulus en treksterkte van de niet-ingezaagde proefstukken en als tweede de vastlegging van complete spanning-rek-diagrammen van de ingezaagde proefstukken. Om de experimenten van de twee typen proefstukken, onderworpen aan een één-assige trekbelasting, te simuleren, is gebruik gemaakt van een 3D-Lattice model met een elementresolutie van 0,25 mm/cel. Op basis van het fitten van de experimentele resultaten, zijn de lokale mechanische eigenschappen van cementpasta staafelementen verkregen. Daarna is een numerieke studie uitgevoerd met betrekking tot de expansie- en degradatieprocessen in het sterk verhinderde proefstuk, dat was ondergedompeld in de sterke sulfaatoplossing (7 mm - 30 g/L). Na vergelijking met de experimentele resultaten in eerdere hoofdstukken, is de grootte van lokale expansieve druk ten gevolge van de externe sulfaataanval besproken.

De experimentele opstelling en technieken (zoals het systeem om spanningen te meten op basis van rekstrookjes, SEM-EDS-analyse en röntgen-computertomografie) die in dit proefschrift zijn gebruikt, kunnen op dezelfde of vergelijkbare wijze worden toegepast in verdere studies met betrekking tot externe sulfaataantasting of andere degradatieproblemen. Daarnaast kunnen de experimentele resultaten die in dit onderzoek zijn gepresenteerd, gebruikt worden voor verdere numerieke studies.

CURRICULUM VITÆ

Xu MA

21-11-1987 Born in Shaanxi Province, China.

EDUCATION

2006-2010 BSc Student in Civil Engineering
Faculty of Civil Engineering
Hunan University, China

2010-2013 MSc Student in Geotechnical Engineering
Faculty of Civil Engineering
Guangzhou University, China

2012-2012 Exchange Program
Department of Civil Engineering
Tampere University of Technology, Finland

2013-2018 PhD Candidate
Faculty of Civil Engineering and Geosciences
Delft University of Technology, The Netherlands
Thesis: Cement paste degradation under external sulfate attack
 - An experimental and numerical research
Promotor: Prof. dr. ir. E. Schlangen
Copromotor: Dr. O. Çopuroğlu

e-mail maxuTUD@163.com

LIST OF PUBLICATIONS

JOURNAL PUBLICATIONS

1. **X. Ma**, O. Çopuroğlu, E. Schlangen, N. Han and F. Xing. *Expansion and degradation of cement paste in sodium sulfate solutions*. Construction and Building Materials. 158 (2018) 410–422.
2. **X. Ma**, O. Çopuroğlu, E. Schlangen, N. Han and F. Xing. *Microstructural characterization on cement paste degradation caused by external sulfate attack*. Submitted for Publication.
3. **X. Ma**, E. Schlangen, O. Çopuroğlu, N. Han and F. Xing. *Experimental and numerical study on mechanical properties of cement paste pipes subjected to uniaxial tensile loading*. Submitted for Publication.
4. **X. Ma**, O. Çopuroğlu, E. Schlangen, N. Han and F. Xing. *Microstructural evolution of cement paste exposed to strong sodium sulfate solution*. Submitted for Publication.

CONFERENCE PROCEEDINGS

1. **X. Ma**, O. Çopuroğlu, E. Schlangen, N. Han and F. Xing. *Cement paste expansion under external sulfate attack*. Proceedings of 14th International Conference on Durability of Building Materials and Components, Ghent, Belgium, 2017.
2. **X. Ma**, O. Çopuroğlu, E. Schlangen, N. Han and F. Xing. *Experimental and numerical study on cement paste degradation under external sulfate attack*. Proceedings of 9th International Conference on Fracture Mechanics of Concrete and Concrete Structures, Berkeley, USA, 2016.

ACKNOWLEDGEMENTS

Life is a series of journeys. Looking back to my PhD journey during the five years stay in the Netherlands, some memories already become blurred. However, the moments I shared with you are always clear and unforgettable. At the end of this thesis, I would like to take this opportunity to express so many appreciations to those who have helped and supported me.

First of all, I would like to express my deepest appreciation to my promotor Prof. Erik Schlangen. I will forever be grateful for his help, encouragement, patient guidance and persistent support, which motivated me to find the way during this PhD journey and walk out of all the struggles with passion. I truly appreciate that he was always available and supportive for discussions at every moment when I needed help, even though his schedule was extremely busy. His suggestions always helped me find the right direction. Without all of these, I could not accomplish this PhD work. My special appreciation extends to my copromotor Dr. Oğuzhan Çopuroğlu for his suggestions, help, patient guidance and continuous support throughout my research. New ideas could always come out of my mind during discussions with him which made my work more efficient.

I would also like to acknowledge Guangdong Province Key Laboratory of Durability for Marine Civil Engineering at Shenzhen University, Guangzhou Elite Project of Guangzhou Municipal Government and Delft University of Technology, for sponsoring the research work reported in this thesis. In particular, I would like to thank Prof. Feng Xing, Prof. Ningxu Han and Prof. Dawang Li at Shenzhen University, who provided me this valuable opportunity and recommended me to be a PhD candidate in Delft University of Technology.

Meanwhile, I would like to give many thanks to my doctoral committee members, Prof. Ignacio Carol, Prof. Klaas van Breugel, Prof. Dick Hordijk and Dr. Guang Ye, for taking the time and effort to carefully review my work and attend my PhD defense. I particularly would like to acknowledge Dr. Guang Ye for all his help.

A special gratitude goes to Zhiwei Qian, Branko Šavija and Mladena Luković, thanks a lot for their continuous help both at and outside of work these years. I really appreciate that a lot! Some of the most important people during a PhD research are the office mates. I feel lucky to share the office with Branko for more than three years, who influenced me a lot! Thanks also goes to my current office mate, Yidong Gan. We shared a lot with each other about research and life. Thanks for the friendship!

The starting period of a journey is always difficult. Appreciations go to Zhuqing Yu, Haoliang Huang, Hua Dong and Tianshi Lu, especially for their help at the start of my PhD journey. To Jiayi Chen (Wenqin Shi), Xuliang Hou (Ying Yang), Zichao Pan and Hongzhi Zhang, thanks for the help and friendship. The special gratitude also goes to Prof. Jiangxiong Wei, Prof. Yingzi Yang, Dr. Yun Huang and Dr. Fuhai Li, who helped me a lot during their visiting in Microlab. Moreover, I would like to give many thanks to Jeannette van den Bos, who helped me translate my summary in this thesis from English

to Dutch and also shared with me a lot of interesting things about the Netherlands during daily coffee break. Thanks also goes to Yu Chen, for his help with the design of this thesis cover and the friendship.

Many thanks goes to those that make our lab work possible: Arjan Thijssen for his teaching in ESEM and MIP and help in CT scan, Gerrit Nagtegaal for his big help in my experimental work, Maiko van Leeuwen, John van den Berg and Ton Blom for their kind help and making the lab atmosphere so enjoyable. I would also like to give my thanks to Paul Vermeulen, who helped me a lot in building my experimental setup. Furthermore, our secretary Claire de Bruin and former secretary Nynke Verhulst are also highly appreciated for their kind help with various daily issues.

Special thanks also goes to Stefan Chaves Figueiredo and Bianca Fraga Silva, Claudia Romero Rodríguez and Fernando França de Mendonça Filho, Marija Nedeljković and Patrick Holthuizen, Maria Varini, and Martin Megalla, thanks for the friendship, the lunch time, coffee break and all the great times that we have shared. Many thanks also goes to Aleksandar Milenković for his support.

I would also like to thank all the other colleagues and former colleagues of Microlab. It would not be such a wonderful experience without any of them. Prof. Rob Polder, Prof. Eddie Koenders, Dr. Henk Jonkers, Renee Mors, Amir Tabakovic, Ennery Leon, Lourdes Maria Silva de Souza, Rene Veerman, José Pacheco, Caner Anaç, Hitham M. Ashry, Senot Sangadji, Eirini Tziviloglou, Balqis MD Yunus, Farhad Pargar, Bahman Ghiassi, Virginia Wiktor, Natalie Carr, Damian Palin, Agus Susanto, Lupita Sierra Beltran, Amir Zomorodian, Yask Kulshreshtha, Kuba Pawlowicz, Josef Kveton, Albina Kostiuhenko and Bart Hendrix, thanks all for the joyful moments, constructive discussions and shared experiences! A very special gratitude goes to my Chinese colleagues for all the great times that we have shared, to Yuwei Ma, Xiaowei Ouyang, Yibing Zuo, Wenjuan Lyu and Zhenming Li for their help, and to Leyang Lu (Xueer Tang), Peng Gao, Jiahua Liu, Bei Wu, Hao Huang (Niha), Zhipei Chen, Shi Xu (Qiling Wang), Shizhe Zhang, Yong Zhang, Yading Xu and Boyu Chen for their friendship and support!

I am also very grateful to all the friends that I met in the Netherlands. Special thanks firstly goes to Minghe Shan (Lingling Shi) and Zheng Liu (Cui Ping). Travelling with them can always bring me surprise and happiness. Great moments as the flatmate and the deep friendship with them will last forever in my mind. Many thanks also goes to all the GEPers (supported by Guangzhou Elite Project Scholarship) at TUDelft, particularly to Zhongbo Zhou for his great help for my settle down in Delft, and Bawei Huang for his friendship and all the unforgettable memories (such as cycling to Katwijk, Afsluitdijk, Brielle, etc.). I would also like to express my appreciation to Chenjie Yu, Hengqian Yi, Tao Lv, Jiawei Lai, Xiaoxiang Liu, Kai Li, Bo Hu, Long Wu, Xuedong Zhang, Ran Shang, Gang Liu, Peng Wei, Zhen Yang, Haixing Fang, Peiyao Luo, Mingjuan Zhao et al. My life in the Netherlands could not be so colorful without them.

At the end, I would like to express the love from the bottom of my heart to my parents for their unconditional love, endless support, great patience and continuous encouragement at every step of my life which make what I am today, to my girlfriend Yu XIE for her love, understanding and continuous support. Love you all for all my life!

*Xu MA
Delft, October 2018*

